

Resonant or asymmetric: The status of sub-GeV dark matter

Sowmiya Balan,^a Csaba Balázs,^b Torsten Bringmann,^c
Christopher Cappiello,^{d,e,f} Riccardo Catena,^g Timon Emken,^h
Tomás E. Gonzalo,^a Taylor R. Gray,^g Will Handley,^{i,j} Quan Huynh,^b
Felix Kahlhoefer^a and Aaron C. Vincent^{d,e,f}

^aInstitute for Theoretical Particle Physics (TTP), Karlsruhe Institute of Technology (KIT), 76128 Karlsruhe, Germany

^bSchool of Physics and Astronomy, Monash University, Melbourne VIC 3800, Australia

^cDepartment of Physics, University of Oslo, N-0316 Oslo, Norway

^dArthur B. McDonald Canadian Astroparticle Physics Research Institute, Kingston ON K7L 3N6, Canada

^eDepartment of Physics, Engineering Physics and Astronomy, Queen's University, Kingston ON K7L 3N6, Canada

^fPerimeter Institute for Theoretical Physics, Waterloo ON N2L 2Y5, Canada

^gChalmers University of Technology, Department of Physics, SE-412 96 Göteborg, Sweden

^hThe Oskar Klein Centre, Department of Physics, Stockholm University, AlbaNova, SE-10691 Stockholm, Sweden

ⁱKavli Institute for Cosmology, University of Cambridge, Madingley Road, Cambridge, CB3 0HA, UK

^jCavendish Laboratory, University of Cambridge, JJ Thomson Avenue, Cambridge, CB3 0HE, UK
E-mail: sowmiya.balan@kit.edu, taylor.gray@chalmers.se, kahlhoefer@kit.edu

Abstract. Sub-GeV dark matter (DM) particles produced via thermal freeze-out evade many of the strong constraints on heavier DM candidates but at the same time face a multitude of new constraints from laboratory experiments, astrophysical observations and cosmological data. In this work we combine all of these constraints in order to perform frequentist and Bayesian global analyses of fermionic and scalar sub-GeV DM coupled to a dark photon with kinetic mixing. For fermionic DM, we find viable parameter regions close to the dark photon resonance, which expand significantly when including a particle-antiparticle asymmetry. For scalar DM, the velocity-dependent annihilation cross section evades the strongest constraints even in the symmetric case. Using Bayesian model comparison, we show that both asymmetric fermionic DM and symmetric scalar DM are preferred over symmetric fermionic DM due to the reduced fine-tuning penalty. Finally, we explore the discovery prospects of near-future experiments both in the full parameter space and for specific benchmark points. We find that the most commonly used benchmark scenarios are already in tension with existing constraints and propose a new benchmark point that can be targeted with future searches.

Keywords: dark matter theory, dark matter experiments, cosmology of theories beyond the SM, particle physics - cosmology connection

Preprint numbers: TTP24-015, P3H-24-033

Contents

1	Introduction	1
2	Models of sub-GeV dark matter	4
2.1	Decays, annihilations and self-interactions	6
2.2	Parameter ranges and priors	8
3	Constraints and likelihoods	9
3.1	Cosmological constraints	10
3.2	Astrophysical constraints	13
3.3	Accelerator experiments	15
3.4	Direct detection	18
4	Results	20
4.1	Fermionic dark matter	20
4.2	Scalar dark matter	29
5	Discussion	32
5.1	Sensitivity projections	32
5.2	A new benchmark scenario	34
6	Conclusions	35
A	Relic density calculations	37
A.1	Asymmetric dark matter with DARKSUSY	38
A.2	Limitations of the standard Boltzmann approach	38
B	Bullet Cluster constraints	41
C	Relativistic cross sections for beam dump DM searches	42
D	Observable predictions from Bayesian scans	43
E	GAMBIT implementation	44
E.1	New models	44
E.2	Updates to DarkBit, CosmoBit and ColliderBit	47
E.3	Backend interfaces	48

1 Introduction

The most plausible explanation for the wealth of astrophysical and cosmological evidence for dark matter (DM) is the existence of new elementary particles. Without additional assumptions, however, the allowed mass range for such particles spans almost 50 orders of magnitude, with the lower bound of around 10^{-30} GeV set by quantum mechanics (the De Broglie wavelength must be smaller than the size of known astrophysical objects [1, 2]) and the upper bound of around 10^{19} GeV set by gravity (the mass of a fundamental particle must

be smaller than the Planck mass). Even larger DM masses are possible when considering composite states. This enormous window can be narrowed down significantly, if we consider DM particles that obtain their relic abundance in the early universe by freezing-out from the SM thermal bath. In this case, a lower bound on the DM mass of around 10 MeV is imposed by cosmology, specifically constraints on the number of relativistic degrees of freedom from Big Bang Nucleosynthesis (BBN) and the Cosmic Microwave Background (CMB) [3, 4], and an upper bound of around 100 TeV is imposed by the unitarity requirement that the annihilation cross section of a particle cannot be arbitrarily large [5]. Over the past few decades, the central part of this range, from a few GeV to a few TeV, has been the target of a large number of direct and indirect detection experiments and collider searches, and their null results have strongly constrained the corresponding DM models [6, 7]. For many models, the leading constraints come from direct detection experiments searching for nuclear recoils, which however rapidly lose sensitivity for DM particles below the GeV scale, because the typical kinetic energy of such particles lies below the detector threshold.

In the present work we therefore focus on sub-GeV thermal DM particles. This mass range has traditionally received less attention because of the Lee-Weinberg bound [8], which states that for sub-GeV DM particles the known interactions of the Standard Model (SM) are insufficient to reproduce the observed DM relic abundance through thermal freeze-out. In recent years, however, many new DM models have been developed, which – in addition to the DM particle – feature a new interaction, mediated for example by the gauge boson of a new $U(1)'$ gauge group, called dark photon (for a review see for example ref. [9]). At the same time, direct detection experiments have substantially improved their sensitivity to sub-GeV DM particles by lowering their thresholds for nuclear recoils and searching for electron recoil signatures [10], while accelerator experiments have performed various dedicated searches for dark photon signals in visible and invisible final states [11]. In combination, these developments make sub-GeV thermal DM one of the most exciting frontiers of particle physics [12].

Nevertheless, models of sub-GeV DM face a key challenge, which is that they need to satisfy strong constraints on the DM annihilation cross section from the CMB [13, 14] and, as recently pointed out in ref. [15], from searches for X-ray emission. There are essentially three ways to evade these constraints: by considering a strongly velocity-dependent annihilation cross section arising for example from p -wave suppression [16] or resonant enhancement [17, 18], by allowing for a particle-antiparticle asymmetry suppressing annihilation rates in the present universe [19], or by considering DM particles that only constitute a fraction f of the total DM density, such that annihilation signals are suppressed proportional to f^2 even in the absence of an asymmetry. In the present work we consider all three possibilities simultaneously and determine which ones are favoured or disfavoured by data.¹

A key finding of our analysis is that these solutions only work in special regions of parameter space, which may face other constraints or require substantial tuning. To study this interplay of different constraints and parameters it becomes necessary to explore the full parameter space of sub-GeV DM models. This approach differs from the one commonly adopted in the literature [20–23], where certain parameter combinations (such as the ratio of DM to dark photon mass or the dark fine-structure constant) are fixed to specific bench-

¹Another possibility would be to consider alternative ways for DM particles to obtain their relic abundance, such as secluded or forbidden annihilations, or non-thermal production via the freeze-in mechanism. These possibilities imply however considerably smaller couplings that are much harder to probe experimentally and therefore outside the scope of the present work.

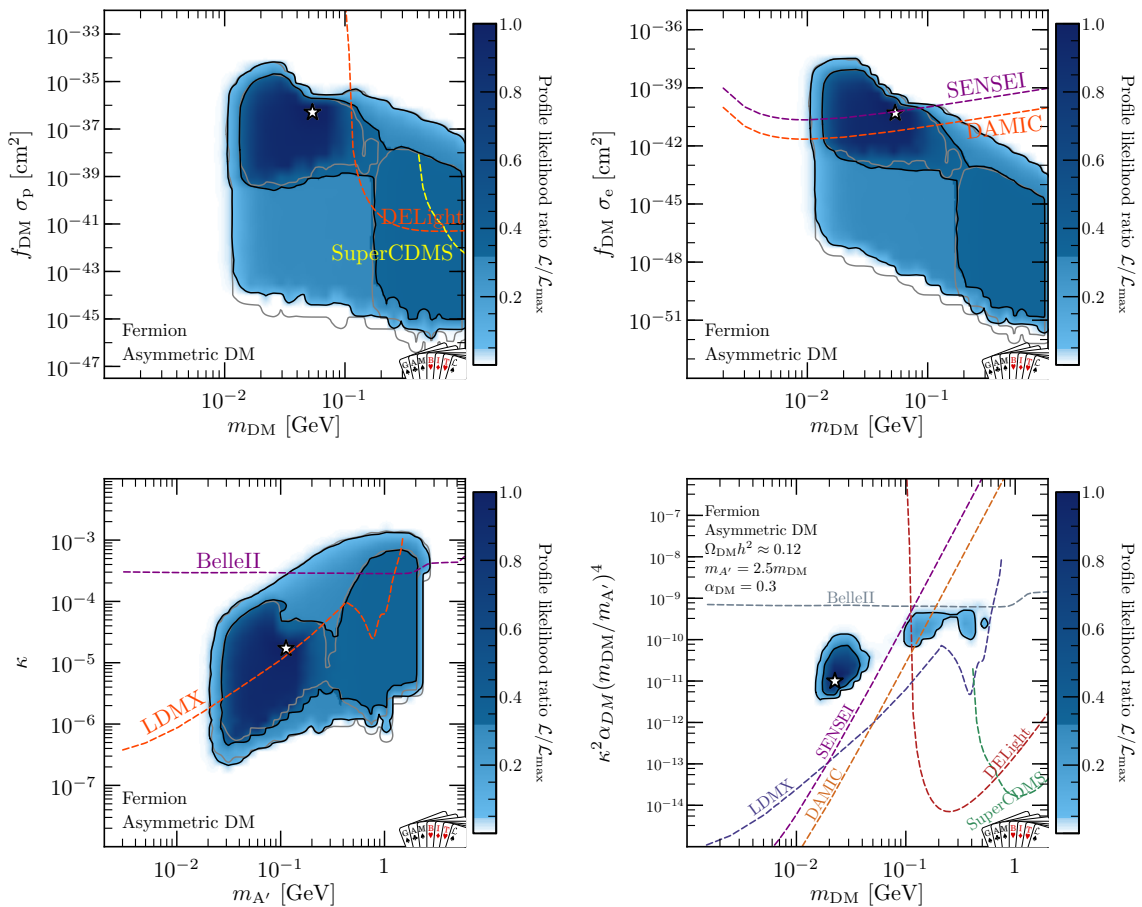


Figure 1. Allowed parameter regions for asymmetric fermionic DM, with the star indicating the best-fit point, compared to the projected sensitivities of various experiments. The different panels show the rescaled DM-nucleus scattering cross section versus the DM mass (top-left), the rescaled DM-electron scattering cross section versus the DM mass (top-right) and the kinetic mixing parameter versus the dark photon mass (bottom-left). In the bottom-right panel we have fixed $m_{A'} = 2.5 m_{\text{DM}}$ and $\alpha_{\text{DM}} = 0.3$, and we show constraints in terms of the effective coupling $\kappa^2 \alpha_{\text{DM}} (m_{\text{DM}}/m_{A'})^4$ versus the DM mass.

mark values. In many cases the most interesting parameter regions can only be found when departing from these benchmark points [24].

The goal of the present work is to perform global fits of scalar and fermionic sub-GeV DM particles coupled to dark photons in order to compare different models and identify the viable regions of parameter space. For this purpose we calculate likelihoods for a wide variety of results from laboratory experiments, astrophysical observations and cosmological data and then perform parameter scans over all model parameters simultaneously. The results can then be analysed in the framework of frequentist or Bayesian statistics, in order to determine which models are disfavoured or preferred by data. This process can be greatly simplified using the GAMBIT global fitting framework v2.5.0 [25–28], which has previously been applied to various DM models [29–34] and other BSM scenarios [35, 36].

Executive summary. For the case of fermionic DM, we find that some tuning of the parameters, in particular the mass ratio of dark photon and DM, is needed to satisfy all constraints. This tuning can be significantly relaxed when including an asymmetry, making it possible in particular to achieve large self-interaction cross sections that can be probed with astrophysical observations. From the Bayesian viewpoint, we find a substantial preference for the model with asymmetry over the symmetric model, which does however depend on the choice of priors. The scalar DM model naturally evades indirect detection constraints, leading to larger allowed parameter regions (and correspondingly larger Bayes factors) in the symmetric case. For both asymmetric fermionic DM and symmetric scalar DM we find that the benchmark points most commonly used in the literature are already in considerable tension with data. We therefore propose a new benchmark point that is consistent with all current constraints and provides an attractive target for future experiments.

Our main findings are summarized in figure 1, which shows the allowed parameter regions for asymmetric fermionic DM in terms of different model parameters and observables compared to the projected sensitivities of various experiments (the corresponding results for scalar DM will be presented in figure 18 and discussed in section 5). In the bottom-right panel we have fixed two of the model parameters to the proposed benchmark values. Doing so leads to a more restricted parameter space, which can be fully probed by next-generation experiments.

Outline. The remainder of the work is structured as follows. In section 2 we introduce the models of sub-GeV DM that we will study and derive the relevant cross sections and decay widths in terms of the model parameters. Section 3 is dedicated to a detailed discussion of all likelihoods that constrain the parameter spaces under consideration. In section 4, we then describe the various parameter scans that we perform and present the corresponding results. We discuss the implications for future DM searches in section 5. Our conclusions are summarized in section 6. Additional technical details are provided in appendices A–C, while additional figures with results from our scans are provided in appendix D. Details regarding the implementation in GAMBIT can be found in appendix E.

2 Models of sub-GeV dark matter

We consider the gauge boson of a new $U(1)'$ gauge group, called the dark photon A' , which obtains a mass $m_{A'}$ via the Stueckelberg mechanism [37].² Couplings of the dark photon to SM particles arise from kinetic mixing with the SM hypercharge field B [38, 39]:

$$\mathcal{L} \supset -\frac{\kappa}{2 \cos \theta_w} \hat{A}'^{\mu\nu} \hat{B}_{\mu\nu}, \quad (2.1)$$

where $X^{\mu\nu} = \partial^\mu X^\nu - \partial^\nu X^\mu$ with $X = \hat{A}', \hat{B}$ is the field-strength tensor before diagonalisation, θ_w denotes the weak mixing angle and κ the kinetic mixing parameter. After electroweak symmetry breaking, we can transform the fields to mass eigenstates with canonical kinetic

²It is of course also possible to generate the dark photon mass through a dark Higgs mechanism. This does not affect the phenomenology of dark photons as long as the dark Higgs boson is sufficiently heavy and sufficiently weakly coupled to the SM Higgs boson. The DM phenomenology, on the other hand, can become more complicated, if the dark Higgs field also couples to the DM particle, such that spontaneous symmetry breaking contributes to its mass. We do not consider this possibility further in the present work.

terms. For $m_{A'} \ll m_Z$ the Lagrangian of the A' is then given by

$$\mathcal{L}_{\text{int}} = -\frac{1}{2}m_{A'}^2 A'^\mu A'_\mu - \frac{1}{4}A'^{\mu\nu} A'_{\mu\nu} - \kappa \epsilon A'^\mu \sum_f q_f \bar{f} \gamma_\mu f, \quad (2.2)$$

where f denote the SM fermions and q_f denotes their electric charges.

We furthermore consider a DM candidate with mass $m_{\text{DM}} < m_{A'}/2$ in the sub-GeV range, which can either be a complex scalar Φ or a Dirac fermion ψ , that couples to the dark photon. The corresponding additions to the Lagrangian are given by

$$\mathcal{L}_\Phi = |\partial_\mu \Phi|^2 - m_{\text{DM}}^2 |\Phi|^2 + i g_{\text{DM}} A'^\mu [\Phi^* (\partial_\mu \Phi) - (\partial_\mu \Phi^*) \Phi] - g_{\text{DM}}^2 A'_\mu A'^\mu |\Phi|^2, \quad (2.3)$$

$$\mathcal{L}_\psi = \bar{\psi} (i \not{\partial} - m_{\text{DM}}) \psi + g_{\text{DM}} A'^\mu \bar{\psi} \gamma_\mu \psi. \quad (2.4)$$

We note that in the absence of a dark Higgs mechanism, the couplings of a massive fermion ψ must be vector-like, i.e. there is no axial-vector coupling.

Since in both cases the DM particle is different from its anti-particle, there may be an asymmetry between their respective number densities, which we denote by [19]

$$\eta_{\text{DM}} \equiv \frac{n_\chi - n_{\bar{\chi}}}{s}, \quad (2.5)$$

where $\chi = \Phi, \psi$ and s denotes the entropy density of the universe. In the absence of processes that violate entropy conservation or DM number conservation, η_{DM} is constant throughout the evolution of the universe. The two models that we consider therefore have 5 parameters each: $m_{A'}$, m_{DM} , κ , g_{DM} and η_{DM} .

The main difference between the two models lies in their annihilation cross section. For scalar DM, s -wave annihilation via an s -channel dark photon is forbidden because of angular momentum conservation, which means that the leading contribution to the annihilation cross section in the non-relativistic limit scales with the DM velocity v as v^2 , such that indirect detection constraints are largely absent [16, 40]. For Dirac DM, on the other hand, s -wave annihilation is allowed, such that the annihilation cross section scales as v^0 , and indirect detection constraints exclude large parts of the parameter space where the observed DM relic abundance can be reproduced.

Nevertheless, there are three ways in which the fermionic model can evade indirect detection constraints. First, the annihilation cross section relevant for DM freeze-out in the early universe may be resonantly enhanced relative to the annihilation cross section relevant in the present universe if the resonance parameter

$$\epsilon_R \equiv \frac{m_{A'}^2 - 4m_{\text{DM}}^2}{4m_{\text{DM}}^2} \quad (2.6)$$

is much smaller than unity: $\epsilon_R \ll 1$ [17, 41]. Second, in the presence of a particle- antiparticle asymmetry, only the symmetric component can annihilate, which leads to a strong suppression of indirect detection signals if the asymmetric component dominates. Finally, we may consider the case where the DM particle under consideration constitutes only a fraction $f_{\text{DM}} < 1$ of the total DM abundance. In our scans we will comprehensively explore all three possibilities.

2.1 Decays, annihilations and self-interactions

In our model there are three competing decay modes of the dark photon: leptonic, hadronic and invisible decays. The leptonic decay width is given by $\Gamma_{\text{lep}} = \sum_{\ell} \Gamma_{\ell\ell}$ with $\ell = e, \mu, \tau$ and

$$\Gamma_{\ell\ell} = \frac{\kappa^2 e^2 m_{A'}}{12\pi} \sqrt{1 - \left(\frac{2m_{\ell}}{m_{A'}}\right)^2} \left(1 + \frac{2m_{\ell}^2}{m_{A'}^2}\right). \quad (2.7)$$

The hadronic decay width can be expressed in terms of the ratio $R(\sqrt{s}) = \sigma(e^+e^- \rightarrow \text{hadrons})/\sigma(e^+e^- \rightarrow \mu^+\mu^-)$ via off-shell SM photons with centre-of-mass energy $\sqrt{s} = m_{A'}$ [42–44]:

$$\Gamma_{\text{had}} = R(m_{A'})\Gamma_{\mu\mu}. \quad (2.8)$$

For certain experimental constraints it may be interesting to split Γ_{had} into different exclusive final states, the most relevant of which are $\pi^+\pi^-$ and K^+K^- . We obtain the corresponding branching ratios from DARKCAST [43], which provides a data base of different models of light gauge bosons that has been interfaced with GAMBIT.

Finally, the invisible decay width (to DM particles) is given by [41]

$$\Gamma_{\text{inv}} = \begin{cases} \frac{g_{\text{DM}}^2 m_{A'}}{48\pi} \left(1 - \frac{4m_{\text{DM}}^2}{m_{A'}^2}\right)^{3/2} & \text{scalar DM,} \\ \frac{g_{\text{DM}}^2 m_{A'}}{12\pi} \left(1 - \frac{4m_{\text{DM}}^2}{m_{A'}^2}\right)^{1/2} \left(1 + \frac{2m_{\text{DM}}^2}{m_{A'}^2}\right) & \text{fermionic DM.} \end{cases} \quad (2.9)$$

From these contributions we can calculate the total decay width of the dark photon as

$$\Gamma_{A'} = \Gamma_{\text{lep}} + \Gamma_{\text{had}} + \Gamma_{\text{inv}}. \quad (2.10)$$

As we will discuss in more detail below, the kinetic mixing parameter κ is experimentally constrained to be well below 10^{-3} . The DM coupling g_{DM} , on the other hand, may be close to the perturbative bound $\alpha_{\text{DM}} = g_{\text{DM}}^2/(4\pi) < 1$, i.e. $g_{\text{DM}} < \sqrt{4\pi}$. If invisible decays are kinematically allowed, i.e. if $m_{A'} > 2m_{\text{DM}}$, we expect this decay mode to dominate the annihilation cross section with a branching ratio close to 100%. In the opposite regime, where $m_{A'} < 2m_{\text{DM}}$, the dark photon can only decay into SM final states. This latter case is constrained by a wide variety of fixed-target experiments and searches at low-energy colliders, which are difficult to reinterpret due to a complicated dependence of the constraints on the dark photon decay length. In the present work we therefore restrict ourselves to the former case. In terms of the resonance parameter introduced in eq. (2.6), this implies $\epsilon_R > 0$.³

The DM annihilation cross section into charged lepton pairs is given by [41]

$$(\sigma v)_{\ell\ell} = \frac{g_{\text{DM}}^2 \kappa^2 e^2}{(s - m_{A'}^2)^2 + m_{A'}^2 \Gamma_{A'}^2} \frac{(2m_{\ell}^2 + s)(y - 4)}{12\pi(y - 2)} \sqrt{1 - \frac{4m_{\ell}^2}{s}} \quad (2.11)$$

for scalar DM and

$$(\sigma v)_{\ell\ell} = \frac{g_{\text{DM}}^2 \kappa^2 e^2}{(s - m_{A'}^2)^2 + m_{A'}^2 \Gamma_{A'}^2} \frac{(2m_{\ell}^2 + s)(y + 2)}{12\pi(y - 2)} \sqrt{1 - \frac{4m_{\ell}^2}{s}}, \quad (2.12)$$

³For $\epsilon_R \ll 1$ it is conceivable that the visible branching ratio becomes non-negligible due to a strong phase-space suppression for the invisible decay. In our scans we will check explicitly for all parameter points that it is a good approximation to neglect laboratory searches for visible dark photon decays.

for fermionic DM, where $y \equiv s/m_{\text{DM}}^2$. For the annihilation into hadrons, we proceed in analogy to the decay width discussed above and write

$$(\sigma v)_{\text{had}} = (\sigma v)_{\mu\mu} R(\sqrt{s}). \quad (2.13)$$

In principle, DM particles could also annihilate into dark photon pairs, but for the spectrum that we consider ($m_{A'} > 2m_{\text{DM}}$) this decay mode is strongly suppressed and plays a negligible role in the calculation of the DM relic abundance.

To understand the importance of the resonance parameter ϵ_R introduced in eq. (2.6), we define

$$\epsilon = \frac{s - 4m_{\text{DM}}^2}{4m_{\text{DM}}^2} \quad (2.14)$$

as a dimensionless measure of the kinetic energy available in an annihilation process. In the non-relativistic limit, $\epsilon = v_{\text{DM}}^2$, where v_{DM} denotes the velocity of each DM particle in the CM frame. With this definition, the dark photon propagator becomes

$$\frac{1}{(s - m_{A'})^2 + m_{A'}^2 \Gamma_{A'}^2} = \frac{1}{16m_{\text{DM}}^4 (\epsilon - \epsilon_R)^2 + m_{A'}^2 \Gamma_{A'}^2}. \quad (2.15)$$

Hence, we see that for $\epsilon \approx \epsilon_R$ the annihilation cross section receives a resonant enhancement, provided that $m_{A'} \Gamma_{A'} \ll m_{\text{DM}}^2$, whereas the propagator becomes independent of ϵ for $\epsilon \ll \epsilon_R$.

In the temperature range relevant for DM freeze-out, ϵ is typically of order 0.1, whereas for indirect detection one can to very good approximation set $\epsilon \rightarrow 0$ (for DM particles bound to the Milky Way halo, e.g., we have $\epsilon \sim 10^{-6}$). Thus, we require $\epsilon_R \sim 0.1$ in order for annihilations to maximally benefit from resonant enhancement during freeze-out without enhancing indirect detection constraints. Choosing $\epsilon_R \ll 0.1$, on the other hand, has the opposite effect and has been used as a means to *boost* indirect detection signals from thermally produced DM [45, 46]. This is illustrated in figure 2, which shows the value of κ required to reproduce the observed DM relic abundance as well as the bounds on κ from indirect detection and missing energy searches as a function of ϵ_R , for $m_{\text{DM}} = 200$ MeV and $g_{\text{DM}} = 0.02$ (see section 3 for details on both the relic density calculation and the constraints shown in the figure). We observe that for this parameter choice indirect detection constraints imply $3 \cdot 10^{-3} < \epsilon_R < 0.3$. If these constraints are absent (for example due to a non-zero asymmetry), the lower bound on ϵ_R disappears and the upper bound on ϵ_R is somewhat relaxed. Because of its central role in the phenomenology of sub-GeV DM, we will in the following use ϵ_R as an independent model parameter instead of $m_{A'}$.

The self-interactions that affect dynamics in astrophysical systems include those between $\chi\chi$, $\bar{\chi}\bar{\chi}$ and $\chi\bar{\chi}$. The differential elastic scattering cross sections for the fermionic DM model are calculated in the non-relativistic limit and are given by

$$\left(\frac{d\sigma}{d\Omega}\right)_{\psi\psi} = \sigma_0, \quad \left(\frac{d\sigma}{d\Omega}\right)_{\psi\bar{\psi}} = \sigma_0 \left[1 + \frac{12w^2}{(1 - 4w^2)^2 + \Gamma_{A'}^2/m_{A'}^2}\right]. \quad (2.16)$$

where $\sigma_0 \equiv (\alpha_{\text{DM}}^2 m_{\text{DM}}^2)/m_{A'}^4$ and $w \equiv m_{\text{DM}}/m_{A'}$. Note that we have made use of the Born approximation, which is accurate for sufficiently large dark photon masses and perturbative couplings. The differential cross-sections for the scalar DM model in the non-relativistic limit are given by,

$$\left(\frac{d\sigma}{d\Omega}\right)_{\Phi\Phi} = 4\sigma_0, \quad \left(\frac{d\sigma}{d\Omega}\right)_{\Phi\Phi^*} = \sigma_0. \quad (2.17)$$

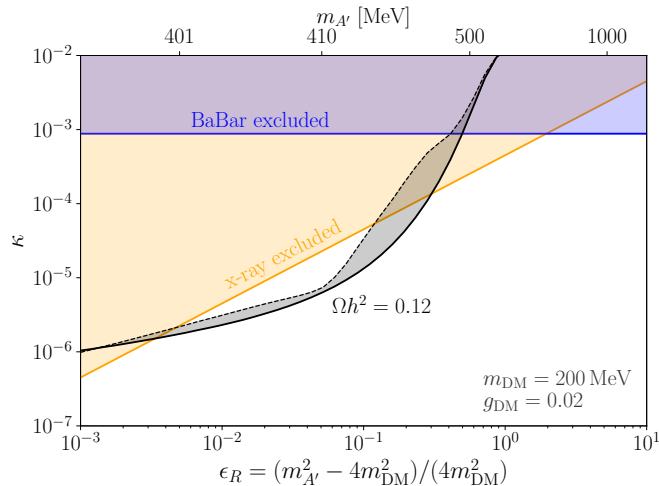


Figure 2. The black line shows the value of the kinetic mixing parameter κ needed to reproduce the observed DM relic abundance $\Omega_{\text{DM}} h^2 = 0.12$ as a function of ϵ_R , for $m_{\text{DM}} = 200$ MeV and $g_{\text{DM}} = 0.02$, when adopting the standard way of calculating the relic density. The shaded region above this line indicates our conservative estimate of the uncertainty on the standard relic density calculation close to very narrow resonances, following ref. [47] (see also appendix A.2). For comparison we show the parameter regions excluded by X-ray observations and by the missing energy search from BaBar. See section 3 for details.

Note that for scalar DM and in the non-relativistic limit, the t -channel dominates over the s -channel even in the resonance region.

2.2 Parameter ranges and priors

To conclude this section, let us briefly state the parameter regions that we will explore in our scans, summarized in table 1. By choice we restrict ourselves to sub-GeV DM particles, i.e. $m_{\text{DM}} < 1$ GeV. A practical reason for this specific upper bound is that there is currently no tool or method to accurately predict the injection spectra from DM annihilations for $1 \text{ GeV} < m_{\text{DM}} < 5 \text{ GeV}$. For the lower bound we take $m_{\text{DM}} > 1$ MeV, well below the bound imposed by cosmological constraints. For the kinetic mixing parameter, a lower bound of $\kappa > 10^{-8}$ is chosen to ensure that dark and visible sector remain in kinetic equilibrium during freeze-out [48], whereas the upper bound is set to $\kappa < 10^{-2}$, well above the experimental constraints. For the DM coupling, on the other hand, we take a lower bound of 10^{-2} , such that $g_{\text{DM}} > \kappa$ everywhere in our parameter space and the dark photon invisible width dominates over the visible one, and impose the perturbativity bound $g_{\text{DM}} < \sqrt{4\pi}$ (see above). Finally, we vary the resonance parameter ϵ_R in the range $[10^{-3}, 8]$, which corresponds to $2m_{\text{DM}} < m_{A'} < 6m_{\text{DM}}$, where the upper bound is chosen to lie well above the parameter range allowed by the relic density requirement (see below).

For the asymmetry parameter, we consider the range

$$0 \leq \frac{m_{\text{DM}}}{1 \text{ GeV}} \eta_{\text{DM}} < 10^{-9}, \quad (2.18)$$

where the lower bound corresponds to the fully symmetric case and the upper bound is obtained from the observation that the asymmetric component alone should not overclose

Table 1. List of model parameters and their ranges. For frequentist scans, the prior is only used to determine the sampling strategy. Our scans also include several nuisance parameters as discussed in the text. The likelihoods that we consider are presented in section 3 and summarized in appendix E.

Parameter name	Symbol	Unit	Range	Prior
Kinetic mixing	κ	–	$[10^{-8}, 10^{-2}]$	logarithmic
Dark sector coupling	g_{DM}	–	$[10^{-2}, \sqrt{4\pi}]$	logarithmic
Asymmetry parameter	η_{DM}	–	$[0, 10^{-9} \text{ GeV}/m_{\text{DM}}]$	linear
Dark matter mass	m_{DM}	MeV	$[1, 1000]$	logarithmic
Dark photon mass <i>or</i>	$m_{A'}$	MeV	$[2, 6000]$ with $m_{A'} \geq 2m_{\text{DM}}$	logarithmic
Resonance parameter	ϵ_R	–	$[10^{-3}, 8]$	logarithmic

the universe. The chosen parameter range for $\eta_{\text{DM}}m_{\text{DM}}$ implies $\Omega_{\text{DM}}h^2 < 0.275$ for the total cosmological DM density, which extends well beyond the observational bound $\Omega_{\text{DM,obs}}h^2 \leq 0.12$, see section 3.1.1.

For our Bayesian scans, we need to specify the prior probabilities in addition to the prior ranges. Since the couplings and DM mass span several orders of magnitude with no preferred scale, we choose logarithmic priors. The parameter ϵ_R however is not a fundamental parameter and therefore not suitable for defining the prior. In our Bayesian scans, we therefore instead take a logarithmic prior on $m_{A'}$ between 2 MeV and 6 GeV, removing all points with $m_{A'} < 2m_{\text{DM}}$ at the prior level. We note that this introduces a bias towards smaller DM masses in the scans, for which there is a larger prior volume in $m_{A'}$. Finally, when including the asymmetry parameter, we choose a flat prior on $\eta_{\text{DM}}m_{\text{DM}}$. The reason for choosing this particular combination of parameters is that it directly enters the relic density calculation, such that the prior range can be restricted by the observed DM relic abundance, see section 3.1.1. A flat prior is chosen such that the symmetric case $\eta_{\text{DM}} = 0$ is included in the scan but does not dominate the prior volume.

Finally, we include three nuisance parameter in our scans, namely the local DM density ρ_0 and the velocity dispersion v_0 and escape velocity v_{esc} of the local DM velocity distribution in the Standard Halo Model. Following previous GAMBIT studies, we allow for ρ_0 to take a rather broad range of values to reflect the spread of different results from the literature, rather than the quoted uncertainty of any individual measurement. Specifically, we take a log-normal distribution with mean $\mu = 0.4 \text{ GeV cm}^{-3}$ and spread $\sigma = 0.15 \text{ GeV cm}^{-3}$. To avoid extreme values, the parameter range is restricted to $0.2 \text{ GeV cm}^{-3} \leq \rho_0 \leq 0.8 \text{ GeV cm}^{-3}$. The velocity parameters are constrained through measurements to $v_0 = 240 \pm 8 \text{ km s}^{-1}$ [49] and $v_{\text{esc}} = 528 \pm 25 \text{ km s}^{-1}$ [50]. All other astrophysical parameters (such as the peculiar motion of the Sun) are fixed to the default parameters of the respective likelihood codes as described in ref. [26].

3 Constraints and likelihoods

In this section we discuss the relevant constraints on the models under consideration, and how we obtain and implement the corresponding likelihoods. The constraints can be divided into four categories: cosmological constraints (section 3.1) from the CMB and from BBN,

astrophysical constraints (section 3.2) from X-rays and observations of the Bullet cluster, accelerator constraints (section 3.3) from beam-dumps and electron-positron colliders and direct detection constraints (section 3.4) from searches for electron and nuclear recoils.

3.1 Cosmological constraints

3.1.1 Relic density

To calculate the DM relic density from thermal freeze-out, we pass the annihilation cross sections from eqs. (2.12) and (2.13) to DARKSUSY v6.4 [51], which performs the thermal averaging, taking special care of centre-of-mass energies close to the dark photon mass and hadronic resonances. DarkSUSY then solves the Boltzmann equation describing the number density of DM particles (including a potential asymmetry η_{DM} , see appendix A for details about this newly added feature) in order to return the present-day abundance of DM particles and anti-particles $\Omega_\chi h^2$ and $\Omega_{\bar{\chi}} h^2$, where $\chi = \phi, \psi$. The sum of these numbers can then be compared to the Planck measurement [14]

$$\Omega_{\text{DM,obs}} h^2 = 0.120 \pm 0.001 \quad (3.1)$$

in order to define the relative cosmological abundance

$$f_{\text{DM}} \equiv \frac{\Omega_{\text{DM}} h^2}{\Omega_{\text{DM,obs}} h^2} \equiv \frac{\Omega_\chi h^2 + \Omega_{\bar{\chi}} h^2}{\Omega_{\text{DM,obs}} h^2}. \quad (3.2)$$

In our analysis we will consider two possible interpretations of this result. The first is that the predicted abundance must match observations, i.e. $f_{\text{DM}} = 1$ within observational and theoretical uncertainties.⁴ The second option is to allow for the possibility that the DM particles under consideration constitute only a DM sub-component, i.e. we implement a one-sided likelihood that penalises $f_{\text{DM}} > 1$ according to the observational and theoretical uncertainty, but does not penalise $f_{\text{DM}} < 1$. If the observed DM abundance is not saturated, we rescale the local DM density ρ_{DM} under the assumption that f_{DM} is constant everywhere, i.e.

$$\rho_{\text{DM}} \rightarrow f_{\text{DM}} \rho_{\text{DM}}. \quad (3.3)$$

Constraints on the DM-nucleon and DM-electron scattering cross sections from direct detection experiments are therefore relaxed by a factor f_{DM}^{-1} .

For observations that probe the DM annihilation cross sections, we furthermore need to account for the particle-antiparticle asymmetry. For this purpose we define the symmetric DM fraction as⁵

$$f_{\text{sym}} \equiv \frac{2 \Omega_{\bar{\chi}} h^2}{\Omega_{\text{DM,obs}} h^2} = f_{\text{DM}} - \eta_{\text{DM}} m_{\text{DM}} \frac{s_0 h^2}{\rho_{\text{DM,obs}} h^2} \leq f_{\text{DM}}, \quad (3.4)$$

⁴For the theoretical uncertainty we assume 10%. This is significantly larger than the precision achieved by DarkSUSY, for the annihilation cross sections of our model, when solving the standard Boltzmann equation [52] adapted to the case with $\eta_{\text{DM}} > 0$. In the presence of very narrow resonances as in our models, however, the standard Boltzmann equation can underestimate the relic density by a much larger factor [47, 53]. As already indicated in figure 2, this is particularly relevant for $\epsilon_R \sim \mathcal{O}(0.1)$. We refer to appendix A.2 for a more detailed discussion, demonstrating that these complications do not affect our results and conclusions based on *scans* over the parameter space (which we perform by using the numerically much faster standard approach, deliberately choosing a ‘too large’ overall theoretical uncertainty in view of this discussion).

⁵Here we assume that η_{DM} is positive, i.e. that we define particles to be the more abundant component and anti-particles to be the less abundant component.

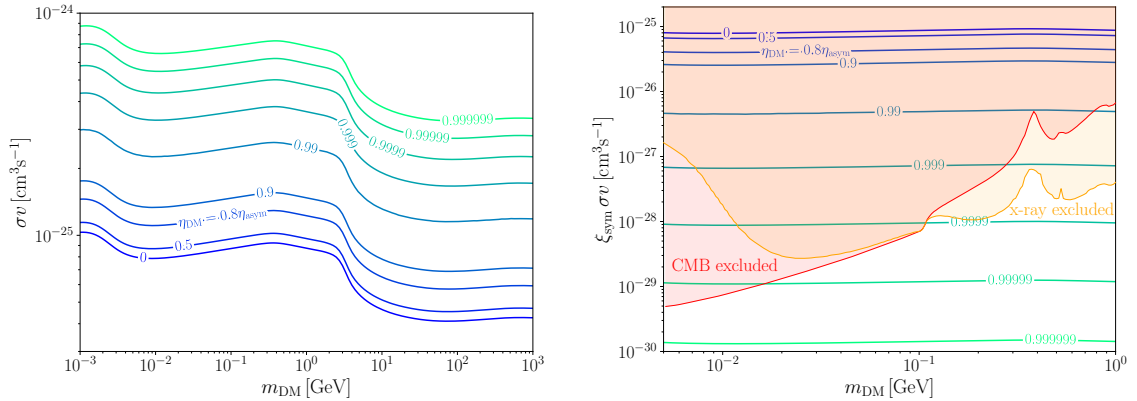


Figure 3. Left: constant annihilation cross section σv required to reproduce the observed DM abundance $\Omega_{\text{DM}} h^2 = 0.12$ as a function of the DM mass for different values of the asymmetry parameter η_{DM} , with η_{asym} defined in eq. (3.5). Relic density calculations have been performed with DARKSUSY v6.4 [51]. Right: corresponding rescaled annihilation cross section $\xi_{\text{sym}} \times \sigma v$ relevant for indirect detection, see eq. (3.6), compared to the constraints on the fermionic DM model from X-rays and the CMB.

where $s_0/\rho_{\text{DM,obs}} \approx 2.755 \times 10^8 (\Omega_{\text{DM,obs}} h^2)^{-1} \text{GeV}^{-1}$. We note that the asymmetry parameter introduced in eq. (2.5) must satisfy the inequality

$$\eta_{\text{DM}} \leq \frac{4.33 \times 10^{-10} \text{GeV}}{m_{\text{DM}}} \equiv \eta_{\text{asym}}(m_{\text{DM}}), \quad (3.5)$$

where η_{asym} denotes the value of η_{DM} for which the asymmetric component alone saturates the relic density. Compared to the fully symmetric case, indirect detection constraints are relaxed by a factor

$$\xi_{\text{sym}} \equiv \frac{n_{\chi} n_{\bar{\chi}}}{\frac{1}{4}(n_{\chi} + n_{\bar{\chi}})^2} = \frac{f_{\text{sym}}}{f_{\text{DM}}} \left(2 - \frac{f_{\text{sym}}}{f_{\text{DM}}} \right), \quad (3.6)$$

which may be tiny if the symmetric component efficiently annihilates away [54, 55]. Of course, indirect detection rates still scale with the *local* DM density as ρ_{DM}^2 (as long as both f_{DM} and ξ_{sym} are constant everywhere).

In figure 3 (left panel) we show the (velocity-independent) annihilation cross section needed to reproduce the observed DM relic abundance $\Omega h^2 = 0.12$ for different values of η_{DM} . We find that η_{DM} needs to be very close to η_{asym} in order to allow for annihilation cross sections well above the standard thermal cross section (corresponding to $\eta_{\text{DM}} = 0$). For a given value of η_{DM} , the mass dependence of these curves reflects as usual the different number of relativistic degrees of freedom in the SM heat bath during DM freeze-out. In the right panel we show the corresponding effective annihilation cross section $\xi_{\text{sym}} \times \sigma v$ that determines the annihilation rate relevant for indirect detection constraints. For comparison, we also indicate the parameter regions excluded by CMB constraints and X-ray constraints, see below, for the fermionic DM model.

3.1.2 Relativistic degrees of freedom

DM particles can either increase or decrease the effective number of relativistic degrees of freedom N_{eff} , depending on their properties: if their mass is close to the MeV scale, they

may still be semi-relativistic at the time when neutrinos freeze out, giving a non-negligible contribution to the (radiation) energy density and thus increasing N_{eff} . On the other hand, residual DM annihilations into electrons after neutrino decoupling would raise the photon temperature relative to the one of neutrinos, and as a result reduce N_{eff} .

To calculate the impact of these effects on the abundances of light elements, we make use of the GAMBIT interface with ALTERBBN v2.2 [56], which provides routines to study the effects of DM annihilations. More concretely, ALTERBBN returns the abundances of ${}^4\text{He}$ and D, which are then compared to observations in order to calculate the likelihood as described in the CosmoBit documentation [27] (see also ref. [36] for a discussion of the most recent data). AlterBBN also returns the neutrino temperature at the end of BBN, which can be translated into the value of N_{eff} relevant for recombination.

For the CMB constraint on N_{eff} , we adopt the likelihood provided by the Planck collaboration [14]:

$$N_{\text{eff}} = 2.99 \pm 0.17, \quad (3.7)$$

using the combination TT,TE,EE+lowE+lensing +BAO. We find that in practice the constraints from BBN and CMB are very similar and exclude DM masses below about 10 MeV, in agreement with ref. [4].

3.1.3 Exotic energy injection

Residual DM annihilations can lead to an injection of exotic energy into the photon-baryon plasma that may spoil the successful predictions of recombination. The rate of injected energy per unit volume depends on the effective parameter [57]

$$p_{\text{ann}} = \frac{f_{\text{DM}}^2 \xi_{\text{sym}}}{2} f_{\text{eff}} \frac{(\sigma_{\text{ann}} v)_0}{m_{\text{DM}}}. \quad (3.8)$$

Here the subscript 0 indicates the $v \rightarrow 0$ limit, which is a good approximation for the temperature range relevant for recombination.

The main challenge is to accurately calculate the fraction f_{eff} of energy deposited in the plasma, which depends both on the DM mass and the final state. Fortunately, the public code HAZMA v2.0 [58, 59] provides the yields of injected γ -rays and positrons for annihilations via a vector mediator with kinetic mixing as a function of the DM mass. These spectra have been obtained under the assumption of vector meson dominance from dedicated simulations of hadron production in DM annihilations using HERWIG4DM [60]. We have tabulated these spectra and made them available in DARKSUSY, as part of the v6.4 release, in order to provide them to DARKAGES [61] and calculate f_{eff} at every point in parameter space (see ref. [32] for further details).

One could in principle calculate the impact of a given p_{ann} on the CMB temperature anisotropies while varying the cosmological parameters. However, there are no significant degeneracies between p_{ann} and other parameters, which makes it possible to calculate a marginalised Planck likelihood that depends only on p_{ann} . Such a likelihood has been obtained in ref. [32] and can be directly used in the present context. The resulting constraint is shown in the right panel of figure 3. The various features above 100 MeV are a direct consequence of the varying hadronic branching ratio of the dark photon, which leads to variations in f_{eff} .

Finally, we note that for the smallest DM masses that we consider, there may be relevant constraints from DM annihilations after the end of BBN, leading to the photodisintegration

of deuterium and helium-3 [3]. However, it was argued in ref. [17] that this constraint is only relevant for parameter points with very large resonant enhancement (corresponding to $\epsilon_R < 10^{-3}$). These parameter regions are not the focus of the present study, and we therefore leave a detailed study of constraints from photodisintegration to future work [62].

3.2 Astrophysical constraints

X-ray constraints

Assuming that DM is not fully asymmetric, it may annihilate to SM particles, producing detectable gamma-ray or X-ray signals. Annihilation directly to photons would lead to a distinctive monochromatic line signal at the DM mass, while annihilation to quarks, leptons and mesons can result in a broad photon spectrum resulting from the subsequent particle fragmentation and decay. Searches for both signals can set strong limits on sub-GeV DM (for example refs. [63, 64]). However, gamma-ray searches for sub-GeV dark matter are limited by the so-called “MeV gap” between keV-range experiments like SPI aboard the INTEGRAL satellite [65], and Fermi-LAT at GeV energies [66]. Numerous experiments have been proposed to fill in this gap in coverage; for a detailed review, see ref. [67].

There are, however, also secondary signals of dark matter annihilation: energetic charged annihilation products can undergo inverse Compton scattering on starlight or CMB photons, thereby producing keV-scale X-rays. Thus, data from INTEGRAL can be used to constrain MeV-scale dark matter by searching for this flux of upscattered photons, as studied in ref. [68]. This analysis was extended in ref. [15] to include data from not just INTEGRAL [69], but also NuSTAR [70–73], XMM-Newton [74, 75], and Suzaku [76]. The resulting analysis places stringent limits on dark matter annihilation to electrons down to 1 MeV, and annihilation to muons and charged pions down to the respective threshold. The authors of ref. [15] have generously provided the likelihoods used in their analysis for each of these annihilation channels. We do not attempt to combine these likelihoods, i.e. we conservatively only include the final state giving the strongest constraint, which is typically e^+e^- .

We note that ref. [77] recently updated the results of ref. [15] using a more realistic treatment of cosmic ray propagation including spatial diffusion and reacceleration. While the resulting limits can be substantially stronger, especially at low mass, they depend on the model and parameters used to describe cosmic ray transport, which carry large uncertainties. We therefore conservatively use the earlier result [15] in the present work.

The resulting constraint is shown in the right panel of figure 3. Similar to the CMB case discussed above, we can see the various features resulting from the hadronic branching ratio of the dark photon.

Bullet cluster constraints

Merging galaxy cluster 1E0657-56, otherwise known as the Bullet Cluster, serves as one of the best test beds for DM self-interactions. It comprises a subcluster that passed through the main cluster’s central region along the plane of the sky. X-ray and lensing observations have identified gas and mass distributions with well-separated peaks, implying that feebly interacting DM dominates the clusters’ masses [78–81]. The presence of DM self-interactions would lead to the subcluster DM component experiencing friction as it passes through the main cluster. This would result in decelerating the DM component of the subcluster, such that it lags behind the collisionless galaxies, and cause the subcluster to lose part of its DM mass.

These observables can be used to constrain self-interaction. The offset between DM and galaxy centroids has been used to place the limit $\sigma_0/m_{\text{DM}} < 1.25 \text{ cm}^2\text{g}^{-1}$ [82], although ref. [83] pointed out that the measured offsets are quite sensitive to the methods used, and more recent analyses [84] have obtained slightly weaker bounds. Ref. [82] also used subcluster survival to place the most stringent constraint, $\sigma_0/m_{\text{DM}} < 0.7 \text{ cm}^2\text{g}^{-1}$. The subcluster mass loss is determined by comparing the observed mass-to-light ratios (γ) of the main and the subcluster assuming that they start out with identical γ . However, it has been pointed out that γ increases slowly with total cluster mass [85] and that there is significant scatter in the mass-luminosity relationship [86–88].

In this work, we constrain DM self-interactions by investigating the subcluster survival rather than the DM-galaxy offset. The reason is that the latter can only be studied using numerical simulations, whereas for the former it is possible to derive an analytic estimate for the *evaporation rate* [89], which can be directly applied to asymmetric DM and DM subcomponent to predict the fraction of total mass lost (Δ_{M}) by the subcluster, see appendix B for details. The theoretical prediction for the final subcluster mass-to-light ratio, $\gamma_{\text{f}}^{\text{sub}} = \gamma_{\text{i}}^{\text{sub}}(1 - \Delta_{\text{M}})$, is then compared to the measured subcluster mass-to-light ratio, $\gamma_{\text{obs}}^{\text{sub}} = 179 \pm 11$ [82]. The novelty in our constraint is that we choose to treat the initial subcluster mass-to-light ratio $\gamma_{\text{i}}^{\text{sub}}$ as a nuisance parameter and calculate a marginalized likelihood,

$$\begin{aligned} \log \mathcal{P} &\propto \log \int d\gamma_{\text{i}}^{\text{sub}} \mathcal{L}(\gamma_{\text{f}}^{\text{sub}}) \Pi(\gamma_{\text{i}}^{\text{sub}}) \\ &\propto \log \sum_n \exp \left(-\frac{1}{2} \frac{(\gamma_{\text{obs}}^{\text{sub}} - \gamma_{\text{i},n}^{\text{sub}}(1 - \Delta_{\text{M}}))^2}{(\sigma_{\text{obs}}^{\text{sub}})^2 + \sigma_{\text{theory}}^2} \right) \end{aligned} \quad (3.9)$$

We have implemented two different priors: (i) a Gaussian prior centred around the measured main cluster mass-to-light ratio, $\gamma_{\text{obs}}^{\text{main}} = 214 \pm 13$ [82], and (ii) a log-normal prior fitted to the *i*-band sample extracted from ref. [87]. The likelihoods are constructed using mass-to-light ratios of the subcluster and main cluster within 150 kpc of the total mass peak, in the photometric *i*-band, taken from ref. [82]. The Gaussian prior assumes that the subcluster and main cluster γ 's are initially correlated. Since the measured values are quite close to each other, this approach leads to strong constraints. On the other hand, the log-normal prior makes no assumption of such a correlation and allows much larger initial subcluster mass-to-light ratios, thus leading to an overly conservative constraint.

The marginalized likelihoods for a single DM component with isotropic and velocity-independent self-interaction cross-section are shown in figure 4. The Gaussian prior centred around the main cluster's mass-to-light ratio gives a limit $\sigma_0/m_{\text{DM}} < 1.4 \text{ cm}^2\text{g}^{-1}$ ($\Delta\chi^2 < 3.84$), very similar to the limit obtained in ref. [90] based on similar arguments and assumptions. The log-normal prior is more conservative, as it assumes no correlation between the clusters and instead only considers the general scatter in the mass-luminosity relationships for galaxy clusters. This prior gives a limit $\sigma_0/m_{\text{DM}} < 5.0 \text{ cm}^2\text{g}^{-1}$ ($\Delta\chi^2 < 3.84$). In the following, we will use the likelihood with correlations, because it resembles more closely the treatment found elsewhere in the literature. We note that this likelihood leads to a slight preference for non-zero self-interaction cross section, with a best-fit value around $\sigma_0/m_{\text{DM}} = 0.5 \text{ cm}^2\text{g}^{-1}$. However, this preference is not significant and the constraint is consistent with vanishing self-interactions at the 1σ level.

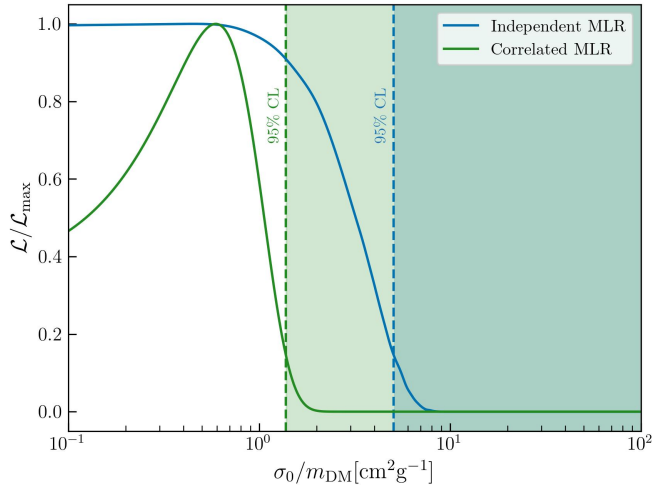


Figure 4. The 95% CL upper limits on the isotropic and velocity-independent self-interaction cross-section, σ_0/m_{DM} , obtained from subcluster survival in the Bullet Cluster. Two different priors are used to marginalize the likelihood over the initial mass-to-light ratio (MLR): the Gaussian prior (green) assumes correlations between the main cluster and sub-cluster initial MLR values; the log-normal prior (blue) assumes no such correlation.

3.3 Accelerator experiments

As discussed in section 2.1, we focus our analysis on parameter regions where the dark photon decays almost exclusively into pairs of DM particles. Constraints on this scenario can come from two types of experiments: searches for missing energy and searches for the scattering of DM particles produced in the dark photon decays. Figure 5 shows the 90 % C.L. exclusion bounds from LSND [91, 92], MiniBooNE electron and nucleon scattering [93], NA64 [94] and BaBar [95] for a complex scalar DM candidate with an example benchmark choice of model parameters. These exclusion bounds are shown from both previous literature results (dashed) and from using the interpolations and scaling techniques implemented in this work (solid). The rest of this section describes these experiments in detail.

LSND and MiniBooNE

Beam dump experiments such as LSND [91, 92] and MiniBooNE [93] aim to produce a relativistic flux of DM particles from interactions between a proton beam and nucleons in a dense target. Neutral mesons such as π^0 and η are produced in these interactions, which then decay producing DM via the chain $\pi^0, \eta \rightarrow \gamma + A'$, $A' \rightarrow \chi\bar{\chi}$ with either $\chi = \psi$ for fermionic DM or $\chi = \Phi$ for scalar DM. The DM particles can then be detected in a downstream detector through DM-nucleon or DM-electron scattering, analogous to underground DM direct detection experiments searching for Galactic DM. The number of expected signal events in the detector is proportional to model parameters g_{DM} and κ , and branching ratios $\text{BR}_{X \rightarrow A'\gamma}$ and $\text{BR}_{A' \rightarrow \chi\bar{\chi}}$:

$$N_\chi \propto \text{BR}_{X \rightarrow A'\gamma} \text{BR}_{A' \rightarrow \chi\bar{\chi}} \kappa^2 g_{\text{DM}}^2 \propto \text{BR}_{A' \rightarrow \chi\bar{\chi}} \kappa^4 g_{\text{DM}}^2, \quad (3.10)$$

where X is a meson produced from beam-target interactions, κ^2 comes from dark photon production, and $\kappa^2 g_{\text{DM}}^2$ from DM scattering in the detector. The number of expected DM

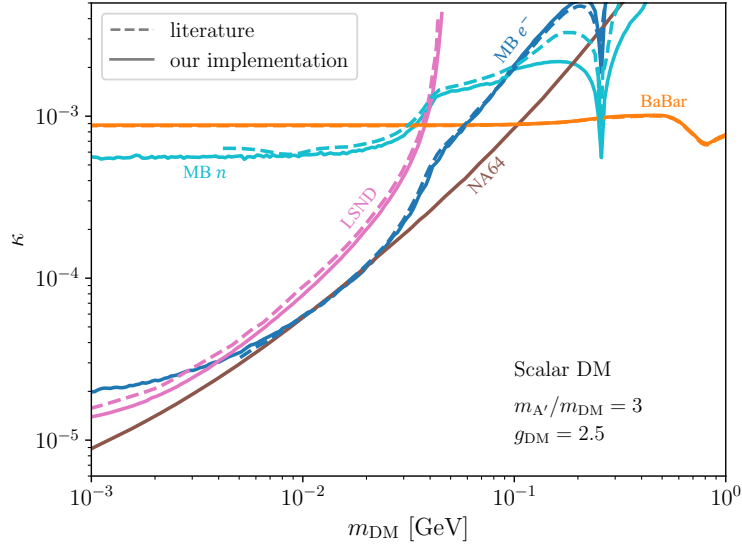


Figure 5. The 90% C.L. exclusion bounds from NA64, LSND, MiniBooNE electron and nucleon scattering, and BaBar experiments which we consider in this analysis, for the case of complex scalar DM with $m_{A'}/m_{\text{DM}} = 3$ and $g_{\text{DM}} = 2.5$. The exclusion bounds are plotted in the κ vs m_{DM} plane, for interpolated simulations used in these global scans (solid curves) in addition to literature values [91–95] for comparison (dashed curves). The NA64 literature values agree exactly with the interpolated values.

signal events is calculated for each model using Monte Carlo simulation software for beam dump experiments, BdNMC [96]. We consider the case where $m_{A'} > 2m_{\text{DM}}$, therefore on-shell contributions to DM production dominate. These simulations are performed on a log-spaced grid of $m_{A'}$ and m_{DM} values at constant values for κ and g_{DM} , which we denote \tilde{g}_{DM} and $\tilde{\kappa}$. From this given set of values, we calculate N_{DM} by scaling the simulated number of events, $\tilde{N}_{\text{DM}} = N_{\text{DM}}(g_{\text{DM}} = \tilde{g}_{\text{DM}}, \kappa = \tilde{\kappa})$, in the following way:

$$N_{\text{DM}}(m_{A'}, m_{\text{DM}}, \kappa, g_{\text{DM}}) = \tilde{N}_{\chi} \left(\frac{\kappa}{\tilde{\kappa}} \right)^4 \left(\frac{g_{\text{DM}}}{\tilde{g}_{\text{DM}}} \right)^2 \text{BR}_{A' \rightarrow \chi\bar{\chi}}(m_{A'}, m_{\text{DM}}, \kappa, g_{\text{DM}}), \quad (3.11)$$

where $\tilde{\kappa}$ and \tilde{g}_{DM} are chosen such that $\tilde{g}_{\text{DM}} \gg \tilde{\kappa}$, and hence $\text{BR}_{A' \rightarrow \chi\bar{\chi}}(m_{A'}, m_{\text{DM}}, \tilde{\kappa}, \tilde{g}_{\text{DM}}) \approx 1$.

We take LSND and MiniBooNE as counting experiments, modelling the likelihood of observing n events, with predicted s signal and b background events, as a Poisson distribution:

$$\mathcal{L} = e^{-(s+b)} \frac{(s+b)^n}{n!}. \quad (3.12)$$

For the case of MiniBooNE, with no excess above the background predictions, we take $n = 0$ and $b = 0$, and s given by the simulated signal value [93]. LSND reported $n = 242$ events which include elastic scattering by neutrinos and potentially DM, with an expected SM background $b = 229 \pm 28$ [91, 92]. We include the background uncertainty by treating b as a nuisance parameter with a Gaussian likelihood that is marginalised over at each parameter point. Figure 5 shows the Mini-BooNE electron scattering (blue), MiniBooNE nucleon scattering (cyan), and LSND electron scattering (pink) 90 % C.L. exclusion bounds.

Note that the literature MiniBooNE nucleon scattering limits are taken from ref. [93], where the treatment of the ρ/ω resonance is different from our approach.

NA64

The NA64 experiment [94] searches for missing energy events of high energy electron collisions with a fixed target, Z , resulting from the production of dark photons via dark bremsstrahlung, $e^- Z \rightarrow e^- Z A'$ and the prompt decay of the dark photon into invisible final states, $A' \rightarrow \chi\bar{\chi}$.

We take results from ref. [94] to calculate the expected number of signal events, N_{DM} , as a function of κ and $m_{A'}$. As long as $m_{A'} > 2m_{\text{DM}}$, dark bremsstrahlung to invisible final states occurs through an on-shell dark photon, thus the process is independent of g_{DM} and m_{DM} . The number of missing energy events is proportional to κ^2 , therefore the results from ref. [94] are re-scaled for the desired κ value. To account for cases where $g_{\text{DM}} \sim \kappa$, when dark photons can also decay visibly, the results are scaled by $\text{BR}_{A' \rightarrow \chi\bar{\chi}}$.

Similarly to the beam dump experiments discussed above, the likelihood of observing n events at NA64 is given by eq. (3.12). No signal events were observed at NA64 [94], hence $n = 0$ and $b = 0$. Exclusion bounds from NA64 at 90 % C.L. are shown in figure 5.

BaBar single-photon search

The BaBar collaboration has used a data set of 53 fb^{-1} of e^+e^- collisions to search for events in which an invisibly decaying dark photon is produced in association with a mono-energetic SM photon [95]. While the event selection cannot be reproduced in detail, ref. [95] provides detailed information on the likelihood for the kinetic mixing parameter κ as a function of the dark photon mass. Moreover, BaBar provides both a Bayesian limit (imposing the prior boundary $\kappa > 0$) and a frequentist limit. With the available information it is possible to implement a detailed likelihood function that accurately reproduces both limits. We note that for dark photons with general branching ratios we need to make the replacement

$$\kappa \rightarrow \kappa \sqrt{\text{BR}_{A' \rightarrow \chi\bar{\chi}}} \quad (3.13)$$

inside the likelihood function, which conservatively assumes that all visible decays have been vetoed by BaBar. We indicate also these limits in figure 5.

Electroweak precision observables

In principle the kinetic mixing parameter κ is constrained by electroweak precision data [97–99]. However, for dark photons that decay dominantly invisibly, the constraints discussed above are much stronger than the direct constraints on κ . We therefore do not include these constraints in our analysis.

Constraints on visibly decaying dark photons

Although our analysis focuses on the case that $g_{\text{DM}} > \kappa$, there are regions of parameter space where the visible branching ratio of the dark photon is non-negligible. This is because the decay of the dark photon into DM is phase-space suppressed in the resonant region ($\epsilon_R \ll 1$). One might worry that in such a case the likelihood implementations described above are insufficient and that additional constraints may arise from searches for prompt or displaced decays of dark photons into visible final states. We therefore check for all points passing all constraints that

- The proper dark photon decay length $c\tau_{A'}$ is shorter than 1 mm, such that searches for long-lived dark photons (for example in beam-dump experiments such as NA62 [100]) are insensitive.
- The visible branching fraction satisfies the constraint $\kappa^2\text{BR}_{A'\rightarrow SM} < 10^{-7}$, such that prompt decays into SM final states are out of reach of the leading experiments such as BaBar [101] and NA48/2 [102].

We find that even though these requirements are very conservative, they are always satisfied in the parameter regions of interest.

3.4 Direct detection

Strong constraints on sub-GeV DM result from searches for DM scattering in ultra-low-background detectors. Only few direct detection experiments achieve sufficiently low energy thresholds to search for sub-GeV DM in nuclear recoils. However, the reach of these experiments can be extended to much smaller masses by searching for electron recoils. Moreover, additional sensitivity can be gained by searching for electrons produced from nuclear recoils via the so-called Migdal effect [103].

Electron recoils

The reference cross section at fixed momentum transfer $q = \alpha m_e$ for DM-electron scattering is given by [104]

$$\sigma_e = \frac{4\mu_{\chi,e}^2 \alpha \kappa^2 g_{\text{DM}}^2}{(m_{A'}^2 + \alpha^2 m_e^2)^2} \quad (3.14)$$

for both scalar and fermionic DM, where $\mu_{\chi,e} \equiv m_{\text{DM}}m_e/(m_{\text{DM}} + m_e) \approx m_e$ is the reduced mass of the DM-electron system.

The leading bounds on σ_e stem from XENON1T [105], SENSEI [106], DarkSide50 [107], PandaX-4T [108], DAMIC-M [109] and SuperCDMS HV [110].⁶ To obtain likelihood functions for these experiments, we have interfaced GAMBIT with the OBSCURA library [112], which provides the atomic response functions following ref. [113] for liquid noble gases and following ref. [114] for semiconductors. Likelihoods are obtained by comparing the background expectation and signal prediction to the observed number of events in each bin and calculating the resulting Poisson likelihood. Details of the likelihood functions and the new GAMBIT interface can be found in appendix E.3.

We show a comparison of the published limits and our implementation in the left panel of figure 6. With the publicly available information it is not possible to reproduce all limits perfectly, in particular close to threshold, where complicated detector effects play an important role. Nevertheless, the leading constraints from SENSEI and PandaX-4T are accurately captured in our implementation.

Nuclear recoils

The DM-proton scattering cross section for vanishing momentum transfer is given by

$$\sigma_p = \frac{4\mu_{\chi,p}^2 \alpha \kappa^2 g_{\text{DM}}^2}{m_{A'}^4} \quad (3.15)$$

⁶The recent results from LZ [111] are difficult to reinterpret in terms of a full likelihood, and are therefore not included in our analysis.

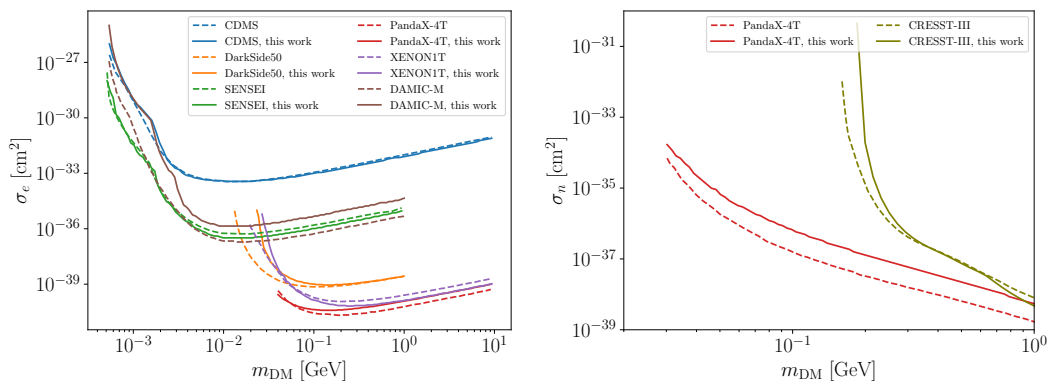


Figure 6. The 90% C.L. exclusion bounds from direct detection experiments with electron recoils on the left and nuclear recoils (including Migdal scattering) on the right. All limits are computed for the case of contact interactions. Dashed lines are the 90% C.L. reported by the experiments, solid lines correspond to our implementation in OBSCURA (electron recoil and Migdal effect) and DDALC (nuclear recoil).

for both scalar and fermionic DM, while the DM-neutron scattering cross section vanishes because the dark photon couples to SM particles proportionally to their charge. As a result, the DM-nucleus cross section is proportional to Z^2 (instead of the commonly assumed scaling proportional to A^2).

The leading constraint on sub-GeV DM from nuclear recoils stems from CRESST-III [115], which we implement using DDALC [30]. However, substantially stronger constraints on the DM-proton scattering cross section can be obtained by exploiting the Migdal effect, which has been implemented in OBSCURA for liquid noble gas detectors following refs. [116–118]. We use this implementation and the electron recoil data discussed above to calculate likelihoods for DarkSide50, XENON1T and PandaX-4T, finding that PandaX-4T gives the strongest constraint.

We show a comparison between the published PandaX-4T bound and our implementation in the right panel of figure 6. For the purpose of comparing to the published bound from PandaX-4T, we set the neutron coupling equal to the proton coupling in this figure. We find that our implementation leads to a considerably weaker constraint than the published result. This is somewhat surprising, given that the underlying data set is the same as for the electron-recoil search, which we are able to reproduce quite well (left panel). This suggests some differences in the theoretical predictions for the Migdal effect, which is affected by large uncertainties in the determination of the electron wave functions that enter in the calculation of the ionisation probabilities [103, 117]. To reflect these uncertainties, we use our (weaker) bound instead of the published one. We also show the CRESST-III bound, which is not subject to these large theoretical uncertainties and can be accurately reproduced away from the threshold.

We mention in passing that in the parameter space that we consider (in particular for $m_{A'} > 2m_{\text{DM}}$) the scattering cross sections can never become large enough for Earth shielding [119, 120] or cosmic-ray upscattering [121] to become relevant. Hence these effects are neglected in our analysis.

4 Results

In this section we present the results from our global fits of fermionic and scalar sub-GeV DM using the likelihoods discussed above. For the fermionic model we consider the case that the DM particle under consideration constitutes a sub-dominant DM component ($\Omega_{\text{DM}}h^2 \leq 0.12$) as well as the case that it is required to reproduce the observed DM abundance within observational and theoretical errors ($\Omega h^2 = 0.12$). In the latter case we either set the asymmetry parameter η_{DM} to zero (symmetric) or include it as an independent parameter in our scans (asymmetric). For the scalar model, indirect detection constraints are much weaker, and we therefore only consider the symmetric case with saturated relic density.

For each of these scenarios we carry out both a frequentist and a Bayesian analysis. The parameter ranges and priors have already been discussed in section 2.2. The exploration of the parameter space is done with the GAMBIT global fitting framework, using Diver [122] with a population size of 38,000 and a convergence threshold of 10^{-6} for frequentist scans and Polychord [123] with 1000 live points and a tolerance of 10^{-10} for Bayesian scans. We have checked that these settings are sufficient to ensure that the scans converge. The results of all scans along with relevant GAMBIT configuration files and an example plotting script are available on Zenodo [124].

4.1 Fermionic dark matter

Frequentist results

Our results for the case of sub-dominant symmetric fermion DM are shown in figure 7. The colour scale represents the likelihood (relative to the maximum \mathcal{L}_{max}), the lines indicate the allowed parameter regions at 68% and 95% confidence level. In each panel, the parameters not shown have been profiled over and the best-fit point is indicated by a white star. We emphasize that the likelihood around the best-fit point is very flat and it's precise position is a result of small numerical fluctuations without deeper physical significance. To guide the eye, we further show the various constraints described in detail in section 3. We make the following observations:

- In the top-left panel we clearly see the impact of the cosmological likelihoods ruling out $m_{\text{DM}} \lesssim 10 \text{ MeV}$ and the indirect detection constraints ruling out $\epsilon_R \gtrsim 0.4$. In other words, the dark photon mass must be tuned to the resonance condition $m_{A'} = 2m_{\text{DM}}$ with approximately 20% precision.
- In the bottom-left panel we see the upper bound $\kappa < 10^{-3}$ imposed by BaBar as well as an increasingly stronger bound towards small DM masses stemming from NA64 (note that the published bounds, which we show for comparison here, are given at 90% C.L.) We also see that κ cannot be arbitrarily small, which is a consequence of the relic density requirement.
- In the top-right panel we see that the dark sector coupling g_{DM} is not strongly constrained and can take values up to the perturbativity bound. For small DM masses, beam-dump experiments become relevant and impose $g_{\text{DM}} \lesssim 1$.
- Finally, in the bottom-right panel, we can see that for increasing g_{DM} the allowed range of κ shrinks towards the upper bound. This is because the relic density requirement is violated if both couplings g_{DM} and κ become small simultaneously (see figure 2).

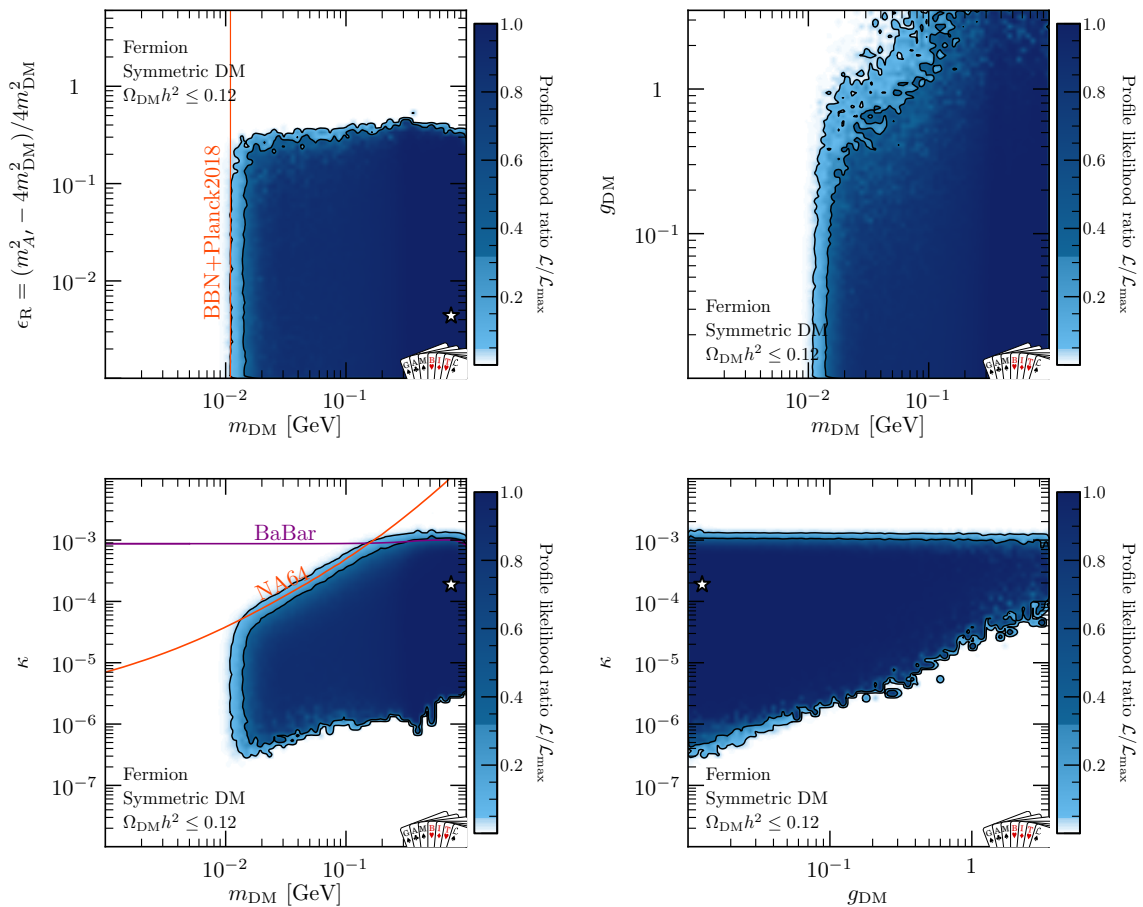


Figure 7. Allowed parameter regions for symmetric fermionic dark matter with $\Omega_{\text{DM}}h^2 \leq 0.12$ in terms of the different model parameters. The color shading indicates the profile likelihood relative to the best-fit point (indicated by a star). Black lines indicate the 1σ and 2σ confidence regions. Coloured lines indicate various experimental and observational constraints (see section 3 for details).

We also point out that the lower bound on κ relaxes slightly for $m_{\text{DM}} \approx 400$ MeV and $m_{\text{DM}} \approx 500$ MeV, leading to noticeable features in the bottom-left panel. The reason is that the centre-of-mass energy of the annihilation process then becomes close to the masses of hadronic bound states (the ω meson and the ϕ meson, respectively), such that the annihilation cross section into hadrons receives a resonant enhancement.

It is furthermore instructive to plot various observables as a function of the DM mass, as shown in figure 8. We can see that in the bulk of the parameter space the DM relic abundance is well below the observed value, such that indirect detection signals (which scale proportional to f_{DM}^2 for symmetric DM) and direct detection signals (which scale proportional to f_{DM}) can be strongly suppressed. Nevertheless, the observed DM relic abundance can be saturated across the entire DM mass range. Both direct and indirect detection experiments place relevant constraints on the parameter space, which can however be evaded by many orders of magnitude when considering sub-dominant dark matter components. However, it turns out that the predicted DM-electron scattering cross section is below current exclusion limits in the entire allowed parameter space.

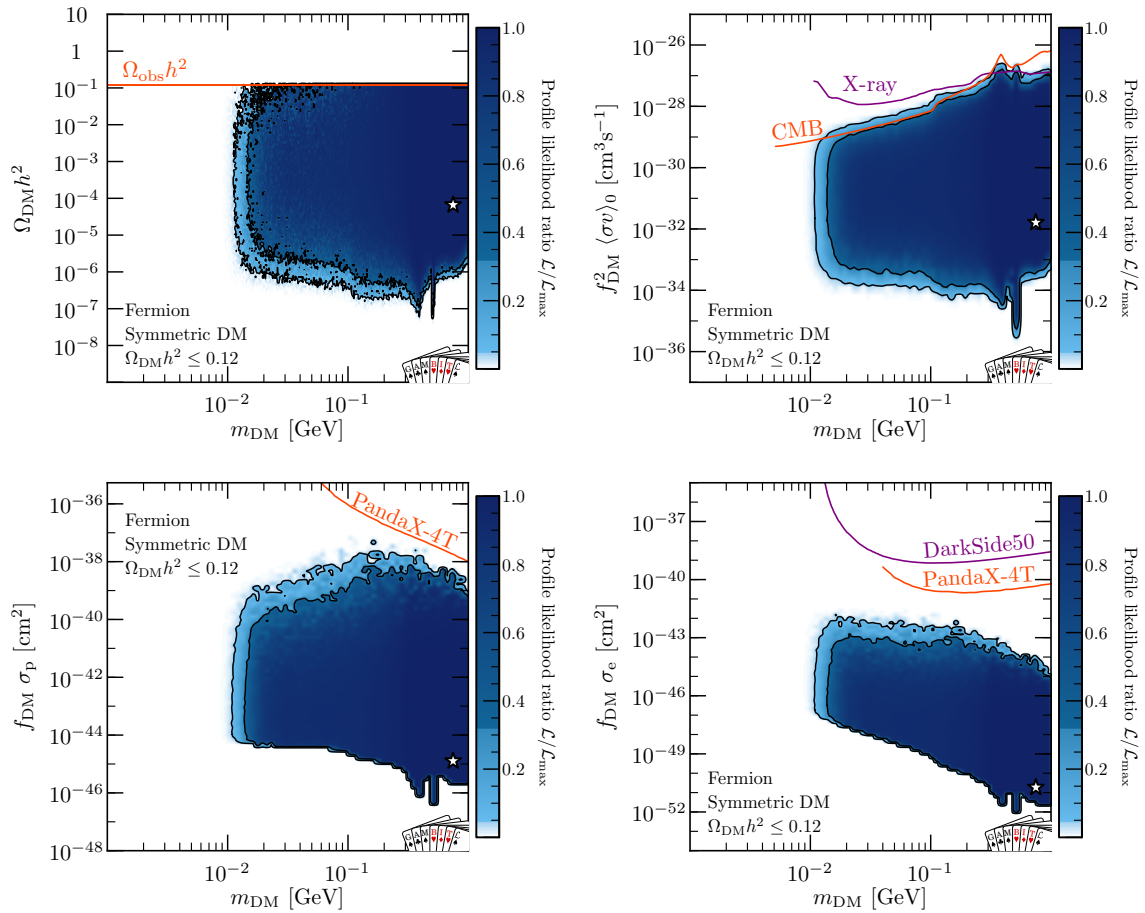


Figure 8. Allowed parameter regions for symmetric fermionic dark matter with $\Omega_{\text{DM}}h^2 \leq 0.12$ in terms of various observables as a function of the DM mass. See caption of figure 7 for details on the various line styles and symbols.

Let us now turn to the case where we require DM to saturate the observed DM relic density. The results of this scan are shown in figure 9. For comparison, we indicate the allowed parameter regions from the previous scan (allowing a sub-dominant DM component) with grey lines. The main difference compared to the previous scan is that there is now a lower bound on the resonance parameter $\epsilon_R \gtrsim 10^{-2}$ in order to evade indirect detection constraints (see figure 2). Moreover, g_{DM} is now constrained to much smaller values in order to avoid very large annihilation cross sections, which would lead to an underabundant DM component with $\Omega_{\text{DM}}h^2 < 0.12$. For the same reason also the largest values of κ are disfavoured. However, in the remaining parameter regions it is possible to satisfy all experimental constraints simultaneously, such that the likelihood of the best-fit point remains largely unchanged relative to the previous case. Correspondingly, the difference in log-likelihood is found to be insignificant: $-2\Delta \log \mathcal{L} = -0.9$.

Because of the small couplings, the remaining allowed regions of parameter space are extremely difficult to probe with laboratory experiments. Both the DM-proton and DM-electron scattering cross sections are orders of magnitude below current limits, and the predicted number of events in the beam-dump experiments that we consider is much smaller

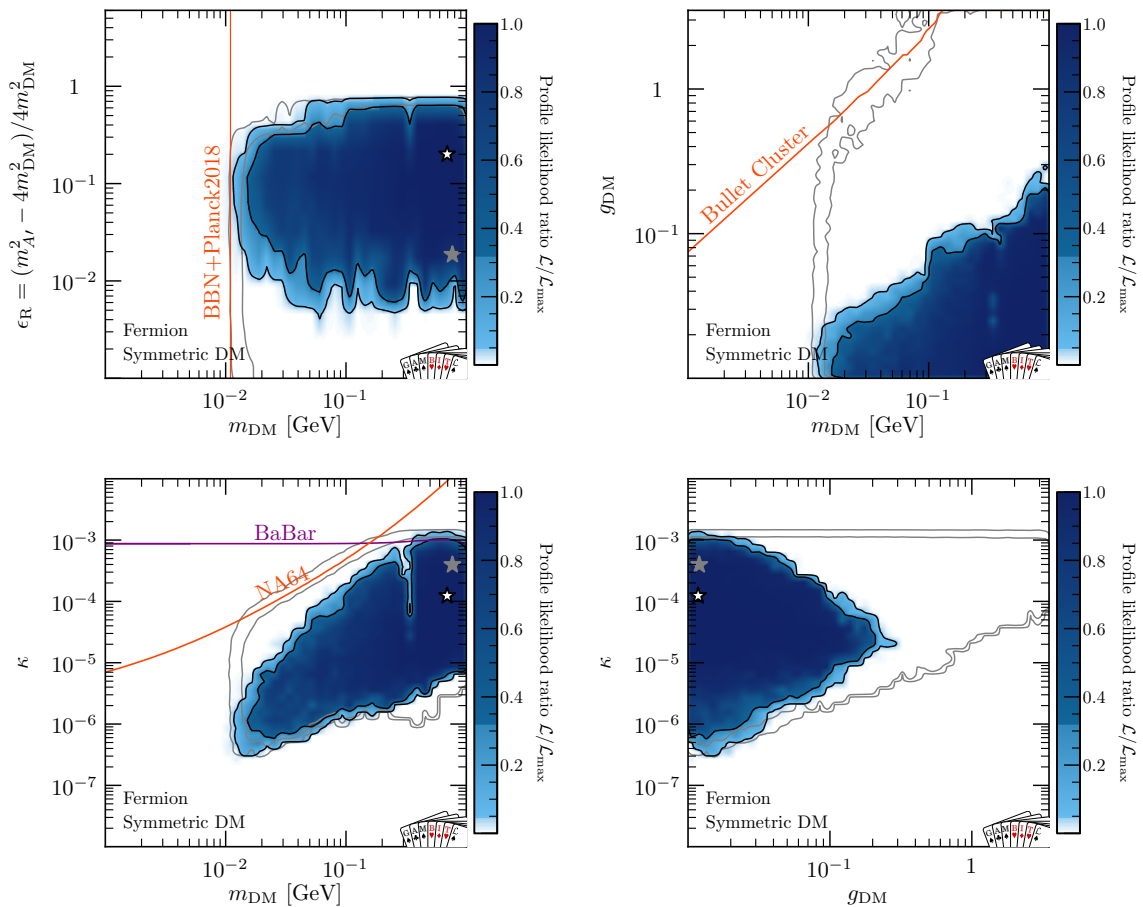


Figure 9. Allowed parameter regions for symmetric fermionic dark matter, when requiring that the observed DM relic abundance is saturated ($\Omega_{\text{DM}}h^2 \approx 0.12$). For comparison, we indicate with gray lines the allowed parameter regions for a sub-dominant DM component and with a gray star the corresponding best-fit point. See caption of figure 7 for details on the various line styles and symbols.

than unity. The only laboratory experiment that places relevant constraints on the parameter space is the BaBar single-photon search.

Next we turn to the question whether the constraints on the parameter space can be relaxed when including a DM asymmetry $\eta_{\text{DM}} > 0$. We expect that a sizeable asymmetry will make it possible to saturate the relic density requirement without violating indirect detection constraints. Hence we expect to find viable parameter space at larger couplings and correspondingly larger cross sections.

We show the allowed parameter regions in figure 10. Note that compared to previous figures we have replaced the panel with g_{DM} versus κ by a panel with m_{DM} versus $\eta_{\text{DM}}m_{\text{DM}}$. As before, grey lines indicate the allowed parameter space when allowing for sub-dominant DM components, while black lines and shaded regions indicate the allowed parameter regions when requiring the relic abundance to be saturated. We see that the difference between the two cases is minimal, indicating that indeed the asymmetry makes it much easier to satisfy the relic density requirement.

Compared to previous figures, we observe two new features. First, the bottom-right

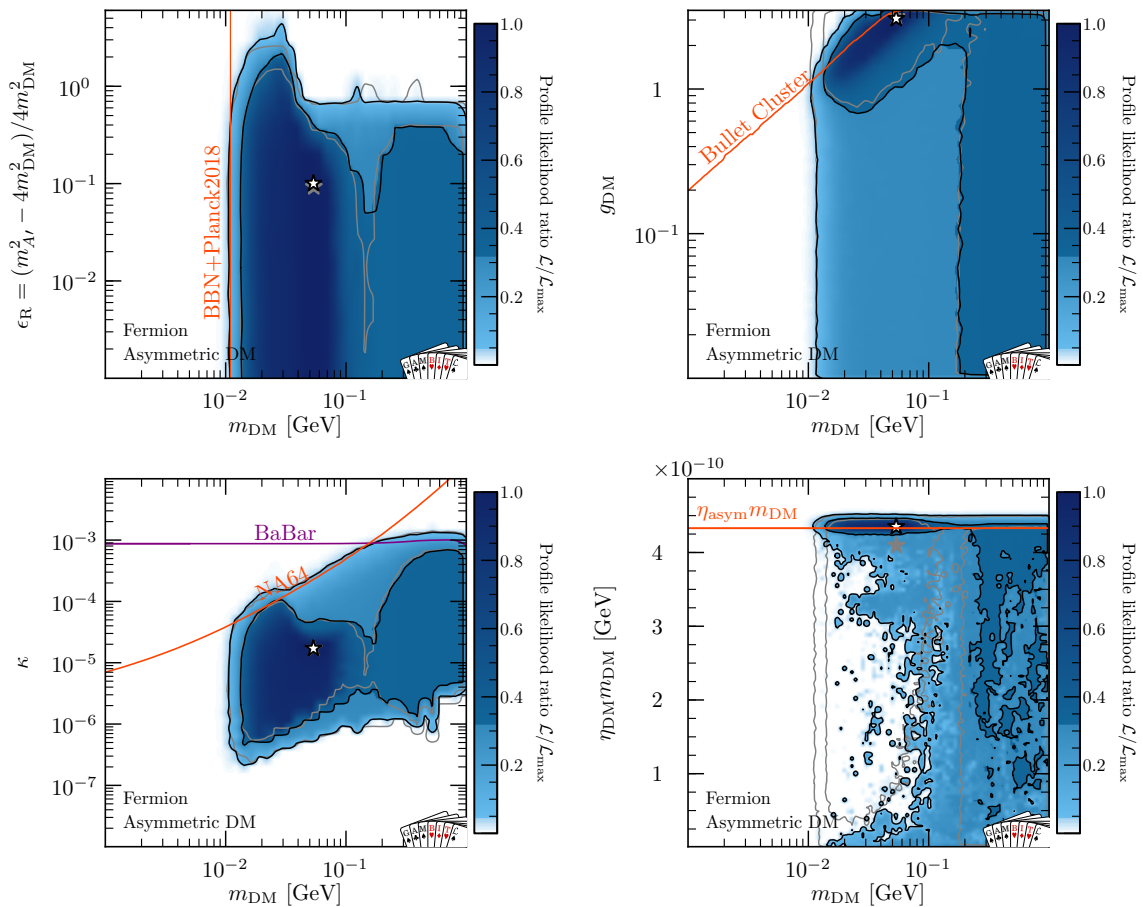


Figure 10. Allowed parameter regions for asymmetric fermionic dark matter with $\Omega_{\text{DM}}h^2 \approx 0.12$. As in figure 9, we indicate with gray lines the allowed parameter regions for a sub-dominant DM component and with a gray star the corresponding best-fit point. The red line in the bottom-right panel indicates the value of $\eta_{\text{DM}}m_{\text{DM}}$ that gives $\Omega_{\text{DM}}h^2 = 0.12$ for the case of a negligible symmetric component, see eq. (3.5).

panel clearly shows a slight preference for $\eta_{\text{DM}}m_{\text{DM}} \approx 4 \cdot 10^{-10}$ GeV, which corresponds to the case where DM is highly asymmetric.

In this case, a relevant constraint on the parameter space stems from the Bullet Cluster bound on DM self-interactions. The Bullet Cluster likelihood that we have implemented prefers a self-interaction cross section around $0.5 \text{ cm}^2/\text{g}$. This preference is the origin of the mild preference for small DM masses and large couplings seen in figure 10. In terms of the log-likelihood of the best-fit point, we find a difference of $-2\Delta \log \mathcal{L} = 2.2$ compared to the symmetric case. We emphasize, however, that this preference at the 1σ level is not significant.

We also show in figure 11 the DM-proton and DM-electron scattering cross sections corresponding to the viable regions of parameter space. In contrast to the case of symmetric DM, we find that now the DM- electron scattering cross section can be large enough for direct detection experiments to place relevant constraints on the model. Indeed, the best-fit point is only slightly below current exclusion limits⁷ and within reach of the next generation

⁷Note that we show published bounds, which are given at 90% confidence level and, in contrast to our

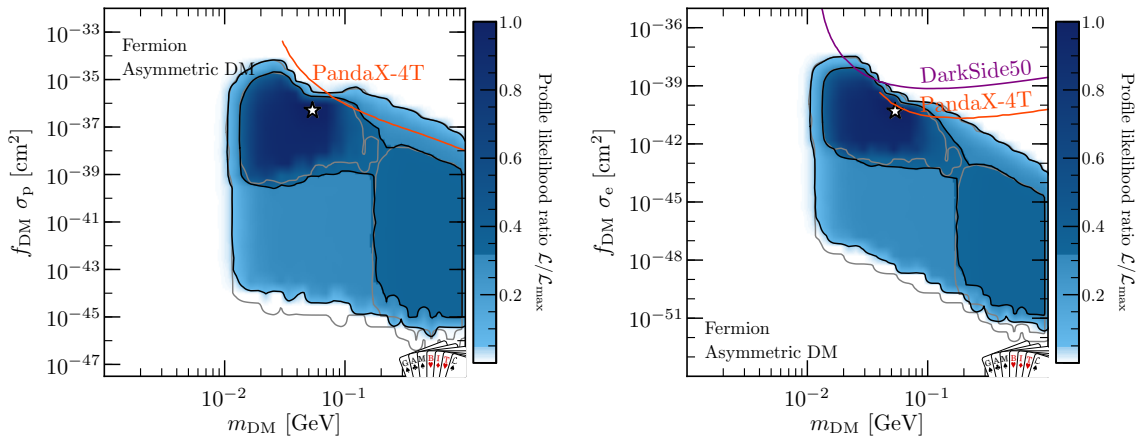


Figure 11. Allowed parameter regions for asymmetric fermionic dark matter with $\Omega_{\text{DM}}h^2 \approx 0.12$ in terms of various observables as a function of the DM mass. See caption of figure 7 for details on the various line styles and symbols.

of experiments.

Bayesian results

As we have seen above, including the asymmetry parameter increases the allowed parameter ranges for the fermionic DM model, but it does not significantly improve the likelihood of the best-fit point. From the frequentist perspective, there is hence no preference for including the additional parameter. Let us now revisit this conclusion in the Bayesian framework, where not only the likelihood of the best-fit point matters, but the volume of the allowed parameter region. In other words, the Bayesian approach penalizes fine-tuning and rewards models that can fit all observations in large fractions of parameter space.

We first consider the case of no asymmetry with the relic density imposed as upper bound. Our results are shown in figure 12, produced using ANESTHETIC [125]. This figure shows in each panel the prior probability in blue and the posterior probability in orange, thus providing a direct visual impression of how the prior belief is updated given the data. Panels above the diagonal show scatter plots of a representative set of the sampled parameter points, panels below the diagonal show the regions of highest probability (dark and light shading corresponding to 68% and 95% probability, respectively). The panels along the diagonal show histograms of the prior and marginalised posterior for each parameter under consideration. Note that the prior for m_{DM} and ϵ_R is not flat due to the requirement $m_{A'} > 2m_{\text{DM}}$ imposed at prior level.

We find good agreement between the Bayesian results and the frequentist results shown in figure 7. In particular, we find that while ϵ_R can be as large as 10^7 at the prior level, the posterior is tightly constrained by the relic density and indirect detection constraints to values below unity. However, while in the frequentist analysis the profile likelihood was found to be approximately constant for $\epsilon_R < 0.4$, we find that the posterior probability rapidly decreases for $\epsilon_R < 0.1$ due to the required fine-tuning between $m_{A'}$ and m_{DM} , leading to a posterior that is strongly peaked around 10^{-1} . Similarly, the marginalised posteriors for the other model parameters exhibit some clear preferences, which are not visible in the profile

treatment, do not include uncertainties in the local DM density and velocity distribution.

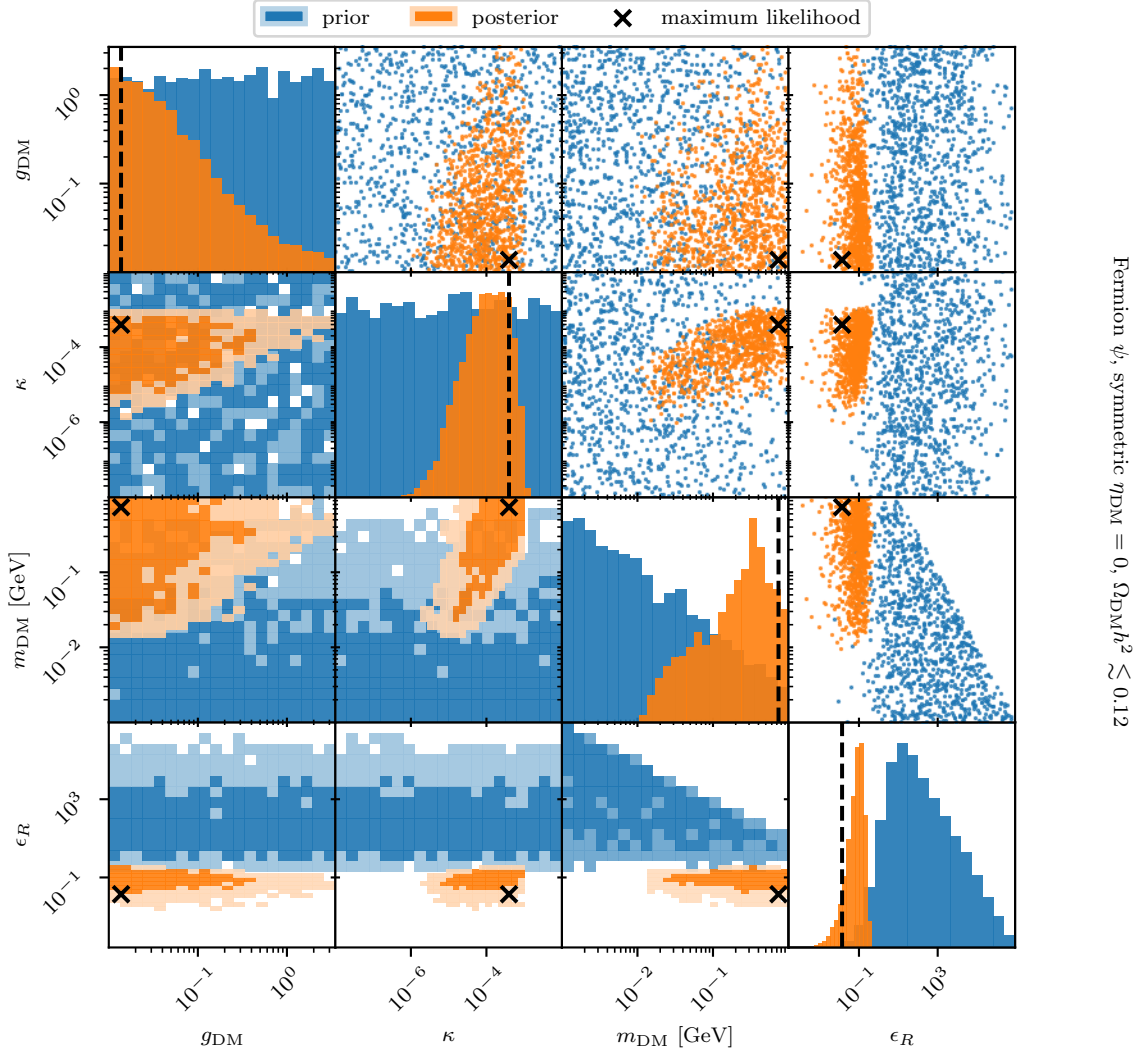


Figure 12. Prior (blue) and posterior (orange) probabilities for the symmetric fermionic DM model with $\Omega_{\text{DM}}h^2 \leq 0.12$. Panels above the diagonal show scatter plots of a representative set of the sampled parameter points, panels below the diagonal show the regions of highest probability (dark and light shading corresponding to 68% and 95% probability, respectively). The panels along the diagonal show histograms of the prior and marginalised posterior for each parameter under consideration. The maximum likelihood point is indicated by a cross in the 2-dimensional plots and by a vertical dashed line in the 1-dimensional histograms.

likelihoods obtained in the frequentist scans. Specifically, there is a clear preference for small values of g_{DM} and large values of m_{DM} . As for ϵ_R these preferences are a result of the volume effect, i.e. the fine-tuning penalty inherent in the Bayesian approach, rather than a result of a preference in the likelihood.

These effects become even more pronounced when requiring the DM particle to constitute all of DM, see figure 13. For small DM masses, significant tuning in both κ and g_{DM}

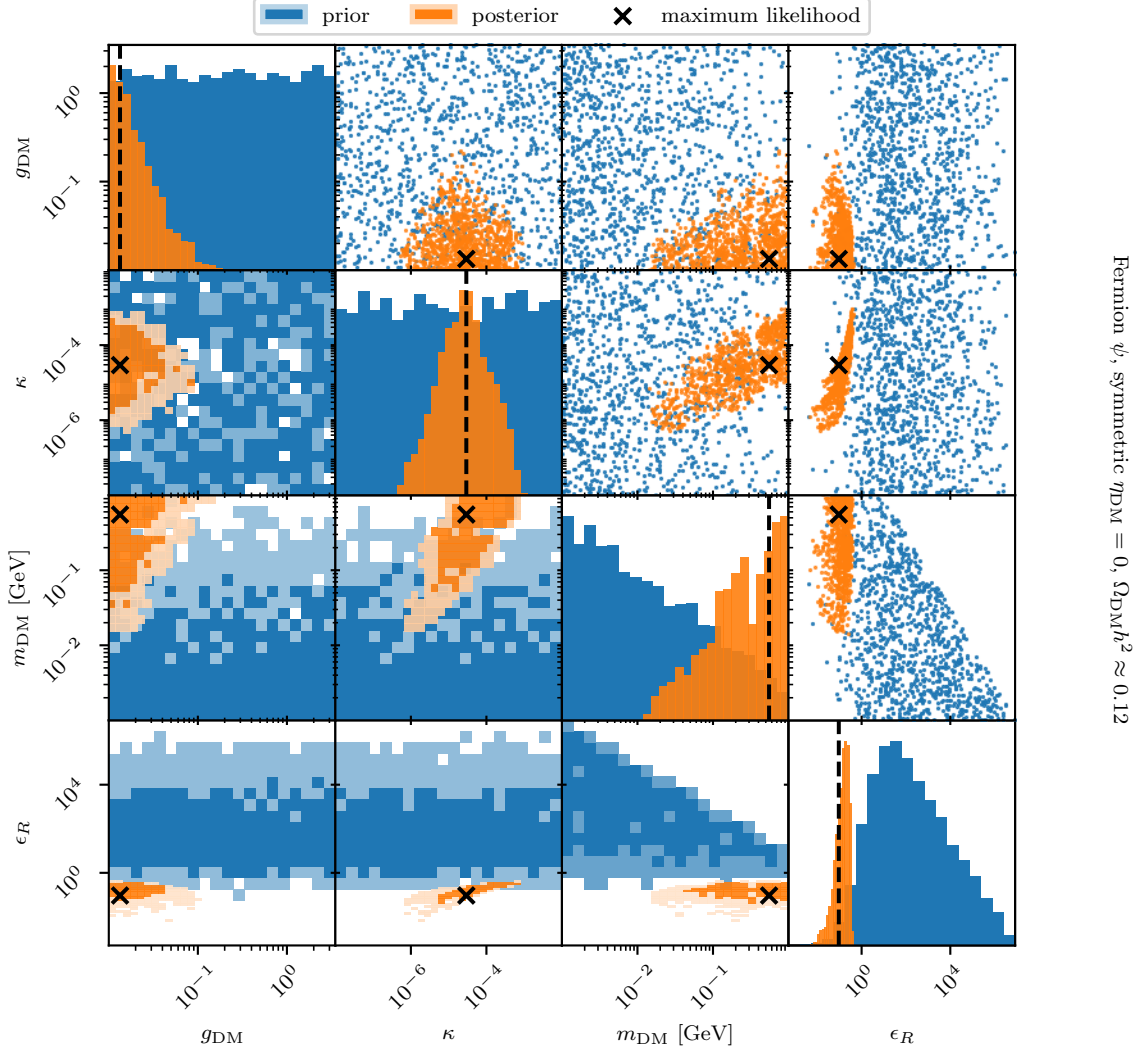


Figure 13. Same as figure 12, but for the symmetric fermionic DM model with $\Omega_{\text{DM}}h^2 \approx 0.12$.

is required in order to satisfy all constraints. As a result, the posterior probability for the DM mass peaks strongly at the largest values considered in the scan, while the posterior probability of g_{DM} peaks strongly at the smallest values. The posterior for κ is less tightly constrained, with a broad peak in the range 10^{-5} – 10^{-4} .

Finally, when we include the asymmetry parameter, we obtain the results shown in figure 14. We see that there is a strong preference for $\eta_{\text{DM}}m_{\text{DM}}$ to be close to $4 \cdot 10^{-10}$ GeV, which corresponds to the case where DM is highly asymmetric. More precisely, the (equal-tailed) credible interval for $\eta_{\text{DM}}m_{\text{DM}}$ is $[4.28, 4.35] \cdot 10^{-10}$ GeV at 68% confidence level (or $[3.78, 4.41] \cdot 10^{-10}$ GeV at 95% confidence level). For comparison, when we allow for a sub-dominant DM component, the credible intervals broaden significantly to $[0.12, 4.30] \cdot 10^{-10}$ GeV at 95% confidence level. Including the asymmetry significantly relaxes the constraints on the other

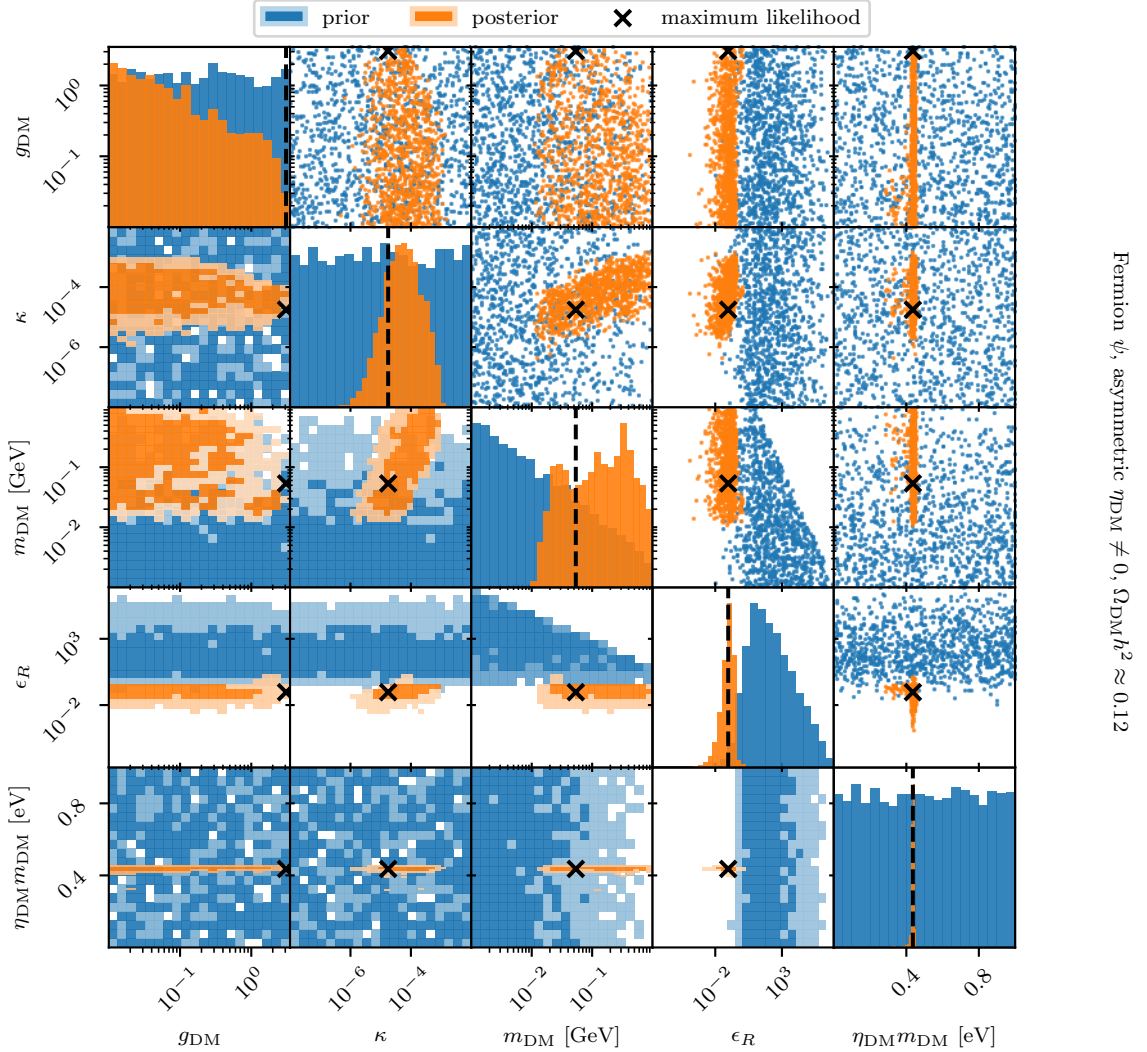


Figure 14. Same as figure 12, but for the *asymmetric* fermionic DM model with $\Omega_{\text{DM}} h^2 \approx 0.12$.

model parameters, leading to much broader posteriors for m_{DM} and g_{DM} , which can now go up to the perturbativity bound.

As in the frequentist case, the best fit point lies at small DM masses and large coupling, corresponding to a self-interaction cross section around $0.5 \text{ cm}^2/\text{g}$. However, the best-fit value of g_{DM} does not coincide with the maximum of the marginalised posterior, which lies at much smaller values. In other words, the Bayesian analysis prefers the large parameter region with negligible self-interaction cross section over the small parameter region with sizeable self-interaction cross section, even though the latter has a slightly higher likelihood.

Given that including an asymmetry substantially relaxes the constraints on the other model parameters, it is interesting to perform a Bayesian model comparison between the models with and without asymmetry parameter. For this purpose, we can calculate the

Bayesian evidence

$$\mathcal{Z} = \int \mathcal{L}(\theta)\pi(\theta)d\theta, \quad (4.1)$$

where θ denotes the model parameters, $\mathcal{L}(\theta)$ the likelihood function and $\pi(\theta)$ the prior probabilities. It is furthermore possible [36, 126] to decompose the Bayesian evidence into the posterior-weighted log-likelihood

$$\langle \log \mathcal{L} \rangle_{\mathcal{P}} = \int \mathcal{P}(\theta) \log \mathcal{L}(\theta) d\theta \quad (4.2)$$

and the Kullback-Leibler divergence of prior and posterior probability

$$\mathcal{D}_{\text{KL}} = \int \mathcal{P}(\theta) \log \frac{\mathcal{P}(\theta)}{\pi(\theta)} d\theta, \quad (4.3)$$

in the sense that

$$\log \mathcal{Z} = \langle \log \mathcal{L} \rangle_{\mathcal{P}} - \mathcal{D}_{\text{KL}}. \quad (4.4)$$

The first term becomes large if the model can fit all available data in the most probable regions of parameter space and small if the entire parameter space is in tension with data. The second term is large if the available data can only be fitted in very special regions of parameter space, and small if the model predictions are generically in agreement with data. This decomposition makes it possible to attribute the preference between two models either to the likelihood (i.e. a genuine preference in the data) or to the volume effect (i.e. a fine-tuning penalty for parameters that need to lie in very narrow regions of parameter space in order for the model to agree with data). For the model without asymmetry we find

$$\log \mathcal{Z}_{\text{sym}} = -376.93 \pm 0.12 = -358.59 - 18.34 \quad (4.5)$$

whereas the model with asymmetry gives

$$\log \mathcal{Z}_{\text{asym}} = -374.18 \pm 0.11 = -358.69 - 15.49. \quad (4.6)$$

As expected, there is no preference between the two models in the likelihood term, but the fine-tuning penalty is much smaller in the second model than in the first one, leading to an overall Bayes factor of

$$\frac{\mathcal{Z}_{\text{asym}}}{\mathcal{Z}_{\text{sym}}} = 15.6, \quad (4.7)$$

which constitutes a “strong” preference according to the Jeffreys’ scale.

We emphasize, however, that the fine-tuning penalty is strongly determined by the chosen priors for the model parameters. If for example we were to use a logarithmic prior for η_{DM} in the range $[10^{-13}, 10^{-6}]$ instead of the linear prior on $\eta_{\text{DM}}m_{\text{DM}}$, the Bayes factor between the two models decreases from 15.6 to 2.9, which corresponds to a model preference that is “barely worth mentioning”.

4.2 Scalar dark matter

For the case of scalar DM, indirect detection constraints play a negligible role, because the annihilation cross section is p -wave suppressed for small velocities. As a result, it is much easier to saturate the observed DM relic abundance even without introducing an asymmetry parameter. We therefore restrict ourselves to the case of symmetric DM.

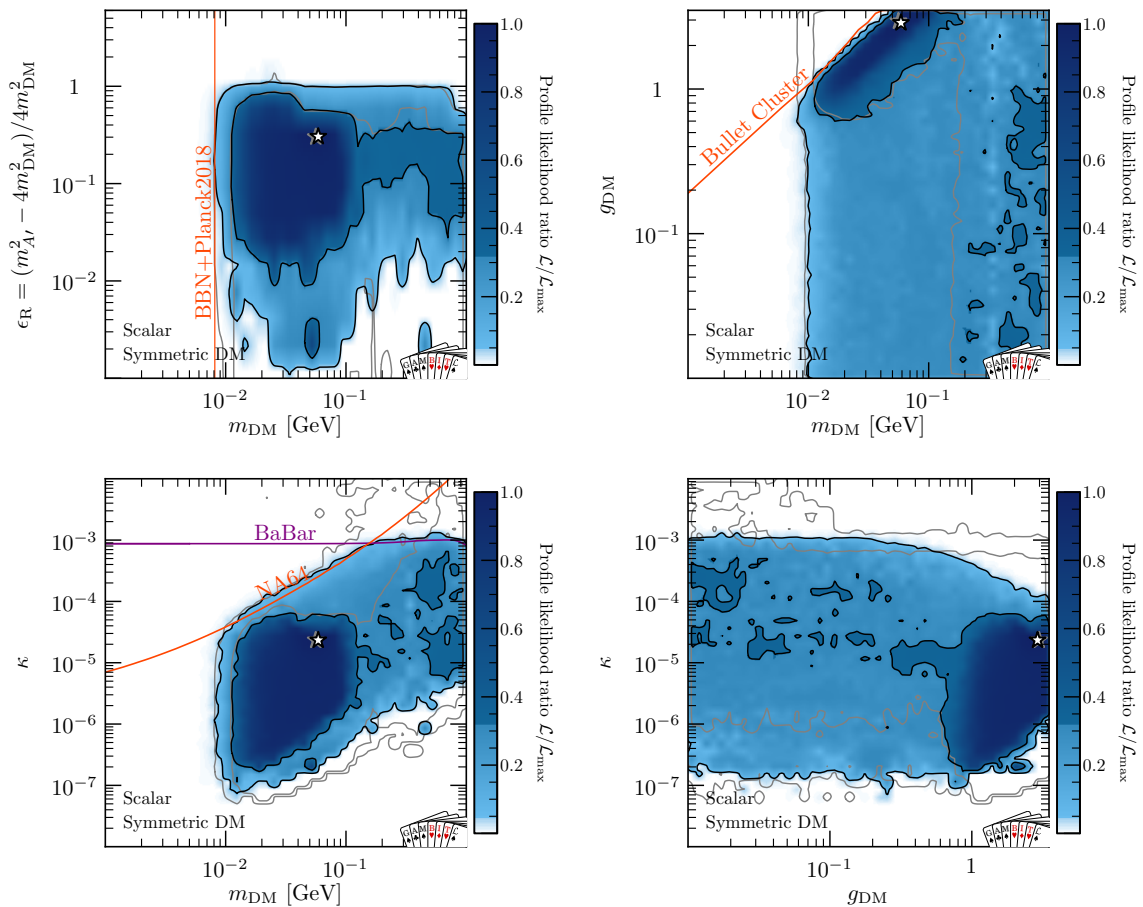


Figure 15. Allowed parameter regions for symmetric scalar dark matter with $\Omega_{DM}h^2 \approx 0.12$. Gray lines indicate the allowed parameter regions for a sub-dominant DM component and the gray star indicates the corresponding best-fit point. See caption of figure 7 for details on the various line styles and symbols.

The results from our frequentist scan are shown in figure 15. The allowed parameter regions look very similar to the case of highly asymmetric fermionic dark matter. This finding is expected, since in both cases indirect detection constraints are absent and the phenomenology is otherwise very similar. We also observe that the allowed parameter regions change only very slightly when considering a sub-dominant DM component (gray lines). The only notable differences are that for a DM sub-component the Bullet Cluster constraint can be evaded, which opens up additional parameter space at large g_{DM} and small m_{DM} , and that the BaBar bound can be evaded by having simultaneously $g_{DM} \approx 10^{-2}$ and $\kappa > 10^{-3}$, such that $\text{BR}_{A' \rightarrow \chi\bar{\chi}} \ll 1$. The latter possibility would however likely be constrained by additional likelihoods not implemented in the present work, such as searches for dark photons decaying into muon pairs at LHCb [127].

The corresponding Bayesian results are shown in figure 16. We find that the posterior probabilities for m_{DM} and g_{DM} now follow the prior probabilities much more closely (apart from the lower bound $m_{DM} \gtrsim 10$ MeV imposed by cosmological constraints). Nevertheless, the relic density requirement still imposes a clear upper bound on ϵ_R and a lower bound on

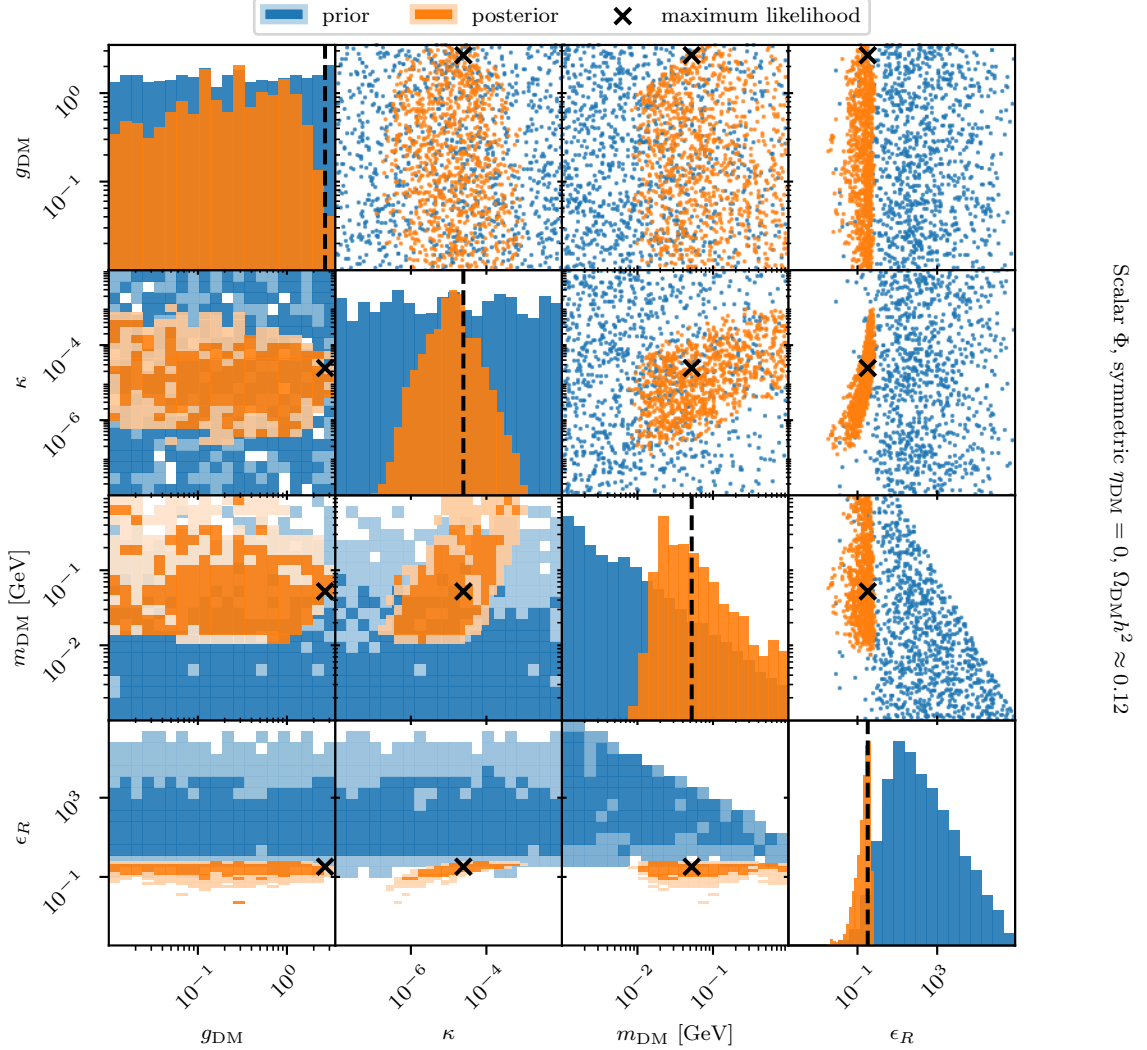


Figure 16. Prior (blue) and posterior (orange) probabilities for the symmetric scalar DM model with $\Omega_{\text{DM}} h^2 \approx 0.12$.

κ , while collider and beam-dump experiments rule out large values of κ .

As expected, we find that including the asymmetry parameter does not change the picture substantially. There is no strong preference for a large asymmetry, and the posteriors of the other model parameters are not significantly modified. The Bayesian evidences are found to be

$$\log \mathcal{Z}_{\text{sym}} = -374.16 \pm 0.11 = -358.46 - 15.70 \quad (4.8)$$

and

$$\log \mathcal{Z}_{\text{asym}} = -373.77 \pm 0.11 = -358.60 - 15.18, \quad (4.9)$$

which are very similar to each other and to the fermionic DM model with asymmetry, such that none of these models are preferred in a Bayesian sense. We illustrate the various Bayesian

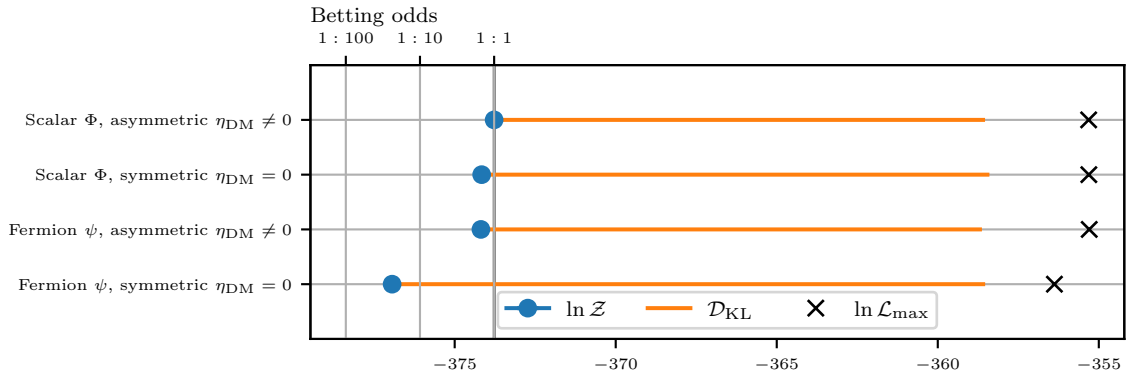


Figure 17. Bayes factors for the various models considered in this work. The blue dots indicate the logarithm of the Bayesian evidence, which can be translated into betting odds relative to the most favoured model (see vertical lines and labels at the top). The orange bars show the Kullback-Leibler divergence of prior and posterior for each model, with longer bars indicating a larger fine-tuning penalty. This penalty is largest for the symmetric fermionic DM model, accounting for the smaller Bayesian evidence, whereas the log-likelihoods of the respective best-fit points (indicated by the black crosses) are similar for all models.

evidences in figure 17.

5 Discussion

In this section we discuss the implications of our results for the experimental search programme for sub-GeV DM.

5.1 Sensitivity projections

In figure 18 we compare the allowed parameter regions of the two preferred models, namely asymmetric fermionic DM and symmetric scalar DM, with the projected sensitivities of near-future experiments. For accelerator experiments we consider the single-photon search of Belle II with 20 fb^{-1} [128] and the missing energy search of LDMX with 10^{16} electrons from an 8 GeV beam [129]. For DM-nucleus scattering we consider SuperCDMS [130], and the recently proposed DELight experiment [131], which plans to use superfluid helium to reach lower DM masses. For DM-electron scattering we show the projections from DAMIC and SENSEI (both taken from ref. [114]).

We find that near-future experiments can probe significant parts of the allowed parameter spaces, but will not be able to explore the two models comprehensively. The reason is in particular that the relic density requirement can be satisfied for rather small values of g_{DM} and κ , given sufficient resonant enhancement (i.e. sufficiently small values of ϵ_R).

The corresponding plots in the Bayesian framework is shown in appendix D. As discussed above, in the Bayesian treatment very small values of ϵ_R are disfavoured due to the required fine-tuning between m_{DM} and $m_{A'}$. This leads to a general preference for larger couplings and cross sections than in the frequentist analysis. Out of the experiments that we consider, we find that LDMX has the greatest chance of discovery, probing 64% of the posterior volume.

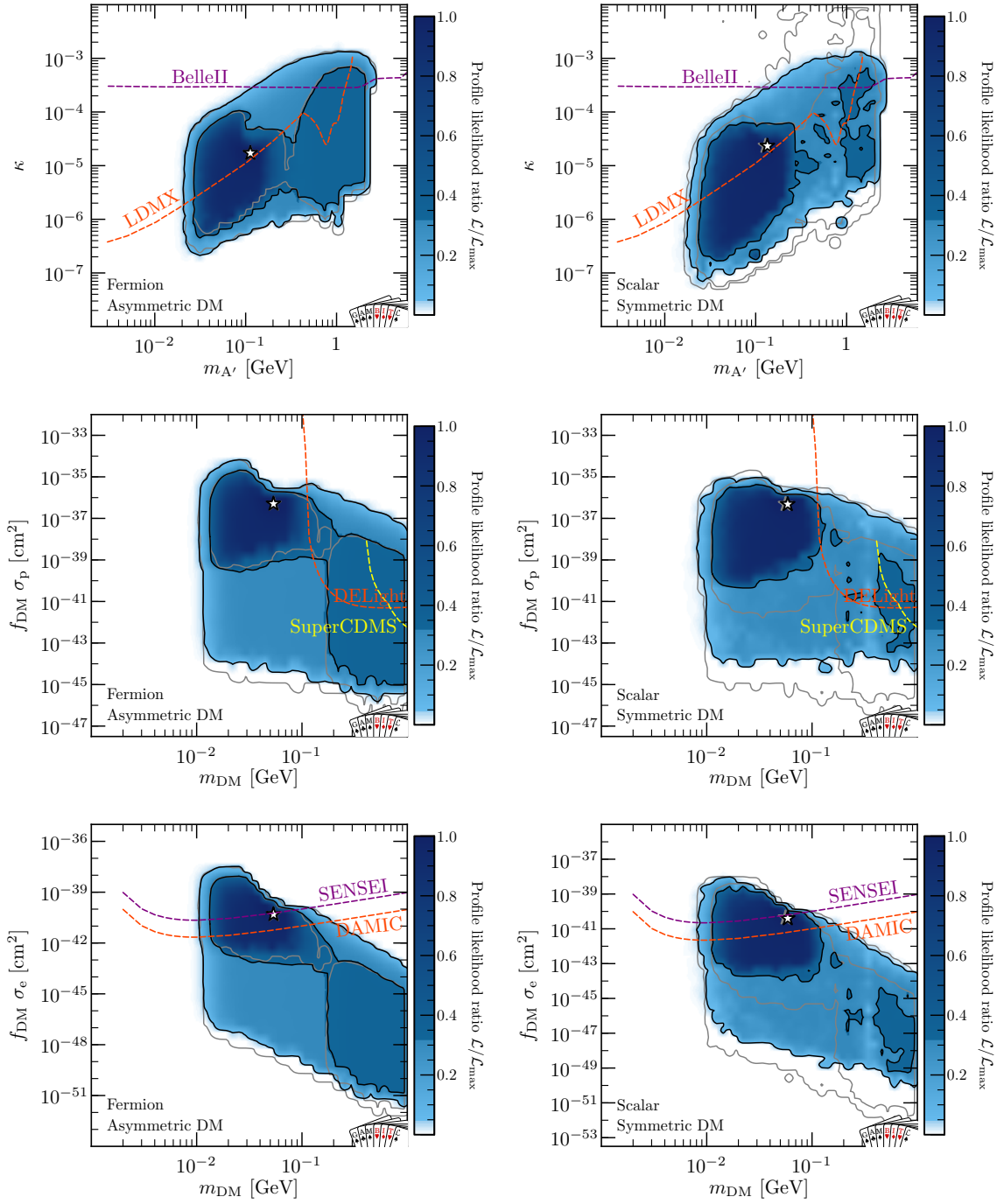


Figure 18. Allowed parameter regions of the asymmetric fermionic DM model (left column) and the symmetric scalar DM model (right column) in terms of the quantities that are most directly relevant for observations: kinetic mixing versus dark photon mass (top row), effective DM-nucleon scattering cross section versus DM mass (middle row) and effective DM-electron scattering cross section versus DM mass (bottom row). In each panel we show the projected sensitivities for various near-future experiments.

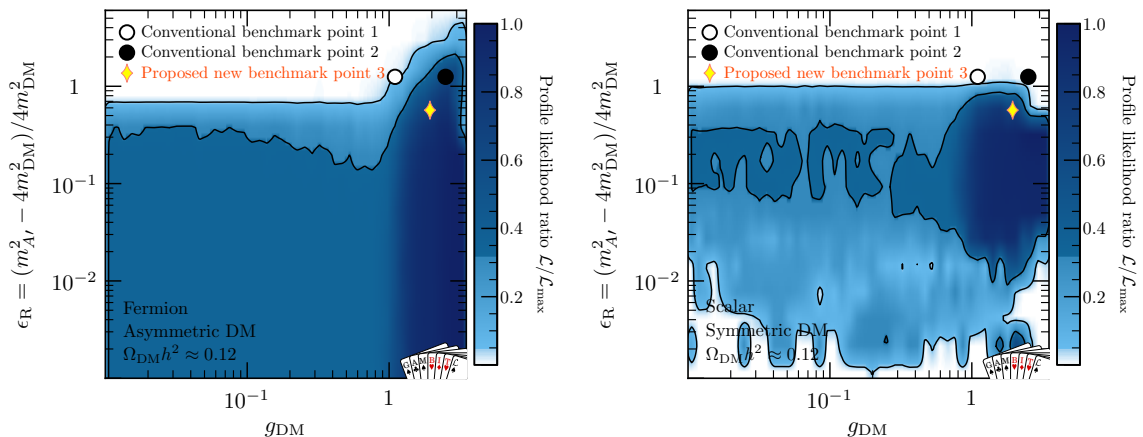


Figure 19. Allowed parameter space for the asymmetric fermion DM model (left) and the symmetric scalar DM model (right) in the $\epsilon_R - g_{\text{DM}}$ parameter plane. The conventional benchmark points with $m_{A'}/m_{\text{DM}} = 3$ and either $\alpha_D = 0.1$ (BP1) or $\alpha_D = 0.5$ (BP2) are indicated by a white and a black dot, respectively. Our proposed benchmark point with $m_{A'}/m_{\text{DM}} = 2.5$ and $\alpha_D = 0.3$ (BP3) is indicated by a yellow diamond.

5.2 A new benchmark scenario

Models of sub-GeV DM coupled to dark photons are often studied under simplifying assumptions in the literature [20–23]. In particular, it has become conventional to fix the ratio of dark photon and DM mass to 3, corresponding to $\epsilon_R = 5/4$. Furthermore, $\alpha_D = g_{\text{DM}}^2/(4\pi)$ is often fixed to either 0.1 or 0.5, corresponding to $g_{\text{DM}} = 1.1$ and $g_{\text{DM}} = 2.5$, respectively.

In figure 19, we show these benchmark choices (called BP1 and BP2) in the g_{DM} versus ϵ_R parameter plane together with the allowed parameter regions that we have identified for asymmetric fermionic DM (left) and scalar DM (right) in our scans. We find that in both models BP1 lies outside of the allowed parameter region at 95% C.L., while BP2 lies barely within the 68% C.L. for asymmetric fermionic DM and outside of the 95% C.L. region for symmetric scalar DM. We therefore propose a new benchmark point (BP3), which is given by

$$\begin{aligned}
 m_{A'} = \frac{5}{2}m_{\text{DM}} \quad \text{or} \quad \epsilon_R = \frac{9}{16} \\
 \alpha_{\text{DM}} = 0.3 \quad \text{or} \quad g_{\text{DM}} = 1.94.
 \end{aligned}
 \tag{5.1}$$

We emphasize that this benchmark point does not suffer from the uncertainties in relic density calculations illustrated in figure 2, both because ϵ_R is not small and because g_{DM} (and hence the invisible decay width) is larger than what is used there.

Once these parameters have been fixed, the allowed ranges of the remaining parameters shrink substantially. In fact, for the case of scalar DM, the relic density requirement implies a very tight relation between κ and m_{DM} , such that effectively all observables are uniquely predicted as a function of the DM mass (see for example ref. [41]). The case of asymmetric fermionic DM is more interesting, since the relic density requirement only imposes a lower bound on κ (corresponding to the case where $\eta_{\text{DM}} = 0$), whereas larger values of κ can still be viable for $\eta_{\text{DM}} > 0$.

We show the allowed parameter regions for asymmetric fermionic DM with ϵ_R and g_{DM} fixed to BP3 in figure 20. To facilitate the comparison with other results in the literature,

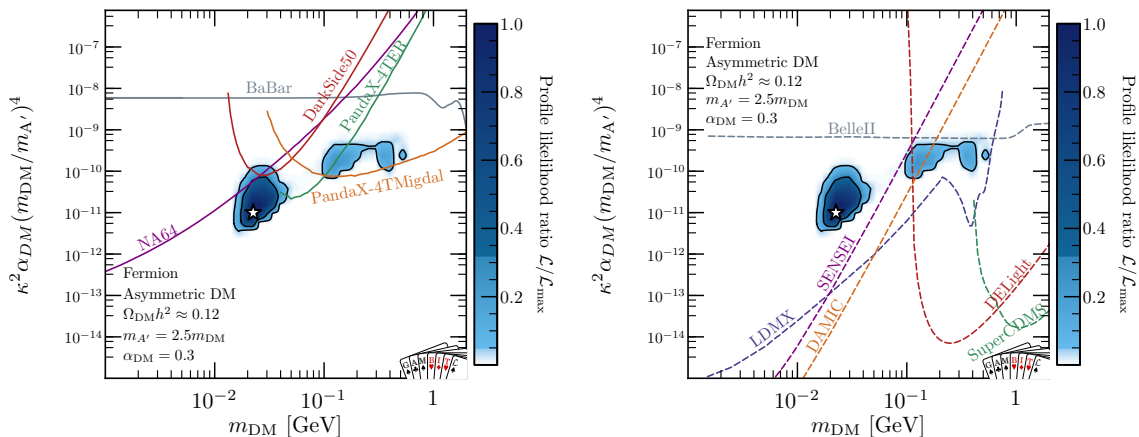


Figure 20. Allowed parameter regions for asymmetric fermionic DM with fixed $\epsilon_R = 0.5625$ and $g_{\text{DM}} = 1.94$ (BP3). In the left panel we show the various constraints implemented in this work, whereas the right panel shows projected sensitivities.

we show on the y-axis the effective coupling

$$y = \kappa^2 \alpha_D \frac{m_{\text{DM}}^4}{m_{A'}^4} = 0.00768 \kappa^2, \quad (5.2)$$

where the second equality holds specifically for BP3. Since we have fixed ϵ_R and g_{DM} , it is possible to superimpose exclusion limits from both accelerator and direct detection experiments in the same parameter plane. Indirect detection constraints, on the other hand, depend in a non-trivial way on the asymmetry parameter and do therefore not appear in this parameter plane. In the right panel of figure 20, we show the corresponding sensitivity projections, which cover the entire allowed parameter space.

6 Conclusions

In this work we have explored several different models of sub-GeV DM coupled to a dark photon with kinetic mixing. These models face much weaker constraints from bounds on the DM scattering cross section from direct detection experiments than traditional WIMPs, but are potentially in tension with bounds on the DM annihilation cross section from indirect detection experiments and cosmological data. The central focus of our study has therefore been to understand how these bounds can be evaded and to explore the implications for laboratory experiments, thus providing a general status update for this much-discussed model class.

For fermionic DM, where annihilation proceeds via s -wave, the simplest possibility to satisfy all experimental constraints is to consider resonant freeze-out, which requires a tight relation between the DM mass and the dark photon mass: $2 < m_{A'}/m_{\text{DM}} \lesssim 2.5$. An attractive alternative is to allow for a particle-antiparticle asymmetry η_{DM} , which increases the relic abundance relative to the symmetric case, for a given annihilation rate, but suppresses indirect detection signals. For scalar DM, on the other hand, annihilation proceeds via p -wave and is therefore velocity-suppressed in the present universe and effectively unconstrained.

To study these possibilities in detail, we have implemented state-of-the-art likelihoods for all relevant observables and measurements. Many of these are calculated using external codes, which we have interfaced using the GAMBIT global fitting framework. In particular, we calculate the DM relic density using DARKSUSY, direct detection constraints using DD-CALC and OBSCURA, dark photon branching ratios using DARKCAST, BBN constraints using ALTERBBN and CMB energy injection constraints using HAZMA and DARKAGES. Furthermore, we have performed several calculations not previously available in the literature, in particular regarding DM production in beam-dump experiments using a version of BDNMC extended for this analysis and DM self-interactions in the Bullet Cluster. Finally, we reinterpret interpolated likelihoods from the literature to constrain dark photon production at accelerators as well as X-rays from DM annihilations.

For the case of symmetric fermionic DM we have found large viable parameter regions close to resonance when allowing for the DM particle to constitute only a fraction of the observed DM abundance, see figure 7. When we instead require the DM particles to saturate the observed DM abundance, the dark sector couplings are tightly constrained by astrophysical and cosmological observations, such that laboratory experiments are not currently sensitive to the allowed parameter regions, see figure 9.

This conclusion changes when including an asymmetry parameter, which makes it possible to saturate the DM relic abundance for larger dark sector couplings without violating astrophysical bounds. As shown in figure 10, this opens up additional parameter regions that are constrained primarily by laboratory experiments (as well as by the DM self-interaction constraint from the Bullet Cluster). We emphasize, however, that the likelihood of the best-fit point does not change significantly when including the asymmetry parameter, such that in the frequentist analysis there is no preference for the asymmetric model over the symmetric one.

We have also performed a Bayesian interpretation of our results, finding general agreement with the frequentist analysis. However, the Bayesian analysis penalises parameter regions that require a finely tuned mass ratio of $m_{A'}/m_{\text{DM}} \approx 2$. In the case of fermionic DM, this fine-tuning penalty leads to a clear preference for a non-zero asymmetry, see figure 14. To quantify this preference, we have calculated the Bayesian evidence for both symmetric and asymmetric fermionic DM, finding a Bayes factor (i.e. an evidence ratio) of around 15 in favour of the asymmetry.

For the case of scalar DM, on the other hand, we have found no preference for introducing an asymmetry. Indeed, the phenomenology and the allowed parameter regions for symmetric scalar DM are very similar to the ones for asymmetric fermionic DM, see figure 15. Correspondingly the Bayes factor between these two models is very close to unity.

Recognizing the vibrant experimental activity to explore the sub-GeV scale, we have also studied the discovery prospects for the next generation of laboratory experiments. We found that these will be able to explore large parts of allowed parameter space, even though they cannot probe the preferred models comprehensively, see figure 18. Since the commonly adopted benchmark points are already disfavoured, we have also proposed a new benchmark scenario, defined as $m_{A'}/m_{\text{DM}} = 2.5$ and $\alpha_{\text{DM}} = 0.3$, which can serve as an appealing target for upcoming searches. Indeed, we expect that this benchmark can be fully probed within the next decade, highlighting the tantalizing possibility for a discovery in the near future.

Acknowledgments

We thank Jordan Koechler for providing the interpolated likelihoods from ref. [15], and Pieter Braat, Jan Conrad, Adam Coogan, Lukas Hergt, Patrick deNiverville, Ruth Pottgen and all members of the GAMBIT community for discussions. SB acknowledges the support by the Doctoral School 'Karlsruhe School of Elementary and Astroparticle Physics: Science and Technology'. The research of CB is supported by Australian Research Council grants DP210101636, DP220100643 and LE210100015. CC was supported by the Arthur B. McDonald Canadian Astroparticle Physics Research Institute. Research at the Perimeter Institute is supported by the Government of Canada through the Department of Innovation, Science, and Economic Development, and by the Province of Ontario. RC acknowledges support from an individual research grant from the Swedish Research Council (Dnr. 2018-05029). RC, TE, and TG research was partly financed via the Knut and Alice Wallenberg project "Light Dark Matter" (Dnr. KAW 2019.0080). TE was also supported by the Knut and Alice Wallenberg Foundation (PI, Jan Conrad). TE thanks the Theoretical Subatomic Physics group at Chalmers University of Technology for its hospitality. TEG and FK acknowledge funding by the Deutsche Forschungsgemeinschaft (DFG) through the Emmy Noether Grant No. KA 4662/1-2 and Grant No. 396021762 – TRR 257. This work was performed using the Cambridge Service for Data Driven Discovery (CSD3), part of which is operated by the University of Cambridge Research Computing on behalf of the STFC DiRAC HPC Facility (www.dirac.ac.uk). The DiRAC component of CSD3 was funded by BEIS capital funding via STFC capital grants ST/P002307/1 and ST/R002452/1 and STFC operations grant ST/R00689X/1. DiRAC is part of the National e-Infrastructure. The plots were made using pippi v2.1 [132] and anesthetic [125].

A Relic density calculations

In this appendix we document the implementation of asymmetric DM relic density calculations in DARKSUSY, which has been made available with release v6.4 of the code (another update in that release, also developed in the context of this work, is the inclusion of interpolated HAZMA yield tables from ref. [59], cf. section 3.1.3). We further discuss the limitations of the common Boltzmann approach that the current DARKSUSY implementation rests on.

Neglecting oscillations and CP violations, the Boltzmann equation for the number densities of non-relativistic DM (χ) and anti-DM ($\bar{\chi}$) particles are given by

$$\dot{n}_\chi + 3Hn_\chi = \dot{n}_{\bar{\chi}} + 3Hn_{\bar{\chi}} = -\langle\sigma v\rangle (n_\chi n_{\bar{\chi}} - n_{\text{eq}}^2), \quad (\text{A.1})$$

where $\langle\sigma v\rangle$ is the total thermally averaged annihilation rate and n_{eq} is the number density in equilibrium. Introducing $Y \equiv n_{\bar{\chi}}/s$ and $x \equiv m_{\text{DM}}/T$, and assuming entropy conservation, this can be re-written in full analogy to the case with $\eta_{\text{DM}} = 0$ (see for example refs. [51, 52] for details) as

$$\frac{dY}{dx} = -\lambda (Y^2 + Y\eta_{\text{DM}} - Y_{\text{eq}}^2), \quad (\text{A.2})$$

with

$$\lambda \equiv \sqrt{\frac{\pi}{45G}} \frac{g_*^{1/2} m_{\text{DM}}}{x^2} \langle\sigma v\rangle. \quad (\text{A.3})$$

Here, $G = M_{\text{Pl}}^{-2}$ is Newton's gravitational constant, and g_* is defined in terms of the effective number of energy (g_{eff}) and entropy (h_{eff}) degrees of freedom as

$$g_*^{1/2} \equiv \frac{h_{\text{eff}}}{\sqrt{g_{\text{eff}}}} \left(1 + \frac{1}{3} \frac{T}{h_{\text{eff}}} \frac{dh_{\text{eff}}}{dT} \right). \quad (\text{A.4})$$

A.1 Asymmetric dark matter with DarkSUSY

We numerically solve eq. (A.2) by means of an implicit trapezoidal method with adaptive stepsize h : when going from x_i to $x_{i+1} = x_i + h$, we estimate $Y_{i+1} \equiv Y(x_{i+1})$ as

$$Y_{i+1} = Y_i + \frac{h}{2} (Y'_i + Y'_{i+1}) = \frac{\tilde{C}_i}{2} - \frac{1}{2} \tilde{\lambda}_{i+1} Y_{i+1}^2 - \frac{1}{2} \tilde{\eta}_{i+1} Y_{i+1}, \quad (\text{A.5})$$

where $\tilde{\lambda}_i \equiv h\lambda(x_i)$, $\tilde{\eta}_i \equiv \eta\tilde{\lambda}_i$ and $\tilde{C}_i \equiv 2Y_i(1 - \frac{\tilde{\eta}_i}{2}) - \tilde{\lambda}_i (Y_i^2 - Y_{\text{eq},i}^2) + \tilde{\lambda}_{i+1} Y_{\text{eq},i+1}^2$. This constitutes a quadratic equation for Y_{i+1} with solution

$$Y_{i+1} = \frac{\tilde{C}_i / [1 + \tilde{\eta}_{i+1}/2]}{1 + \sqrt{1 + \tilde{\lambda}_{i+1} \tilde{C}_i / [1 + \tilde{\eta}_{i+1}/2]^2}}. \quad (\text{A.6})$$

In order to estimate the local relative error we also calculate the abundance at x_{i+1} with a modified Euler method. We denote this alternative estimate for Y_{i+1} with a lower-case y_{i+1} :

$$y_{i+1} \equiv Y_i + hY'_{i+1} = Y_i + \tilde{\lambda}_{i+1} Y_{\text{eq},i+1}^2 - \tilde{\lambda}_{i+1} y_{i+1}^2 - \tilde{\eta}_{i+1} y_{i+1}, \quad (\text{A.7})$$

which we solve for

$$y_{i+1} = \frac{\tilde{c}_i / (2[1 + \tilde{\eta}_{i+1}])}{1 + \sqrt{1 + \tilde{\lambda}_{i+1} \tilde{c}_i / [1 + \tilde{\eta}_{i+1}]^2}}, \quad (\text{A.8})$$

with $\tilde{c}_i \equiv 4Y_i + 4\tilde{\lambda}_{i+1} Y_{\text{eq},i+1}^2$. When solving the Boltzmann equation (A.2), as implemented in eq. (A.6), we adaptively decrease the step size h if $(Y_{i+1} - y_{i+1})/Y_{i+1}$ exceeds a given tolerance (contained in the common block variable `compeps`; the initial step size for h is stored in the common block variable `hstep`).

A new routine `dsrdomega_adm` returns the total DM density $\Omega_{\text{DM}} h^2$ thus calculated – in full analogy to the corresponding routine `dsrdomega` for the symmetric case (but taking an additional input parameter η_{DM}). It also returns the fraction of symmetric DM that contributes to the relic density,

$$r \equiv \frac{2\Omega_{\tilde{\chi}} h^2}{\Omega_{\text{DM}} h^2} = \frac{f_{\text{sym}}}{f_{\text{DM}}}. \quad (\text{A.9})$$

A.2 Limitations of the standard Boltzmann approach

One of the main assumptions leading to the formulation of the Boltzmann equation in its standard form, eq. (A.1), is that kinetic equilibrium between the DM particles and the heat bath is maintained throughout the entire freeze-out process. While kinetic decoupling generically indeed happens much later than chemical decoupling [133], very early kinetic decoupling can occur exactly in the situation we are interested in here, namely in the vicinity of narrow resonances [53]. In other words, eq. (A.1) runs risk of becoming invalid, and the goal of this appendix is to discuss alternatives and consequences.

One option is to solve the full Boltzmann equation at the phase-space level, which however is computationally much more challenging. Sizeable DM self-interactions are even more difficult to model in this framework than the elastic scattering of DM on relativistic heat bath particles (though significant progress has recently been made in this direction [134]). Alternatively, one can truncate the Boltzmann hierarchy at second order and only consider the much simpler coupled system of equations describing the evolution of DM number density and velocity dispersion (or ‘temperature’), respectively. Notably, these coupled Boltzmann equations actually become an exact description of the system in the limit of *large* DM self-interactions. We refer to ref. [47] for further references and a more detailed discussion of these two approaches.

For the specific case of resonant annihilations, both approaches give comparable results [47, 53]. For parameter points with $\epsilon_R \sim 0.1$, in particular, it turns out that the actual relic density can be an order of magnitude above the one naively inferred from solving eq. (A.1). This difference of course significantly exceeds the uncertainty typically associated with relic density calculations. Since the true relic density is larger than the one obtained from the naive approach, a correspondingly larger value of $\langle\sigma v\rangle$ is needed during freeze-out to compensate for this effect and avoid DM overproduction. For example, this can be achieved by decreasing ϵ_R or increasing κ . As illustrated in Fig. 2, notably, the former option can typically even be combined with a slightly *lower* value of κ , resulting in a smaller uncertainty in the relic density calculations and at the same time avoiding more stringent indirect detection constraints. Another option to suppress the relic density is to decrease the DM mass. In practice, the required shift in the model parameters is often found to be somewhat smaller than suggested by a simple estimate based on the scaling $\Omega_{\text{DM}}h^2 \propto 1/\langle\sigma v\rangle$ [53].

In the context of global scans, we are less interested in the shift of individual parameter points than in the behaviour of the allowed parameter space as a whole. Crucially, when showing two-dimensional confidence regions, we profile over all other directions in parameter space. As long as this projection includes at least some parameter points with accurate relic density calculations, the final result will also be accurate. Even in parameter regions where large uncertainties remain, these can usually be compensated for by shifts in the values of parameters that are being profiled over, as discussed above. Finally, even though there may in principle remain small parts of the two-dimensional confidence regions where such shifts are penalized by complementary constraints in *all* available directions of parameter space, these regions will be very small compared to the orders of magnitude spanned by the total allowed parameter space. Taken together, these effects substantially reduce

the impact of the uncertainty in the relic density calculation on our main results. We therefore conclude that the results of our global scans are generally robust. In the following, we discuss in more detail how our findings are expected to change with a more accurate relic density calculation.

First, we note that for the case of a sub-dominant DM component, the likelihood typically does not depend sensitively on the precise value of the relic density. This is because direct and indirect detection constraints can be evaded by many orders of magnitude (see figure 8), while constraints from accelerator experiments do not depend on $\Omega_{\text{DM}}h^2$. Inaccuracies in the relic density calculation therefore do not significantly modify the allowed regions of parameter space. For the case of asymmetric DM, on the other hand, the most interesting regions of parameter space turn out to be those with asymmetry parameter η_{DM} close to its upper bound η_{asym} . In these regions, the relic density is determined primarily by η_{DM} and is therefore less sensitive to the precise value of the annihilation rate than in the symmetric

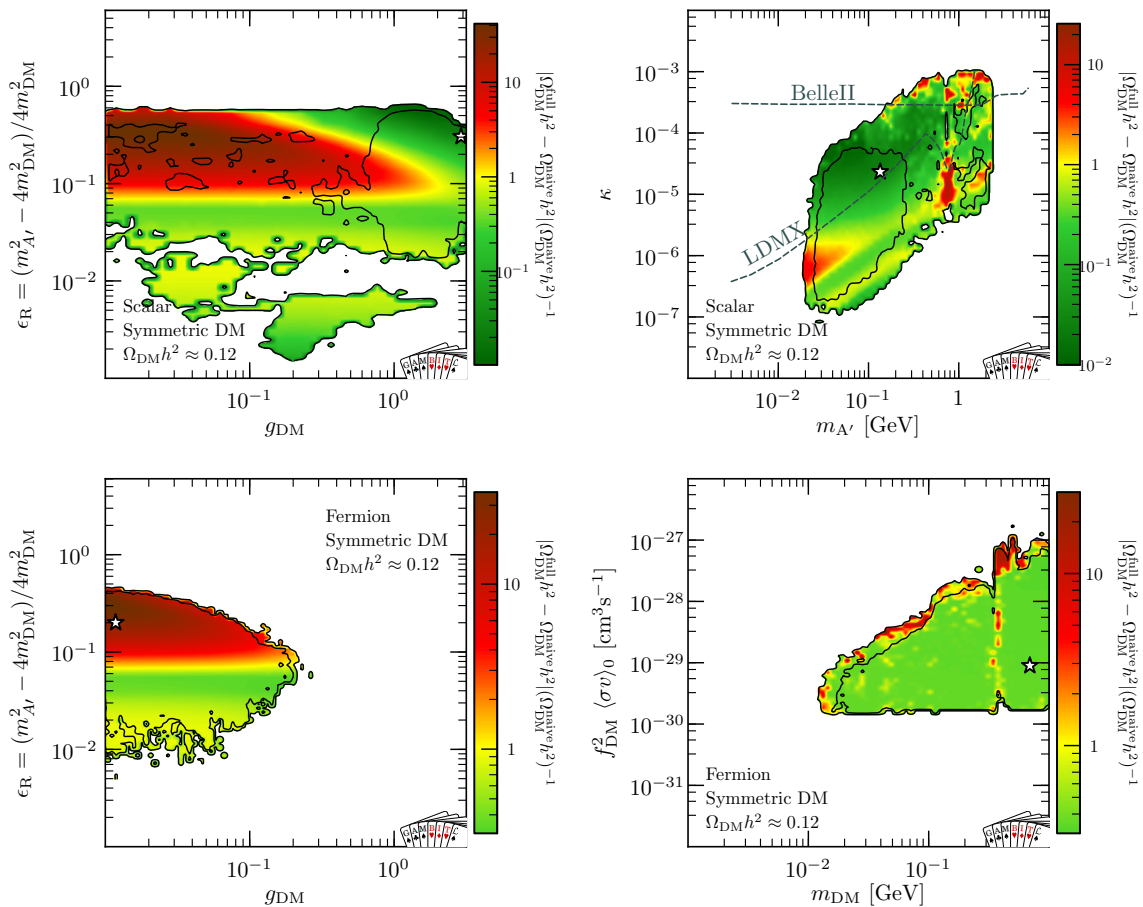


Figure 21. Estimated uncertainty in the relic density calculation for symmetric scalar DM (top row) and symmetric fermionic DM (bottom row), obtained by comparing the result from solving eq. (A.1), called $\Omega_{\text{DM}}^{\text{naive}} h^2$, to the results from ref. [47], called $\Omega_{\text{DM}}^{\text{full}} h^2$. For each pair of model parameters, we minimise the uncertainty over the remaining model parameters.

case.

In particular, as shown in figure 3, tuning η to be closer to η_{asym} would allow to avoid indirect detection constraints even for significantly larger values of κ . We therefore do not expect our scan results for asymmetric DM to change in any visible way.

For the purpose of this discussion, we therefore focus on the case of symmetric DM with $\Omega_{\text{DM}} h^2 \approx 0.12$, considering in figure 21 both scalar DM (upper panels) and fermion DM (lower panels). The colour coding in each panel corresponds to our estimate of the inaccuracy of the standard method to calculate the relic density, minimised over all parameters not shown explicitly. In other words, regions coloured in green are not affected by the uncertainties in the relic density calculation, whereas regions coloured in red are *potentially* affected and require in principle a more accurate calculation to determine whether or not they remain allowed.

In order to interpret the figure and its implications, let us first recall that the inaccuracy in the relic density calculation is by far most pronounced around $\epsilon_R \approx 0.1$, and that it becomes sizeable for resonance widths $\Gamma_{A'}/m_{A'} \lesssim 10^{-3}$ [47]. This is exactly what is seen in the left

panels of the figure. For fermion DM, in particular, the upper bound on g_{DM} implies that the invisible decay rate is always rather small – while for scalar DM the resonance can be so wide that there is no significant issue with relic density calculations even for $\epsilon_R \approx 0.1$.

However, when projecting the parameter space in terms of the observables that we are interested in for which we provide examples in the right panels of figure 21), we find that

most of the parameter regions are actually very robust and not affected by the inaccuracy of our relic density calculation. Correcting for these inaccuracies may move individual parameter points from red ‘islands’ well within the 2σ contours – but without changing the overall boundaries of the allowed parameter region. In that sense, the small red parameter regions at the upper edge of the displayed contours are of potentially greatest concern. However, as explained above, the relic density can be reduced by both a larger value of κ and a smaller value ϵ_R . The latter would not leave a visible imprint in these plots, justifying our claim that the results we have presented in the main text are robust.

An interesting open question is whether it may be possible in certain cases to increase κ while keeping all other parameters fixed, which might bring the model closer to being in reach of future experiments. We leave a more detailed study of this possibility for future work.

B Bullet Cluster constraints

The Bullet Cluster comprises a main cluster and a subcluster, each of which consists dominantly of gas and DM, such that $M^{\text{main,sub}} = M_{\text{tot}}^{\text{main,sub}} + M_{\text{gas}}^{\text{main,sub}}$. Here M_{tot} denotes the total DM mass, which for the case of multi-component DM may be larger than the mass M_{DM} of the DM component under consideration. In this case, we define the fraction of DM particles f_χ and antiparticles $f_{\bar{\chi}}$ relative to M_{tot} such that $f_\chi + f_{\bar{\chi}} = M_{\text{DM}}/M_{\text{tot}} \equiv f_{\text{DM}} \leq 1$.

For an asymmetric DM model, the self-interactions that can lead to expulsion of DM particles from the sub-cluster include those between $\chi\chi$, $\bar{\chi}\bar{\chi}$ and $\chi\bar{\chi}$. The loss of DM mass as a function of time is then given by the sum of loss in DM particles and antiparticles,

$$M_{\text{DM}}^{\text{sub}}(t) - M_{\text{DM}}^{\text{sub}}(0) = -M_{\text{tot}}^{\text{sub}} \left[f_\chi \left(1 - \exp^{-\int dt \Gamma_\chi} \right) + f_{\bar{\chi}} \left(1 - \exp^{-\int dt \Gamma_{\bar{\chi}}} \right) \right], \quad (\text{B.1})$$

where $\Gamma_{\chi(\bar{\chi})} = R_{\text{imd},\chi(\bar{\chi})} + R_{\text{cml},\chi(\bar{\chi})}$ is the rate of evaporation of DM particles (antiparticles), which is a sum of immediate evaporation (i.e. expulsion of individual particles) and cumulative evaporation (i.e. mass loss due to heating). We adopt the results from ref. [89]:

$$R_{\text{imd}} = \frac{\bar{\rho}_{\text{main}}}{m_{\text{DM}}} v_0 \sigma_{\text{imd}} \equiv \frac{\bar{\rho}_{\text{main}}}{m_{\text{DM}}} v_0 \int d\phi \int_{2\bar{v}_{\text{esc,sub}}^2/v_0^2-1}^{1-2\bar{v}_{\text{esc,sub}}^2/v_0^2} d\cos\theta \frac{d\sigma}{d\Omega} \quad (\text{B.2})$$

$$R_{\text{cml}} = \frac{\bar{\rho}_{\text{main}}}{m_{\text{DM}}} v_0 \sigma_T \equiv \frac{\bar{\rho}_{\text{main}}}{m_{\text{DM}}} v_0 \int d\phi \int_{-1}^1 d\cos\theta (1 - |\cos\theta|) \frac{d\sigma}{d\Omega}, \quad (\text{B.3})$$

where $\bar{\rho}_{\text{main}} = 2.955 \cdot 10^6 M_\odot \text{kpc}^{-3}$ is the average DM density within 150 kpc of the main cluster, m_{DM} is the DM mass, $\bar{v}_{\text{esc,sub}} = 2408 \text{ km/s}$ is the average escape velocity within 150 kpc of the subcluster, $v_0 = 3900 \text{ km/s}$ is the constant collision velocity and σ_T is the (corrected) momentum-transfer cross section (cluster and merger parameters obtained from ref. [83]).

The total evaporation rate for particles and antiparticles are

$$\Gamma_\chi = \frac{\bar{\rho}_{\text{main}}}{m_{\text{DM}}} v_0 [f_\chi(\sigma_{\text{imd},\chi\chi} + \sigma_{T,\chi\chi}) + f_{\bar{\chi}}(\sigma_{\text{imd},\chi\bar{\chi}} + \sigma_{T,\chi\bar{\chi}})] = \frac{\bar{\rho}_{\text{main}}}{m_{\text{DM}}} v_0 \sigma_{\text{eff},\chi} \quad (\text{B.4})$$

$$\Gamma_{\bar{\chi}} = \frac{\bar{\rho}_{\text{main}}}{m_{\text{DM}}} v_0 [f_{\bar{\chi}}(\sigma_{\text{imd},\bar{\chi}\bar{\chi}} + \sigma_{T,\bar{\chi}\bar{\chi}}) + f_\chi(\sigma_{\text{imd},\chi\bar{\chi}} + \sigma_{T,\chi\bar{\chi}})] = \frac{\bar{\rho}_{\text{main}}}{m_{\text{DM}}} v_0 \sigma_{\text{eff},\bar{\chi}}. \quad (\text{B.5})$$

We further make two simplifying assumptions: (i) Evaporative collisions occur only after pericenter passage, (ii) a particle ejected with velocity $\bar{v}_{\text{esc,sub}}$ takes time $\Delta t = 150 \text{ kpc}/\bar{v}_{\text{esc,sub}}$ to leave the central region of the subcluster. With these assumptions, the relative mass loss $\Delta_{\text{DM}} \equiv (M_{\text{DM},i}^{\text{sub}} - M_{\text{DM},f}^{\text{sub}})/M_{\text{tot},i}^{\text{sub}}$ (with subscript i (f) denoting the initial (final) value) can be written as

$$\Delta_{\text{DM}} = (f_{\text{DM}} - f_{\bar{\chi}}) \left(1 - \exp\left(-\bar{\Sigma}_{\text{main}} \frac{\sigma_{\text{eff},\chi}}{m_{\text{DM}}}\right) \right) + f_{\bar{\chi}} \left(1 - \exp\left(-\bar{\Sigma}_{\text{main}} \frac{\sigma_{\text{eff},\bar{\chi}}}{m_{\text{DM}}}\right) \right) \quad (\text{B.6})$$

where

$$\bar{\Sigma}_{\text{main}} = \bar{\rho}_{\text{main}} (Z - v_0 \Delta t) = 1.41 \cdot 10^9 M_\odot \text{kpc}^{-2} \quad (\text{B.7})$$

and $Z = 720 \text{ kpc}$ is the observed separation between the two clusters. This expression gives us an analytic prediction for the DM mass loss. But during major mergers, gas is also stripped away from the colliding cluster. Thus, the measured total mass loss $\Delta_{\text{M}} = (M_{\text{f}}^{\text{sub}} - M_{\text{i}}^{\text{sub}})/M_{\text{i}}^{\text{sub}}$ will include a contribution from gas. The DM mass loss and the total mass loss are related by,

$$\Delta_{\text{M}} = \Delta_{\text{DM}}(1 - R_i^{\text{sub}}) + R_i^{\text{sub}}(1 - x) \quad (\text{B.8})$$

where $R_i^{\text{sub}} = M_{\text{gas},i}^{\text{sub}}/M_{\text{i}}^{\text{sub}}$ is the ratio of initial gas mass to initial total cluster mass and $x = M_{\text{gas},f}^{\text{sub}}/M_{\text{gas},i}^{\text{sub}}$, such that $(1 - x)$ is the fraction of gas lost during the collision. While $R_{\text{f}}^{\text{sub}}$ can be obtained from observations, $R_{\text{i}}^{\text{sub}}$ is more difficult to estimate. Here we use the observed value from the main cluster after the collision as approximation, i.e. we set $R_{\text{i}}^{\text{sub}} = R_{\text{f}}^{\text{main}}$ to the observed values of main cluster and subcluster, respectively, we have

$$x = \left(\frac{R_{\text{f}}^{\text{sub}}}{1 - R_{\text{f}}^{\text{sub}}} \right) \left(\frac{1 - R_{\text{f}}^{\text{main}}}{R_{\text{f}}^{\text{main}}} \right) (1 - \Delta_{\text{DM}}). \quad (\text{B.9})$$

We use $R_{\text{f}}^{\text{main}} = 0.09 \pm 0.01$ and $R_{\text{f}}^{\text{sub}} = 0.04 \pm 0.01$ from ref. [80].

C Relativistic cross sections for beam dump DM searches

In this appendix, we provide analytic expressions for the differential cross sections for relativistic DM-electron and -nucleon scattering for both the complex scalar and Dirac DM models investigated in this work. As explained in section 3, we use these cross sections to predict the number of DM signal events in beam dump experiments with BDNMC [96]. We have obtained them by implementing the models of section 2 in FEYNRULES [135], and then using CALCHEP [136] to calculate the squared modulus of the corresponding scattering amplitudes. We have validated the outcome of this symbolic computations through direct analytical calculations. While in the case of complex scalar DM the relativistic cross sections for DM-electron and -nucleon scattering were already implemented in BDNMC, the implementation in the BDNMC code of the analogous cross sections for the case of Dirac DM has been performed within this work.

For the differential cross section for DM-electron scattering, in the laboratory frame we find

$$\frac{d\sigma_{\text{eDM}}(E_{\vec{p}}, E_{\vec{k}'})}{dE_{\vec{k}'}} = \frac{1}{32\pi m_e (E_{\vec{p}}^2 - m_{\text{DM}}^2)} \overline{|\mathcal{M}_{\text{eDM}}(E_{\vec{p}}, E_{\vec{k}'})|^2}, \quad (\text{C.1})$$

where

$$\overline{|\mathcal{M}_{\text{eDM}}(E_{\vec{p}}, E_{\vec{k}'})|^2} = 8g_{\text{DM}}^2 \kappa^2 e^2 \frac{2m_e^2 E_{\vec{p}}^2 - m_e (E_{\vec{k}'} - m_e) f(E_{\vec{p}}, E_{\vec{k}'})}{(m_{A'}^2 + 2m_e E_{\vec{k}'} - 2m_e^2)^2}, \quad (\text{C.2})$$

and

$$f(E_{\vec{p}}, E_{\vec{k}'}) = \begin{cases} 2m_e E_{\vec{p}} + m_{\text{DM}}^2 & \text{Complex scalar DM} \\ 2m_e E_{\vec{p}} - m_e E_{\vec{k}'} + 2m_e^2 + m_{\text{DM}}^2 & \text{Dirac DM,} \end{cases} \quad (\text{C.3})$$

while $E_{\vec{p}}$ ($E_{\vec{k}'}$) is the initial (final) state DM (electron) energy. Eq. (C.1) agrees with eq. (3) in ref. [137]. For the differential cross section for DM-nucleon scattering, in the laboratory frame we find

$$\frac{d\sigma_{\text{nDM}}(E_{\vec{p}}, E_{\vec{p}'})}{dE_{\vec{p}'}} = \frac{1}{32\pi m_n (E_{\vec{p}}^2 - m_{\text{DM}}^2)} \overline{|\mathcal{M}_{\text{nDM}}(E_{\vec{p}}, E_{\vec{p}'})|^2}, \quad (\text{C.4})$$

where

$$\overline{|\mathcal{M}_{\text{nDM}}(E_{\vec{p}}, E_{\vec{p}'})|^2} = g_{\text{DM}}^2 \frac{F_1^2 \mathcal{A}(E_{\vec{p}}, E_{\vec{p}'}) + F_2^2 \mathcal{B}(E_{\vec{p}}, E_{\vec{p}'}) + F_1 F_2 \mathcal{C}(E_{\vec{p}}, E_{\vec{p}'})}{[m_{A'}^2 + 2m_n (E_{\vec{p}} - E_{\vec{p}'})]^2}, \quad (\text{C.5})$$

and

$$\begin{aligned} \mathcal{A}(E_{\vec{p}}, E_{\vec{p}'}) &= \begin{cases} 8m_n [E_{\vec{p}'} (2E_{\vec{p}} m_n + m_{\text{DM}}^2) - E_{\vec{p}} m_{\text{DM}}^2] \\ 8m_n [E_{\vec{p}}^2 m_n + E_{\vec{p}'} (m_n E_{\vec{p}} + m_n^2 + m_{\text{DM}}^2) - E_{\vec{p}} (m_n^2 + m_{\text{DM}}^2)] \end{cases} \\ \mathcal{B}(E_{\vec{p}}, E_{\vec{p}'}) &= \begin{cases} 2m_n (E_{\vec{p}} - E_{\vec{p}'}) [E_{\vec{p}}^2 + 2(E_{\vec{p}} + m_n) E_{\vec{p}'} + E_{\vec{p}'}^2 - 2E_{\vec{p}} m_n - 4m_{\text{DM}}^2] \\ 4m_n (E_{\vec{p}} - E_{\vec{p}'}) [(2E_{\vec{p}} - m_n) E_{\vec{p}'} + E_{\vec{p}'} m_n - 2m_{\text{DM}}^2] \end{cases} \\ \mathcal{C}(E_{\vec{p}}, E_{\vec{p}'}) &= \begin{cases} -8m_n (E_{\vec{p}} - E_{\vec{p}'}) (-m_n E_{\vec{p}'} + E_{\vec{p}} m_n + 2m_{\text{DM}}^2) & \text{Complex scalar DM} \\ 16m_n (E_{\vec{p}} - E_{\vec{p}'}) (-m_n E_{\vec{p}'} + E_{\vec{p}} m_n - m_{\text{DM}}^2) & \text{Dirac DM.} \end{cases} \end{aligned} \quad (\text{C.6})$$

Here, $E_{\vec{p}'}$ is the outgoing DM particle energy, m_n is the nucleon mass, while F_1 and F_2 are momentum-dependent nucleon form factors [138]. Eq. (C.4) agrees with eq. (B.10) in ref. [138], and includes the interference terms (i.e. terms proportional to $F_1 F_2$) that are missing in eq. (14) of ref. [92].

D Observable predictions from Bayesian scans

In this appendix we provide additional results from our Bayesian scans, showing posterior probabilities for the parameters and observables relevant for various experiments. These figures allow us to identify promising targets for future experiments and to quantify the (Bayesian) probability of a detection, i.e. the fraction of the credible region that can be probed. The case of symmetric fermionic DM is shown in figure 22, while the case of asymmetric fermionic DM is shown in figure 23. As expected, the latter case allows for much larger couplings and therefore for more promising detection prospects. Finally the case of symmetric scalar DM is shown in figure 24.

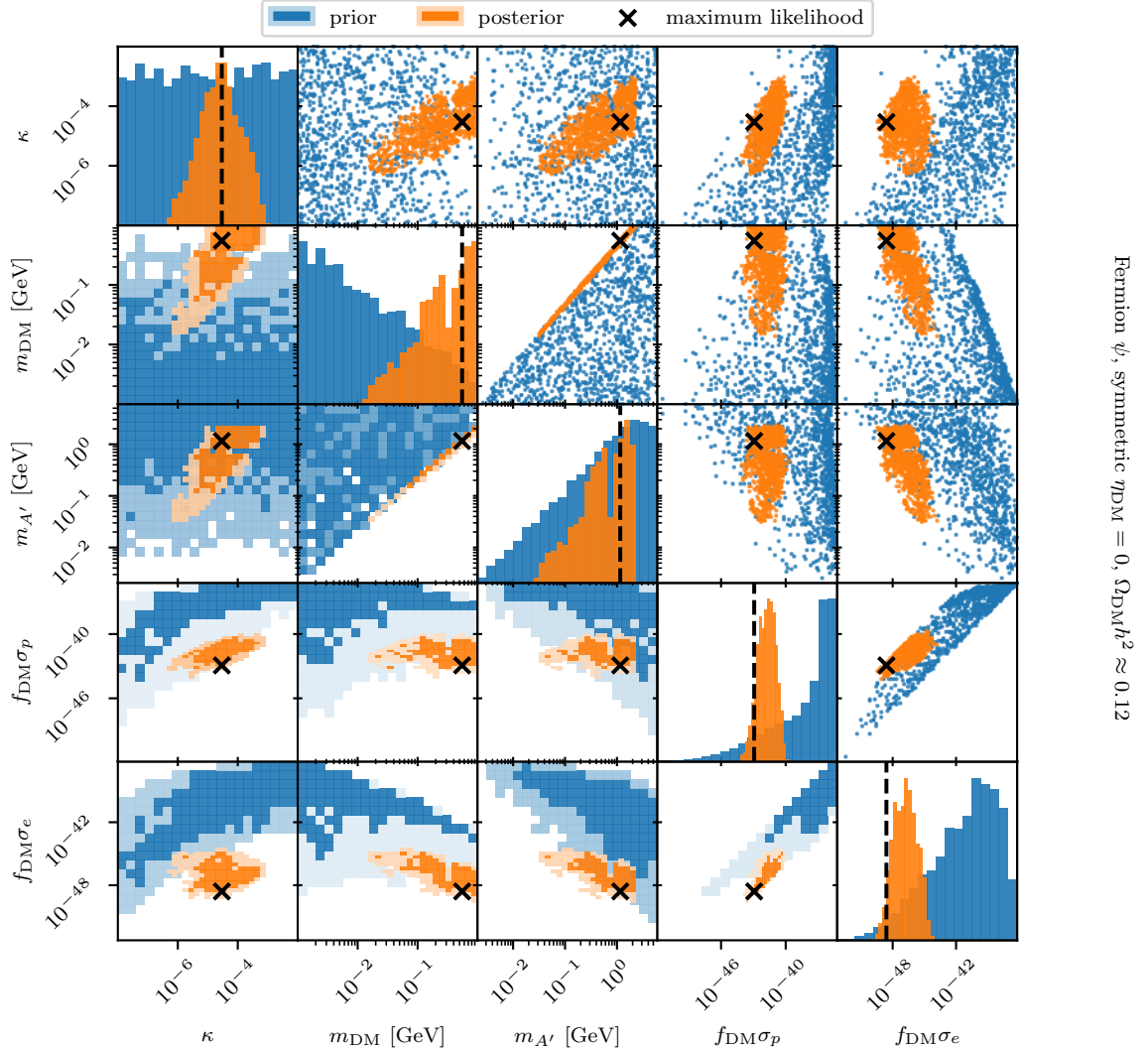
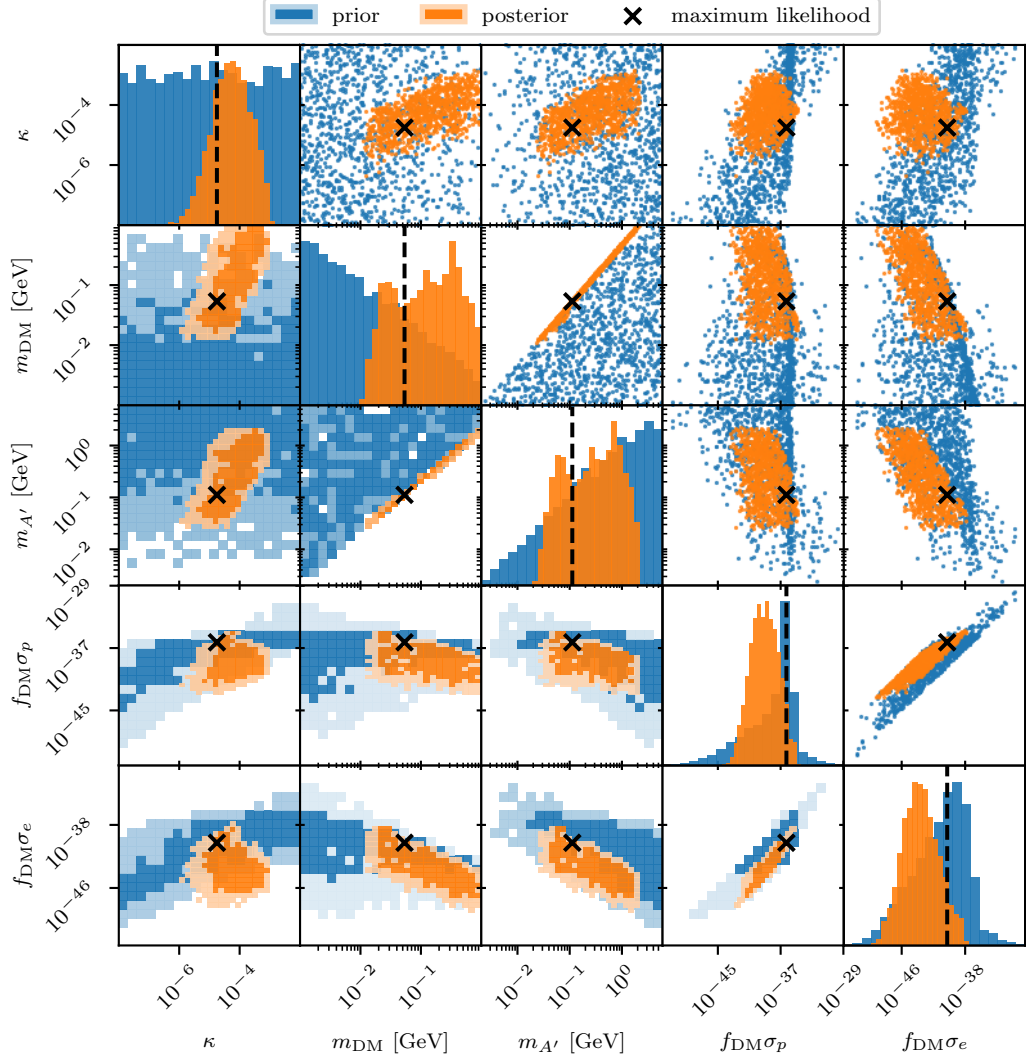


Figure 22. Prior (blue) and posterior (orange) probabilities for symmetric fermionic DM in terms of the most relevant parameters and observables.

E GAMBIT implementation

E.1 New models

Two new model trees have been added to the GAMBIT model hierarchy, according to the fermionic and scalar sub-GeV models described in this work. The top of the model trees are `SubGeVDM_fermion` and `SubGeVDM_scalar`, respectively. Each of the trees contain a resonant DM model where the mass splitting $\epsilon_R = (m_{A'}^2 - 4m_{\text{DM}}^2)/(4m_{\text{DM}}^2)$ replaces the dark photon mass as a model parameter, `Resonant_SubGeVDM_fermion` and `Resonant_SubGeVDM_scalar`. Furthermore, for each of the four models above, there is a companion model where the asymmetry parameter η_{DM} is substituted by the combination $\eta_{\text{DM}} m_{\text{DM}}$



Fermion ψ , asymmetric $\eta_{\text{DM}} \neq 0$, $\Omega_{\text{DM}} h^2 \approx 0.12$

Figure 23. Prior (blue) and posterior (orange) probabilities for asymmetric fermionic DM in terms of the most relevant parameters and observables.

called, respectively, [SubGeVDM_fermion_RDprior](#), [Resonant_SubGeVDM_fermion_RDprior](#), for fermionic DM, and [SubGeVDM_scalar_RDprior](#) and [Resonant_SubGeVDM_scalar_RDprior](#) for scalar DM. Finally, two reparametrisations of the general [SubGeVDM_fermion](#) are also available, where the dark matter coupling g_{DM} is replaced by the DM-electron cross section σ_e , [SubGeVDM_fermion_sigmae](#), or the DM-nucleon cross section σ_N , [SubGeVDM_fermion_sigman](#).

SubGeVDM_fermion: $m_{\text{DM}}, m_{A'}, g_{\text{DM}}, \kappa, \eta_{\text{DM}}$

Sub-GeV DM fermion model parametrised with the DM mass m_{DM} , the dark photon mass $m_{A'}$, the DM-dark photon coupling g_{DM} , the kinetic mixing parameter κ and the asymmetry parameter η_{DM} .

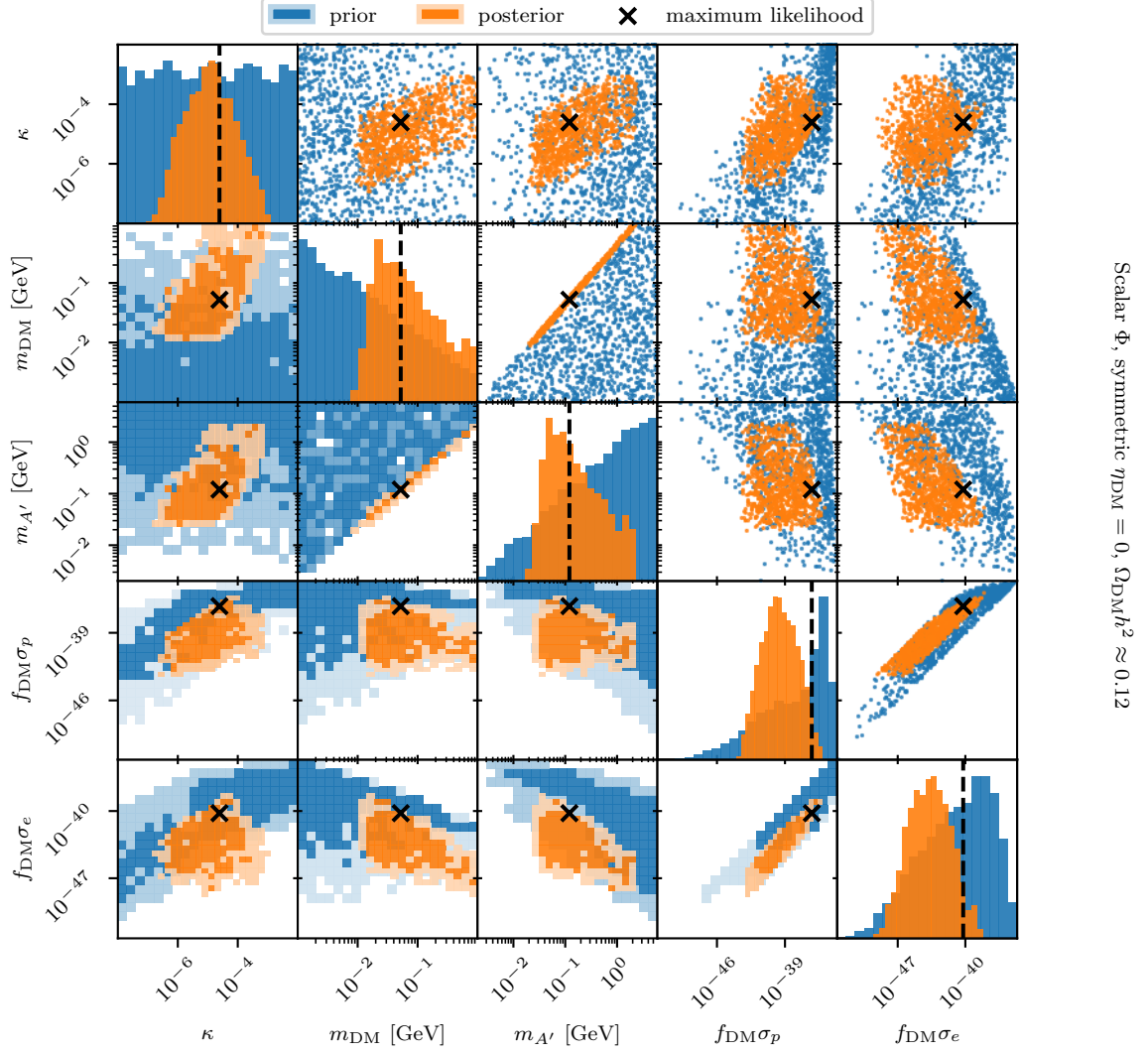


Figure 24. Prior (blue) and posterior (orange) probabilities for scalar DM in terms of the most relevant parameters and observables.

SubGeVDM_fermion_sigmae: $m_{\text{DM}}, m_{A'}, \text{sigmae}, \text{kappa}, \text{etaDM}$

Child model of [SubGeVDM_fermion](#) with the DM-electron cross section sigmae as a parameter instead of the coupling g_{DM} .

SubGeVDM_fermion_sigmaN: $m_{\text{DM}}, m_{A'}, \text{sigmaN}, \text{kappa}, \text{etaDM}$

Child model of [SubGeVDM_fermion](#) with the DM-nucleon cross section sigmaN as a parameter instead of the coupling g_{DM} .

SubGeVDM_fermion_RDprior: $m_{\text{DM}}, m_{A'}, g_{\text{DM}}, \text{kappa}, \text{etaDM}_{\text{mDM}}$

Child model of [SubGeVDM_fermion](#) with a relic density prior, i.e. substituting the asymmetry parameter etaDM with the combination $\text{etaDM}_{\text{mDM}}$.

Resonant_SubGeVDM_fermion: $m_{\text{DM}}, \text{epsR}, g_{\text{DM}}, \text{kappa}, \text{etaDM}$

Child model of [SubGeVDM_fermion](#) with in the resonance $m_{\text{DM}} \sim 2m_{A'}$, so substituting the parameter m_{Ap} by the mass splitting epsR defined in eq.(2.6).

Resonant_SubGeVDM_fermion_RDprior: $m_{\text{DM}}, \text{epsR}, g_{\text{DM}}, \text{kappa}, \text{etaDM}_m$

Child model of [SubGeVDM_fermion](#) using both the resonance parameter epsR and the relic density prior parameter etaDM_m .

SubGeVDM_scalar: $m_{\text{DM}}, m_{\text{Ap}}, g_{\text{DM}}, \text{kappa}, \text{etaDM}$

Sub-GeV DM scalar model parametrised with the DM mass m_{DM} , the dark photon mass m_{Ap} , the DM-dark photon coupling g_{DM} , the kinetic mixing parameter kappa and the asymmetry parameter etaDM .

SubGeVDM_scalar_RDprior: $m_{\text{DM}}, m_{\text{Ap}}, g_{\text{DM}}, \text{kappa}, \text{etaDM}_m$

Child model of [SubGeVDM_scalar](#) with a relic density prior, i.e. substituting the asymmetry parameter etaDM with the combination etaDM_m .

Resonant_SubGeVDM_scalar: $m_{\text{DM}}, \text{epsR}, g_{\text{DM}}, \text{kappa}, \text{etaDM}$

Child model of [SubGeVDM_scalar](#) with in the resonance $m_{\text{DM}} \sim 2m_{A'}$, so substituting the parameter m_{Ap} by the mass splitting epsR defined in eq.(2.6).

Resonant_SubGeVDM_scalar_RDprior $m_{\text{DM}}, \text{epsR}, g_{\text{DM}}, \text{kappa}, \text{etaDM}_m$

Child model of [SubGeVDM_scalar](#) using both the resonance parameter epsR and the relic density prior parameter etaDM_m .

To complement the model descriptions above, a capability called [SubGeVDM_spectrum](#) was added to the SpecBit module [139] to set up relevant spectrum details.

E.2 Updates to DarkBit, CosmoBit and ColliderBit

In addition to the new models, this work has also expanded the likelihood computations of the DarkBit [26], CosmoBit [27] and ColliderBit [140] modules. The full list of new capabilities, along with their module functions, dependencies and backend requirements, is given in tables 2-5.

In DarkBit, many capabilities are supplemented with module functions for the sub-GeV models, including those for computing the process catalog, [TH_ProcessCatalog_SubGeVDM_fermion](#) and [TH_ProcessCatalog_SubGeVDM_scalar](#), those that calculate the the direct detection couplings, [DD_couplings_SubGeVDM_fermion](#) and [DD_couplings_SubGeVDM_scalar](#), and those storing the DM properties, [DarkMatter_ID_SubGeVDM_fermion](#) and [DarkMatterConj_ID_SubGeVDM_fermion](#), for fermion DM, and [DarkMatter_ID_SubGeVDM_scalar](#), and [DarkMatterConj_ID_SubGeVDM_scalar](#) for scalar DM.

New capabilities added for this project include [RD_oh2_aDM](#), which computes the relic abundance for an asymmetric DM model, [ID_suppression](#), which calculates the suppression factor of ID signals due to under abundant DM, [DM_mass_loss](#) computes the loss in mass of subcluster due to self-interactions, [BulletCluster_1nL](#) is the likelihood function for the Bullet Cluster, [Xray_loglikelihoods](#) calculates the constraints from the annihilation of DM into X-rays, [set_gamLike_GC_halo](#) initialises the DM halo in GAMLIKE, [LocalHalo_GeV](#) provides and alternative local halo parametrisation with all parameter in GeV and [sigma_e](#) computes the DM-electron cross section. Furthermore, many new experimental likelihoods are added

for direct detection of DM using electron recoils and nuclear recoils via the Migdal effect. The capabilities for these likelihoods are of the form `<experiment>_LogLikelihood`, where the `<experiment>` label takes into account not only the experiment but also the type of interaction if there is more than one type. The likelihoods included are for the experiments: `XENON1T_ER`, `DarkSide50_ER`, `DarkSide50_ER_2023`, `PandaX_4T_ER`, `SENSEI_at_MINOS`, `CDMS_HVeV_2020`, `DAMIC_M_2023`, `XENON1T_Migdal`, `DarkSide50_Migdal`, `DarkSide50_Migdal_2023` and `PandaX_4T_Migdal`. Lastly, the capability `RD_oh2_underprediction` calculates the expected underprediction of the relic abundance by not using the standard Boltzmann solution (see appendix A.2 above) from the tabulated results from [47].

The only changes done to CosmoBit for this work are those to enable the usage of ALTERBBN with the sub-GeV DM models, as well as new capabilities to extract the value of N_{eff} after BBN. These are `Neff_after_BBN`, which get the N_{eff} value after BBN from ALTERBBN, and `N_eff_likelihood_Planck_BAO`, which computes the likelihood for N_{eff} given Planck + BAO data.

Finally, the modifications to ColliderBit include a new capability to calculate the likelihood to see dark photons at BaBar, `BaBar_single_photon_LogLike`, and a new module function `SubGeVDM_results` for the capability `AllAnalysisNumbers` that implements limits from the beam dump experiments LSND, MiniBoone and NA64 as interpolated yields.

E.3 Backend interfaces

For the purpose of this study two new backend interfaces have been implemented, to DARKCAST and to OBSCURA. Furthermore, important changes were performed to the backend interface to DARKSUSY in order to allow the computation of the relic abundance in asymmetric DM models (more about that in appendix A), and that of ALTERBBN, to allow the input of the DM parameters and the return of N_{eff} .

A new backend interface was created to DARKCAST v1.1 for the calculation of the decay widths and branching fractions of the dark photon. Convenience backend functions were created, `dark_photon_decay_width` and `dark_photon_branching_fraction` for single final state, and `dark_photon_decay_width_multi` and `dark_photon_branching_fraction_multi` for multiple final states.

Lastly, the external tool OBSCURA, designed to compute likelihoods from direct detection experiments, was used to calculate the constraints from electron recoils and nuclear recoils using the Migdal effect. Since OBSCURA is written in C++, we use BOSS to create the hierarchy of abstract and wrapper classes required to use them inside GAMBIT (see section 4.5 of ref. [25] for more details on how BOSS works). The classes used from OBSCURA are `Standard_Halo_Model` for setting the DM halo model, `DM_Particle_SI` the DM particle model and three models for detectors: crystal experiments, `DM_Detector_Crystal`, ionization experiments with electron recoils, `DM_Detector_Ionization_ER`, and ionization experiments with nuclear recoils via the Migdal effect, `DM_Detector_Ionization_Migdal`. Using those classes, the OBSCURA functions for which backend interfaces have been implemented are `XENON1T_S2_ER`, `DarkSide50_S2_ER`, `DarkSide50_S2_ER_2023`, `PandaX_S2_4T_ER`, `SENSEI_at_MINOS`, `CDMS_HVeV_2020`, `DAMIC_M_2023`, which compute the likelihood of DM-electron electron scatterings, and `XENON1T_Migdal`, `DarkSide50_Migdal`, `DarkSide50_Migdal_2023` and `PandaX_4T_Migdal`, that compute the likelihood of DM-nucleon scattering with Migdal effect.

References

- [1] V. Iršič, M. Viel, M. G. Haehnelt, J. S. Bolton, and G. D. Becker, *First constraints on fuzzy dark matter from Lyman- α forest data and hydrodynamical simulations*, *Phys. Rev. Lett.* **119** (2017), no. 3 031302, [[1703.04683](#)].
- [2] K. K. Rogers and H. V. Peiris, *Strong Bound on Canonical Ultralight Axion Dark Matter from the Lyman-Alpha Forest*, *Phys. Rev. Lett.* **126** (2021), no. 7 071302, [[2007.12705](#)].
- [3] P. F. Depta, M. Hufnagel, K. Schmidt-Hoberg, and S. Wild, *BBN constraints on the annihilation of MeV-scale dark matter*, *JCAP* **04** (2019) 029, [[1901.06944](#)].
- [4] N. Sabti, J. Alvey, M. Escudero, M. Fairbairn, and D. Blas, *Refined Bounds on MeV-scale Thermal Dark Sectors from BBN and the CMB*, *JCAP* **01** (2020) 004, [[1910.01649](#)].
- [5] K. Griest and M. Kamionkowski, *Unitarity Limits on the Mass and Radius of Dark Matter Particles*, *Phys. Rev. Lett.* **64** (1990) 615.
- [6] G. Arcadi, M. Dutra, P. Ghosh, M. Lindner, Y. Mambrini, et al., *The waning of the WIMP? A review of models, searches, and constraints*, *Eur. Phys. J. C* **78** (2018), no. 3 203, [[1703.07364](#)].
- [7] G. Arcadi, D. Cabo-Almeida, M. Dutra, P. Ghosh, M. Lindner, et al., *The Waning of the WIMP: Endgame?*, [2403.15860](#).
- [8] B. W. Lee and S. Weinberg, *Cosmological Lower Bound on Heavy Neutrino Masses*, *Phys. Rev. Lett.* **39** (1977) 165–168.
- [9] S. Knapen, T. Lin, and K. M. Zurek, *Light Dark Matter: Models and Constraints*, *Phys. Rev. D* **96** (2017), no. 11 115021, [[1709.07882](#)].
- [10] T. Lin, *Dark matter models and direct detection*, *PoS* **333** (2019) 009, [[1904.07915](#)].
- [11] M. Fabbrichesi, E. Gabrielli, and G. Lanfranchi, *The Dark Photon*, [2005.01515](#).
- [12] M. Battaglieri et al., *US Cosmic Visions: New Ideas in Dark Matter 2017: Community Report*, in *U.S. Cosmic Visions: New Ideas in Dark Matter*, 7, 2017. [1707.04591](#).
- [13] T. R. Slatyer, N. Padmanabhan, and D. P. Finkbeiner, *CMB Constraints on WIMP Annihilation: Energy Absorption During the Recombination Epoch*, *Phys. Rev. D* **80** (2009) 043526, [[0906.1197](#)].
- [14] **Planck Collaboration**, N. Aghanim et al., *Planck 2018 results. VI. Cosmological parameters*, *Astron. Astrophys.* **641** (2020) A6, [[1807.06209](#)]. [Erratum: *Astron. Astrophys.* 652, C4 (2021)].
- [15] M. Cirelli, N. Fornengo, J. Koechler, E. Pinetti, and B. M. Roach, *Putting all the X in one basket: Updated X-ray constraints on sub-GeV Dark Matter*, *JCAP* **07** (2023) 026, [[2303.08854](#)].
- [16] C. Boehm and P. Fayet, *Scalar dark matter candidates*, *Nucl. Phys. B* **683** (2004) 219–263, [[hep-ph/0305261](#)].
- [17] E. Bernreuther, S. Heeba, and F. Kahlhoefer, *Resonant sub-GeV Dirac dark matter*, *JCAP* **03** (2021) 040, [[2010.14522](#)].
- [18] N. Brahma, S. Heeba, and K. Schutz, *Resonant pseudo-Dirac dark matter as a sub-GeV thermal target*, *Phys. Rev. D* **109** (2024), no. 3 035006, [[2308.01960](#)].
- [19] T. Lin, H.-B. Yu, and K. M. Zurek, *On Symmetric and Asymmetric Light Dark Matter*, *Phys. Rev. D* **85** (2012) 063503, [[1111.0293](#)].
- [20] E. Izaguirre, G. Krnjaic, P. Schuster, and N. Toro, *Analyzing the Discovery Potential for Light Dark Matter*, *Phys. Rev. Lett.* **115** (2015), no. 25 251301, [[1505.00011](#)].

- [21] J. Alexander et al., *Dark Sectors 2016 Workshop: Community Report*, 8, 2016. [1608.08632](#).
- [22] A. Berlin, N. Blinov, G. Krnjaic, P. Schuster, and N. Toro, *Dark Matter, Millicharges, Axion and Scalar Particles, Gauge Bosons, and Other New Physics with LDMX*, *Phys. Rev. D* **99** (2019), no. 7 075001, [[1807.01730](#)].
- [23] J. Beacham et al., *Physics Beyond Colliders at CERN: Beyond the Standard Model Working Group Report*, *J. Phys. G* **47** (2020), no. 1 010501, [[1901.09966](#)].
- [24] A. Berlin, P. deNiverville, A. Ritz, P. Schuster, and N. Toro, *Sub-GeV dark matter production at fixed-target experiments*, *Phys. Rev. D* **102** (2020), no. 9 095011, [[2003.03379](#)].
- [25] **GAMBIT Collaboration**, P. Athron et al., *GAMBIT: The Global and Modular Beyond-the-Standard-Model Inference Tool*, *Eur. Phys. J. C* **77** (2017), no. 11 784, [[1705.07908](#)]. [Addendum: *Eur.Phys.J.C* 78, 98 (2018)].
- [26] T. Bringmann et al., *DarkBit: A GAMBIT module for computing dark matter observables and likelihoods*, *Eur. Phys. J. C* **77** (2017), no. 12 831, [[1705.07920](#)].
- [27] J. J. Renk et al., *CosmoBit: A GAMBIT module for computing cosmological observables and likelihoods*, *JCAP* **02** (2021) 022, [[2009.03286](#)].
- [28] S. Bloor, T. E. Gonzalo, P. Scott, C. Chang, A. Raklev, et al., *The GAMBIT Universal Model Machine: from Lagrangians to likelihoods*, *Eur. Phys. J. C* **81** (2021), no. 12 1103, [[2107.00030](#)].
- [29] **GAMBIT Collaboration**, P. Athron et al., *Status of the scalar singlet dark matter model*, *Eur. Phys. J. C* **77** (2017), no. 8 568, [[1705.07931](#)].
- [30] **GAMBIT Collaboration**, P. Athron et al., *Global analyses of Higgs portal singlet dark matter models using GAMBIT*, *Eur. Phys. J. C* **79** (2019), no. 1 38, [[1808.10465](#)].
- [31] S. Hoof, F. Kahlhoefer, P. Scott, C. Weniger, and M. White, *Axion global fits with Peccei-Quinn symmetry breaking before inflation using GAMBIT*, *JHEP* **03** (2019) 191, [[1810.07192](#)]. [Erratum: *JHEP* 11, 099 (2019)].
- [32] **GAMBIT Collaboration**, P. Athron et al., *Thermal WIMPs and the scale of new physics: global fits of Dirac dark matter effective field theories*, *Eur. Phys. J. C* **81** (2021), no. 11 992, [[2106.02056](#)].
- [33] C. Chang, P. Scott, T. E. Gonzalo, F. Kahlhoefer, A. Kvellestad, et al., *Global fits of simplified models for dark matter with GAMBIT: I. Scalar and fermionic models with s-channel vector mediators*, *Eur. Phys. J. C* **83** (2023), no. 3 249, [[2209.13266](#)].
- [34] C. Chang, P. Scott, T. E. Gonzalo, F. Kahlhoefer, and M. White, *Global fits of simplified models for dark matter with GAMBIT: II. Vector dark matter with an s-channel vector mediator*, *Eur. Phys. J. C* **83** (2023), no. 8 692, [[2303.08351](#)]. [Erratum: *Eur.Phys.J.C* 83, 768 (2023)].
- [35] P. Athron et al., *Global fits of axion-like particles to XENON1T and astrophysical data*, *JHEP* **05** (2021) 159, [[2007.05517](#)].
- [36] C. Balázs et al., *Cosmological constraints on decaying axion-like particles: a global analysis*, *JCAP* **12** (2022) 027, [[2205.13549](#)].
- [37] E. Stueckelberg, *Interaction energy in electrodynamics and in the field theory of nuclear forces*, *Helv. Phys. Acta* **11** (1938) 225–244.
- [38] B. Holdom, *Two $U(1)$'s and Epsilon Charge Shifts*, *Phys. Lett. B* **166** (1986) 196–198.
- [39] K. S. Babu, C. F. Kolda, and J. March-Russell, *Implications of generalized $Z - Z'$ mixing*, *Phys. Rev. D* **57** (1998) 6788–6792, [[hep-ph/9710441](#)].
- [40] C. Boehm, X. Chu, J.-L. Kuo, and J. Pradler, *Scalar dark matter candidates revisited*, *Phys.*

Rev. D **103** (2021), no. 7 075005, [[2010.02954](#)].

- [41] J. L. Feng and J. Smolinsky, *Impact of a resonance on thermal targets for invisible dark photon searches*, *Phys. Rev. D* **96** (2017), no. 9 095022, [[1707.03835](#)].
- [42] V. V. Ezhela, S. B. Lugovsky, and O. V. Zenin, *Hadronic part of the muon $g - 2$ estimated on the $\sigma_{tot}^{2003}(e^+e^- \rightarrow \text{hadrons})$ evaluated data compilation*, [hep-ph/0312114](#).
- [43] P. Ilten, Y. Soreq, M. Williams, and W. Xue, *Serendipity in dark photon searches*, *JHEP* **06** (2018) 004, [[1801.04847](#)].
- [44] **Particle Data Group Collaboration**, P. Zyla et al., *Review of Particle Physics*, *PTEP* **2020** (2020), no. 8 083C01.
- [45] M. Ibe, H. Murayama, and T. T. Yanagida, *Breit-Wigner Enhancement of Dark Matter Annihilation*, *Phys. Rev. D* **79** (2009) 095009, [[0812.0072](#)].
- [46] W.-L. Guo and Y.-L. Wu, *Enhancement of Dark Matter Annihilation via Breit-Wigner Resonance*, *Phys. Rev. D* **79** (2009) 055012, [[0901.1450](#)].
- [47] T. Binder, T. Bringmann, M. Gustafsson, and A. Hryczuk, *Dark matter relic abundance beyond kinetic equilibrium*, *Eur. Phys. J. C* **81** (2021) 577, [[2103.01944](#)].
- [48] J. A. Evans, S. Gori, and J. Shelton, *Looking for the WIMP Next Door*, *JHEP* **02** (2018) 100, [[1712.03974](#)].
- [49] M. J. Reid et al., *Trigonometric Parallaxes of High Mass Star Forming Regions: the Structure and Kinematics of the Milky Way*, *Astrophys. J.* **783** (2014) 130, [[1401.5377](#)].
- [50] A. J. Deason, A. Fattahi, V. Belokurov, N. W. Evans, R. J. J. Grand, et al., *The local high-velocity tail and the Galactic escape speed*, *Mon. Not. Roy. Astron. Soc.* **485** (2019), no. 3 3514–3526, [[1901.02016](#)].
- [51] T. Bringmann, J. Edsjö, P. Gondolo, P. Ullio, and L. Bergström, *DarkSUSY 6 : An Advanced Tool to Compute Dark Matter Properties Numerically*, *JCAP* **07** (2018) 033, [[1802.03399](#)].
- [52] P. Gondolo and G. Gelmini, *Cosmic abundances of stable particles: Improved analysis*, *Nucl. Phys. B* **360** (1991) 145–179.
- [53] T. Binder, T. Bringmann, M. Gustafsson, and A. Hryczuk, *Early kinetic decoupling of dark matter: when the standard way of calculating the thermal relic density fails*, *Phys. Rev. D* **96** (2017), no. 11 115010, [[1706.07433](#)]. [Erratum: *Phys.Rev.D* 101, 099901 (2020)].
- [54] M. L. Graesser, I. M. Shoemaker, and L. Vecchi, *Asymmetric WIMP dark matter*, *JHEP* **10** (2011) 110, [[1103.2771](#)].
- [55] N. F. Bell, S. Horiuchi, and I. M. Shoemaker, *Annihilating Asymmetric Dark Matter*, *Phys. Rev. D* **91** (2015), no. 2 023505, [[1408.5142](#)].
- [56] A. Arbey, J. Auffinger, K. P. Hickerson, and E. S. Jentsen, *AlterBBN v2: A public code for calculating Big-Bang nucleosynthesis constraints in alternative cosmologies*, *Comput. Phys. Commun.* **248** (2020) 106982, [[1806.11095](#)].
- [57] T. R. Slatyer, *Indirect Dark Matter Signatures in the Cosmic Dark Ages II. Ionization, Heating and Photon Production from Arbitrary Energy Injections*, *Phys. Rev. D* **93** (2016), no. 2 023521, [[1506.03812](#)].
- [58] A. Coogan, L. Morrison, and S. Profumo, *Hazma: A Python Toolkit for Studying Indirect Detection of Sub-GeV Dark Matter*, *JCAP* **01** (2020) 056, [[1907.11846](#)].
- [59] A. Coogan, L. Morrison, T. Plehn, S. Profumo, and P. Reimitz, *Hazma meets HERWIG4DM: precision gamma-ray, neutrino, and positron spectra for light dark matter*, *JCAP* **11** (2022) 033, [[2207.07634](#)].
- [60] T. Plehn, P. Reimitz, and P. Richardson, *Hadronic Footprint of GeV-Mass Dark Matter*,

SciPost Phys. **8** (2020) 092, [[1911.11147](#)].

- [61] P. Stöcker, M. Krämer, J. Lesgourgues, and V. Poulin, *Exotic energy injection with ExoCLASS: Application to the Higgs portal model and evaporating black holes*, *JCAP* **03** (2018) 018, [[1801.01871](#)].
- [62] P. Braat and M. Hufnagel. In preparation.
- [63] **Fermi-LAT, DES Collaboration**, A. Albert et al., *Searching for Dark Matter Annihilation in Recently Discovered Milky Way Satellites with Fermi-LAT*, *Astrophys. J.* **834** (2017), no. 2 110, [[1611.03184](#)].
- [64] J. W. Foster, Y. Park, B. R. Safdi, Y. Soreq, and W. L. Xu, *Search for dark matter lines at the Galactic Center with 14 years of Fermi data*, *Phys. Rev. D* **107** (2023), no. 10 103047, [[2212.07435](#)].
- [65] G. Vedrenne, J. P. Roques, V. Schönfelder, P. Mandrou, G. G. Lichti, et al., *SPI: The spectrometer aboard INTEGRAL*, *Astronomy and Astrophysics* **411** (Nov., 2003) L63–L70.
- [66] **Fermi-LAT Collaboration**, W. B. Atwood et al., *The Large Area Telescope on the Fermi Gamma-ray Space Telescope Mission*, *Astrophys. J.* **697** (2009) 1071–1102, [[0902.1089](#)].
- [67] T. Aramaki et al., *Snowmass2021 Cosmic Frontier: The landscape of cosmic-ray and high-energy photon probes of particle dark matter*, [2203.06894](#).
- [68] M. Cirelli, N. Fornengo, B. J. Kavanagh, and E. Pinetti, *Integral X-ray constraints on sub-GeV Dark Matter*, *Phys. Rev. D* **103** (2021), no. 6 063022, [[2007.11493](#)].
- [69] L. Bouchet, A. W. Strong, T. A. Porter, I. V. Moskalenko, E. Jourdain, et al., *Diffuse Emission Measurement with the SPECTROMETER on INTEGRAL as an Indirect Probe of Cosmic-Ray Electrons and Positrons*, *The Astrophysical Journal* **739** (Sept., 2011) 29, [[1107.0200](#)].
- [70] K. Mori et al., *NuSTAR Hard X-ray Survey of the Galactic Center Region. I. Hard X-ray Morphology and Spectroscopy of the Diffuse Emission*, *Astrophys. J.* **814** (2015), no. 2 94, [[1510.04631](#)].
- [71] J. Hong et al., *NuSTAR Hard X-ray Survey of the Galactic Center Region II: X-ray Point Sources*, *Astrophys. J.* **825** (2016), no. 2 132, [[1605.03882](#)].
- [72] B. M. Roach, K. C. Y. Ng, K. Perez, J. F. Beacom, S. Horiuchi, et al., *NuSTAR Tests of Sterile-Neutrino Dark Matter: New Galactic Bulge Observations and Combined Impact*, *Phys. Rev. D* **101** (2020), no. 10 103011, [[1908.09037](#)].
- [73] R. Krivonos, D. Wik, B. Grefenstette, K. Madsen, K. Perez, et al., *NuSTAR measurement of the cosmic X-ray background in the 3–20 keV energy band*, *Mon. Not. Roy. Astron. Soc.* **502** (2021), no. 3 3966–3975, [[2011.11469](#)].
- [74] C. Dessert, N. L. Rodd, and B. R. Safdi, *The dark matter interpretation of the 3.5-keV line is inconsistent with blank-sky observations*, *Science* **367** (2020), no. 6485 1465–1467, [[1812.06976](#)].
- [75] J. W. Foster, M. Kongsore, C. Dessert, Y. Park, N. L. Rodd, et al., *Deep Search for Decaying Dark Matter with XMM-Newton Blank-Sky Observations*, *Phys. Rev. Lett.* **127** (2021), no. 5 051101, [[2102.02207](#)].
- [76] T. Yoshino, K. Mitsuda, N. Y. Yamasaki, Y. Takei, T. Hagihara, et al., *Energy Spectra of the Soft X-Ray Diffuse Emission in Fourteen Fields Observed with Suzaku*, *Publications of the Astronomical Society of Japan* **61** (Aug., 2009) 805, [[0903.2981](#)].
- [77] P. De la Torre Luque, S. Balaji, and J. Koechler, *Importance of cosmic ray propagation on sub-GeV dark matter constraints*, [2311.04979](#).
- [78] D. Clowe, A. Gonzalez, and M. Markevitch, *Weak lensing mass reconstruction of the*

- interacting cluster 1E0657-558: Direct evidence for the existence of dark matter*, *Astrophys. J.* **604** (2004) 596–603, [[astro-ph/0312273](#)].
- [79] D. Clowe, M. Bradac, A. H. Gonzalez, M. Markevitch, S. W. Randall, et al., *A direct empirical proof of the existence of dark matter*, *Astrophys. J. Lett.* **648** (2006) L109–L113, [[astro-ph/0608407](#)].
- [80] M. Bradac, D. Clowe, A. H. Gonzalez, P. Marshall, W. Forman, et al., *Strong and weak lensing united. 3. Measuring the mass distribution of the merging galaxy cluster 1E0657-56*, *Astrophys. J.* **652** (2006) 937–947, [[astro-ph/0608408](#)].
- [81] D. Paraficz, J. P. Kneib, J. Richard, A. Morandi, M. Limousin, et al., *The Bullet cluster at its best: weighing stars, gas, and dark matter*, *Astron. Astrophys.* **594** (2016) A121, [[1209.0384](#)].
- [82] S. W. Randall, M. Markevitch, D. Clowe, A. H. Gonzalez, and M. Bradac, *Constraints on the Self-Interaction Cross-Section of Dark Matter from Numerical Simulations of the Merging Galaxy Cluster 1E 0657-56*, *Astrophys. J.* **679** (2008) 1173–1180, [[0704.0261](#)].
- [83] A. Robertson, R. Massey, and V. Eke, *What does the Bullet Cluster tell us about self-interacting dark matter?*, *Mon. Not. Roy. Astron. Soc.* **465** (2017), no. 1 569–587, [[1605.04307](#)].
- [84] D. Wittman, N. Golovich, and W. A. Dawson, *The Mismeasure of Mergers: Revised Limits on Self-interacting Dark Matter in Merging Galaxy Clusters*, *Astrophys. J.* **869** (2018), no. 2 104, [[1701.05877](#)].
- [85] J. G. Holland, H. Böhringer, G. Chon, and D. Pierini, *Optical and X-ray profiles in the REXCESS sample of galaxy clusters*, *Mon. Not. Roy. Astron. Soc.* **448** (2015), no. 3 2644–2664, [[1501.04286](#)].
- [86] P. Popesso, A. Biviano, H. Böhringer, and M. Romaniello, *RASS-SDSS Galaxy Cluster Survey. 7. On the Cluster Mass to Light ratio and the Halo Occupation Distribution*, *Astron. Astrophys.* **464** (2007) 451, [[astro-ph/0606260](#)].
- [87] R. N. Proctor, C. Mendes de Oliveira, L. Azanha, R. Dupke, and R. Overzier, *A derivation of masses and total luminosities of galaxy groups and clusters in the maxBCG catalogue*, *Mon. Not. Roy. Astron. Soc.* **449** (2015), no. 3 2345–2352, [[1503.00975](#)].
- [88] E. Tempel, T. Tuvikene, R. Kipper, and N. I. Libeskind, *Merging groups and clusters of galaxies from the SDSS data. The catalogue of groups and potentially merging systems*, *Astron. Astrophys.* **602** (2017) A100, [[1704.04477](#)].
- [89] F. Kahlhoefer, K. Schmidt-Hoberg, M. T. Frandsen, and S. Sarkar, *Colliding clusters and dark matter self-interactions*, *Mon. Not. Roy. Astron. Soc.* **437** (2014), no. 3 2865–2881, [[1308.3419](#)].
- [90] M. Markevitch, A. H. Gonzalez, D. Clowe, A. Vikhlinin, L. David, et al., *Direct constraints on the dark matter self-interaction cross-section from the merging galaxy cluster 1E0657-56*, *Astrophys. J.* **606** (2004) 819–824, [[astro-ph/0309303](#)].
- [91] **LSND Collaboration**, L. B. Auerbach et al., *Measurement of electron - neutrino - electron elastic scattering*, *Phys. Rev. D* **63** (2001) 112001, [[hep-ex/0101039](#)].
- [92] P. deNiverville, M. Pospelov, and A. Ritz, *Observing a light dark matter beam with neutrino experiments*, *Phys. Rev. D* **84** (2011) 075020, [[1107.4580](#)].
- [93] **MiniBooNE-DM Collaboration**, A. Aguilar-Arevalo et al., *Dark matter search in nucleon, pion, and electron channels from a proton beam dump with miniboone*, *Phys. Rev. D* **98** (Dec, 2018) 112004.
- [94] **NA64 Collaboration**, Y. M. Andreev et al., *Search for Light Dark Matter with NA64 at CERN*, *Phys. Rev. Lett.* **131** (2023), no. 16 161801, [[2307.02404](#)].

- [95] **BaBar Collaboration**, J. P. Lees et al., *Search for Invisible Decays of a Dark Photon Produced in e^+e^- Collisions at BaBar*, *Phys. Rev. Lett.* **119** (2017), no. 13 131804, [[1702.03327](#)].
- [96] P. deNiverville, C.-Y. Chen, M. Pospelov, and A. Ritz, *Light dark matter in neutrino beams: production modelling and scattering signatures at MiniBooNE, T2K and SHiP*, *Phys. Rev. D* **95** (2017), no. 3 035006, [[1609.01770](#)].
- [97] D. Curtin, R. Essig, S. Gori, and J. Shelton, *Illuminating Dark Photons with High-Energy Colliders*, *JHEP* **02** (2015) 157, [[1412.0018](#)].
- [98] B. M. Loizos, X. G. Wang, A. W. Thomas, M. J. White, and A. G. Williams, *Constraints on the dark sector from electroweak precision observables*, [2306.13408](#).
- [99] M. P. Bento, H. E. Haber, and J. a. P. Silva, *Classes of complete dark photon models constrained by Z-physics*, *Phys. Lett. B* **850** (2024) 138501, [[2311.04976](#)].
- [100] **NA62 Collaboration**, E. Cortina Gil et al., *Search for dark photon decays to $\mu^+\mu^-$ at NA62*, *JHEP* **09** (2023) 035, [[2303.08666](#)].
- [101] **BaBar Collaboration**, J. P. Lees et al., *Search for a Dark Photon in e^+e^- Collisions at BaBar*, *Phys. Rev. Lett.* **113** (2014), no. 20 201801, [[1406.2980](#)].
- [102] **NA48/2 Collaboration**, J. R. Batley et al., *Search for the dark photon in π^0 decays*, *Phys. Lett. B* **746** (2015) 178–185, [[1504.00607](#)].
- [103] M. Ibe, W. Nakano, Y. Shoji, and K. Suzuki, *Migdal Effect in Dark Matter Direct Detection Experiments*, *JHEP* **03** (2018) 194, [[1707.07258](#)].
- [104] R. Essig, J. Mardon, and T. Volansky, *Direct Detection of Sub-GeV Dark Matter*, *Phys. Rev. D* **85** (2012) 076007, [[1108.5383](#)].
- [105] **XENON Collaboration**, E. Aprile et al., *Light Dark Matter Search with Ionization Signals in XENON1T*, *Phys. Rev. Lett.* **123** (2019), no. 25 251801, [[1907.11485](#)].
- [106] **SENSEI Collaboration**, L. Barak et al., *SENSEI: Direct-Detection Results on sub-GeV Dark Matter from a New Skipper-CCD*, *Phys. Rev. Lett.* **125** (2020), no. 17 171802, [[2004.11378](#)].
- [107] **DarkSide Collaboration**, P. Agnes et al., *Search for Dark Matter Particle Interactions with Electron Final States with DarkSide-50*, *Phys. Rev. Lett.* **130** (2023), no. 10 101002, [[2207.11968](#)].
- [108] **PandaX Collaboration**, D. Huang et al., *Search for Dark-Matter–Nucleon Interactions with a Dark Mediator in PandaX-4T*, *Phys. Rev. Lett.* **131** (2023), no. 19 191002, [[2308.01540](#)].
- [109] **DAMIC-M Collaboration**, I. Arnquist et al., *First Constraints from DAMIC-M on Sub-GeV Dark-Matter Particles Interacting with Electrons*, *Phys. Rev. Lett.* **130** (2023), no. 17 171003, [[2302.02372](#)].
- [110] **SuperCDMS Collaboration**, D. W. Amaral et al., *Constraints on low-mass, relic dark matter candidates from a surface-operated SuperCDMS single-charge sensitive detector*, *Phys. Rev. D* **102** (2020), no. 9 091101, [[2005.14067](#)].
- [111] **LZ Collaboration**, J. Aalbers et al., *Search for new physics in low-energy electron recoils from the first LZ exposure*, *Phys. Rev. D* **108** (2023), no. 7 072006, [[2307.15753](#)].
- [112] T. Emken, *obscura: A modular c++ tool and library for the direct detection of (sub-gev) dark matter via nuclear and electron recoils*, *Journal of Open Source Software* **6** (2021), no. 68 3725.
- [113] R. Catena, T. Emken, N. A. Spaldin, and W. Tarantino, *Atomic responses to general dark matter-electron interactions*, *Phys. Rev. Res.* **2** (2020), no. 3 033195, [[1912.08204](#)].

- [114] R. Essig, M. Fernandez-Serra, J. Mardon, A. Soto, T. Volansky, et al., *Direct Detection of sub-GeV Dark Matter with Semiconductor Targets*, *JHEP* **05** (2016) 046, [[1509.01598](#)].
- [115] **CRESST Collaboration**, A. H. Abdelhameed et al., *First results from the CRESST-III low-mass dark matter program*, *Phys. Rev. D* **100** (2019), no. 10 102002, [[1904.00498](#)].
- [116] M. J. Dolan, F. Kahlhoefer, and C. McCabe, *Directly detecting sub-GeV dark matter with electrons from nuclear scattering*, *Phys. Rev. Lett.* **121** (2018), no. 10 101801, [[1711.09906](#)].
- [117] D. Baxter, Y. Kahn, and G. Krnjaic, *Electron Ionization via Dark Matter-Electron Scattering and the Migdal Effect*, *Phys. Rev. D* **101** (2020), no. 7 076014, [[1908.00012](#)].
- [118] R. Essig, J. Pradler, M. Sholapurkar, and T.-T. Yu, *Relation between the Migdal Effect and Dark Matter-Electron Scattering in Isolated Atoms and Semiconductors*, *Phys. Rev. Lett.* **124** (2020), no. 2 021801, [[1908.10881](#)].
- [119] T. Emken and C. Kouvaris, *DaMaSCUS: The Impact of Underground Scatterings on Direct Detection of Light Dark Matter*, *JCAP* **10** (2017) 031, [[1706.02249](#)].
- [120] T. Emken and C. Kouvaris, *How blind are underground and surface detectors to strongly interacting Dark Matter?*, *Phys. Rev. D* **97** (2018), no. 11 115047, [[1802.04764](#)].
- [121] T. Bringmann and M. Pospelov, *Novel direct detection constraints on light dark matter*, *Phys. Rev. Lett.* **122** (2019), no. 17 171801, [[1810.10543](#)].
- [122] **GAMBIT Collaboration**, G. D. Martinez, J. McKay, B. Farmer, P. Scott, E. Roebber, et al., *Comparison of statistical sampling methods with ScannerBit, the GAMBIT scanning module*, *Eur. Phys. J. C* **77** (2017), no. 11 761, [[1705.07959](#)].
- [123] W. J. Handley, M. P. Hobson, and A. N. Lasenby, *PolyChord: nested sampling for cosmology*, *Mon. Not. Roy. Astron. Soc.* **450** (2015), no. 1 L61–L65, [[1502.01856](#)].
- [124] S. Balan et al., *Supplementary data: Resonant or asymmetric: The status of sub-GeV dark matter*, .
- [125] W. Handley, *anesthetic: nested sampling visualisation*, *J. Open Source Softw.* **4** (2019), no. 37 1414, [[1905.04768](#)].
- [126] L. T. Hergt, W. J. Handley, M. P. Hobson, and A. N. Lasenby, *Bayesian evidence for the tensor-to-scalar ratio r and neutrino masses m_ν : Effects of uniform vs logarithmic priors*, *Phys. Rev. D* **103** (2021) 123511, [[2102.11511](#)].
- [127] **LHCb Collaboration**, R. Aaij et al., *Search for $A' \rightarrow \mu^+ \mu^-$ Decays*, *Phys. Rev. Lett.* **124** (2020), no. 4 041801, [[1910.06926](#)].
- [128] **Belle-II Collaboration**, W. Altmannshofer et al., *The Belle II Physics Book*, *PTEP* **2019** (2019), no. 12 123C01, [[1808.10567](#)]. [Erratum: PTEP 2020, 029201 (2020)].
- [129] T. Åkesson et al., *Current Status and Future Prospects for the Light Dark Matter eXperiment*, in *Snowmass 2021*, 3, 2022. [2203.08192](#).
- [130] **SuperCDMS Collaboration**, R. Agnese et al., *Projected Sensitivity of the SuperCDMS SNOLAB experiment*, *Phys. Rev. D* **95** (2017), no. 8 082002, [[1610.00006](#)].
- [131] B. von Krosigk et al., *DELight: A Direct search Experiment for Light dark matter with superfluid helium*, *SciPost Phys. Proc.* **12** (2023) 016, [[2209.10950](#)].
- [132] P. Scott, *Pippi - painless parsing, post-processing and plotting of posterior and likelihood samples*, *Eur. Phys. J. Plus* **127** (2012) 138, [[1206.2245](#)].
- [133] T. Bringmann, *Particle Models and the Small-Scale Structure of Dark Matter*, *New J. Phys.* **11** (2009) 105027, [[0903.0189](#)].
- [134] A. Hryczuk and M. Laletin, *Impact of dark matter self-scattering on its relic abundance*, *Phys. Rev. D* **106** (2022), no. 2 023007, [[2204.07078](#)].

- [135] A. Alloul, N. D. Christensen, C. Degrande, C. Duhr, and B. Fuks, *FeynRules 2.0 - A complete toolbox for tree-level phenomenology*, *Comput. Phys. Commun.* **185** (2014) 2250–2300, [[1310.1921](#)].
- [136] A. Belyaev, N. D. Christensen, and A. Pukhov, *CalcHEP 3.4 for collider physics within and beyond the Standard Model*, *Comput. Phys. Commun.* **184** (2013) 1729–1769, [[1207.6082](#)].
- [137] B. Batell, R. Essig, and Z. Surujon, *Strong Constraints on Sub-GeV Dark Sectors from SLAC Beam Dump E137*, *Phys. Rev. Lett.* **113** (2014), no. 17 171802, [[1406.2698](#)].
- [138] B. Batell, P. deNiverville, D. McKeen, M. Pospelov, and A. Ritz, *Leptophobic Dark Matter at Neutrino Factories*, *Phys. Rev. D* **90** (2014), no. 11 115014, [[1405.7049](#)].
- [139] **GAMBIT Models Workgroup Collaboration**, P. Athron et al., *SpecBit, DecayBit and PrecisionBit: GAMBIT modules for computing mass spectra, particle decay rates and precision observables*, *Eur. Phys. J. C* **78** (2018), no. 1 22, [[1705.07936](#)].
- [140] **GAMBIT Collaboration**, C. Balázs et al., *ColliderBit: a GAMBIT module for the calculation of high-energy collider observables and likelihoods*, *Eur. Phys. J. C* **77** (2017), no. 11 795, [[1705.07919](#)].

Table 2. Capabilities added to DarkBit associated with this work. LL is shorthand for `LogLikelihood`.

Capability	Function (type)	Dependencies [type] / Backend reqs [type (args)]
TH_ProcessCatalog	TH_ProcessCatalog_SubGeVDM_fermion (TH_ProcessCatalog) TH_ProcessCatalog_SubGeVDM_scalar (TH_ProcessCatalog)	SubGeVDM_spectrum [Spectrum] decay_rates [DecayTable]
DD_couplings	DD_couplings_SubGeVDM_fermion (DM_nucleon_couplings) DD_couplings_SubGeVDM_scalar (DM_nucleon_couplings)	
DarkMatter_ID	DarkMatter_ID_SubGeVDM_fermion (string) DarkMatter_ID_SubGeVDM_scalar (string)	
DarkMatterConj_ID	DarkMatterConj_ID_SubGeVDM_fermion (string) DarkMatterConj_ID_SubGeVDM_scalar (string)	
RD_oh2_aDM	RD_oh2_DS_general_aDM (ddpair)	RD_spectrum_ordered [RD_spectrum_type] RD_eff_annrate [fptr_dd] RD_oh2_DS6_ini [int] dsrdstart [void (...)] dsrdens [void (...)] rdpars [DS_RDPARS] adm_com [DS_ADM_COM]
ID_suppression,	ID_suppression_aDM (double) ID_suppression_symDM (double)	RD_oh2_aDM [ddpair] RD_fraction [double] DM_process [std::string]
DM_mass_loss	TH_ProcessCatalog_SubGeVDM_scalar (TH_ProcessCatalog)	SubGeVDM_spectrum [Spectrum] decay_rates [DecayTable]
BulletCluster_inL	calc_bullet_cluster_DMmassLoss (double)	SubGeVDM_spectrum [Spectrum] RD_fraction [double] RD_oh2_aDM [ddpair] decay_rates [DecayTable]
Xray_loglikelihoods	TH_ProcessCatalog_SubGeVDM_scalar (TH_ProcessCatalog)	SubGeVDM_spectrum [Spectrum] decay_rates [DecayTable]
set_gamLike_GC_halo	Xray_loglikes_Cirelli (double)	WIMP_properties [WIMPprops] LocalHalo [LocalMaxwellianHalo] TH_ProcessCatalog [TH_ProcessCatalog] ID_suppression [double]
LocalHalo_GeV	ExtractLocalMaxwellianHalo_GeV (LocalMaxwellianHalo)	
XENON1T_ER_LL	calc_XENON1T_ER_LL (double)	LocalHalo_GeV [LocalMaxwellianHalo] RD_fraction [double] sigma_e [double] XENON1T_S2_ER [obscura:: DM_Detector_Ionization_ER]
DarkSide50_ER_LL	calc_DarkSide50_ER_LL (double)	LocalHalo_GeV [LocalMaxwellianHalo] RD_fraction [double] sigma_e [double] DarkSide50_S2_ER [obscura:: DM_Detector_Ionization_ER]
DarkSide50_ER_2023_LL	calc_DarkSide50_ER_2023_LL (double)	LocalHalo_GeV [LocalMaxwellianHalo] RD_fraction [double] sigma_e [double] DarkSide50_S2_ER_2023 [obscura:: DM_Detector_Ionization_ER]

Table 3. Capabilities added to DarkBit associated with this work (continued). LL is shorthand for LogLikelihood.

Capability	Function (type)	Dependencies [type] / Backend reqs [type (args)]
PandaX_4T_ER_LL	calc_PandaX_4T_ER_LL (double)	LocalHalo_GeV [LocalMaxwellianHalo] RD_fraction [double] sigma_e [double] PandaX_S2_4T_ER [obscura:: DM_Detector_Ionization_ER]
SENSEI_at_MINOS_LL	calc_SENSEI_at_MINOS_LL (double)	LocalHalo_GeV [LocalMaxwellianHalo] RD_fraction [double] sigma_e [double] SENSEI_at_MINOS [obscura:: DM_Detector_Crystal]
CDMS_HVeV_2020_LL	calc_CDMS_HVeV_2020_LL (double)	LocalHalo_GeV [LocalMaxwellianHalo] RD_fraction [double] sigma_e [double] CDMS_HVeV_2020 [obscura:: DM_Detector_Crystal]
DAMIC_M_2023_LL	calc_DAMIC_M_2023_LL (double)	LocalHalo_GeV [LocalMaxwellianHalo] RD_fraction [double] sigma_e [double] DAMIC_M_2023 [obscura:: DM_Detector_Crystal]
XENON1T_Migdal_LL	calc_XENON1T_Migdal_LL (double)	LocalHalo_GeV [LocalMaxwellianHalo] RD_fraction [double] sigma_SI_p [double] sigma_SI_n [double] XENON1T_Migdal [obscura:: DM_Detector_Ionization_Migdal]
DarkSide50_Migdal_LL	calc_DarkSide50_Migdal_LL (double)	LocalHalo_GeV [LocalMaxwellianHalo] RD_fraction [double] sigma_SI_p [double] sigma_SI_n [double] DarkSide50_Migdal [obscura:: DM_Detector_Ionization_Migdal]
DarkSide50_Migdal_2023_LL	calc_DarkSide50_Migdal_2023_LL (double)	LocalHalo_GeV [LocalMaxwellianHalo] RD_fraction [double] sigma_SI_p [double] sigma_SI_n [double] DarkSide50_Migdal_2023 [obscura:: DM_Detector_Ionization_Migdal]
PandaX_4T_Migdal_LL	calc_PandaX_4T_Migdal_LL (double)	LocalHalo_GeV [LocalMaxwellianHalo] RD_fraction [double] sigma_SI_p [double] sigma_SI_n [double] PandaX_4T_Migdal [obscura:: DM_Detector_Ionization_Migdal]
RD_oh2_underprediction	RD_oh2_underprediction_SubGeVDM (double)	

Table 4. Capabilities added to CosmoBit associated with this work.

Capability	Function (type)	Dependencies [type] / Backend reqs [type (args)]
<code>Neff_after_BBN</code>	<code>extract_Neff_after_BBN</code> (double)	<code>primordial_abundances</code> [<code>BBN_container</code>]
<code>N_eff_likelihood_Planck_BAO</code>	<code>compute_N_eff_likelihood_Planck_BAO</code> (double)	<code>Neff_after_BBN</code> [double]

Table 5. Capabilities added to ColliderBit associated with this work.

Capability	Function (type)	Dependencies [type] / Backend reqs [type (args)]
<code>BaBar_single_photon_LogLike</code>	<code>BaBar_single_photon_LogLike_SubGeVDM</code> (double)	<code>dark_photon_decay_rates</code> [<code>DecayTable::Entry</code>]
<code>AllAnalysisNumbers</code>	<code>SubGeVDM_results</code> (<code>AnalysisDataPointers</code>)	<code>SubGeVDM_spectrum</code> [<code>Spectrum</code>]